Doctoral dissertation

Study on Digital Coherent Optical Pulse Transmission with a High Spectral Efficiency
(高い周波数利用効率を有するデジタルコヒーレント光パルス伝送に関する研究)

東北大学大学院工学研究科
通信工学専攻

David Odeke OTUYA
B3TD2302

Contents

Chapter 1

Introduction

1.1 Data traffic increase and the state of optical communication research

Driven by the rapid growth of the Internet through broadband fixed and mobile access and with new services such as high definition video streaming and "big data" [1]- [2], data traffic in backbone networks is ever increasing across the world. Figure 1.1 shows the recent trend in the total data downloads, as an indicator for data traffic in backbone networks, in Japan. There has been an exponential increase in the data traffic over the last decade, with current annual increase as large as 40%. If this increase continues at this rate over the next 15 years, the total data traffic would reach 1 Petabit/s by the year 2030.

The above expansion in demand necessitates an immediate and aggressive steps towards increasing capacity, since the scalability of data transmission capacity with current wavelength division multiplexing (WDM) technologies is limited by the bandwidth of erbium-doped fiber amplifier (EDFA), which is approximately 85 nm (1525-1610 nm) [3]. Fiber fusing is another limiting factor for capacity increase, since it limits the signal power through optical fibers to approximately 1 W per single fiber strand [4]. These two factors put the maximum data capacity through a single strand of fiber at 100 Tbit/s, a value 10 times smaller than the required 1 Petabit/s after 15 years from now.

To bridge this impending gap in capacity, there have been intensive efforts being made to come up with high capacity signal generation, transmission and detection techniques [5]- [6]. Now, with the successful development and commercialization of digital coherent technologies for 100 Gbit/s system in optical communication transmission, research is intensively shifting its focus

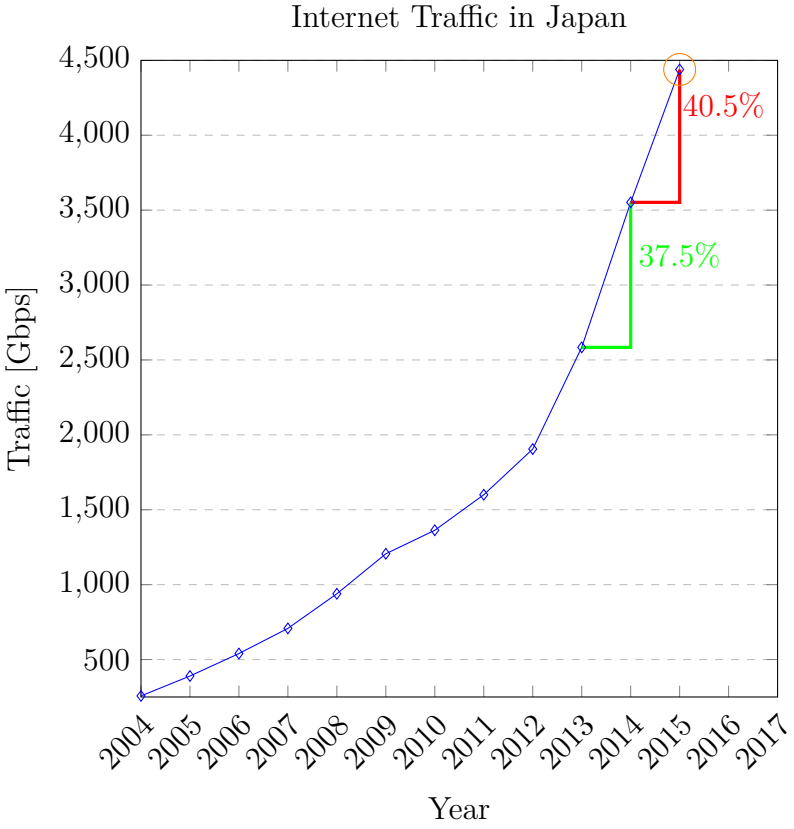

Figure 1.1: Total data traffic in Japan

towards expanding capacity to 1 Tbit/s and beyond [7]. There are mainly two approaches currently under research that can scale up the transmission capacity per single WDM channel. The first approach involves the use of time division multiplexing (TDM), either electrically through electrical time division multiplexing (ETDM) or in the optical domain employing optical time division multiplexing (OTDM). Using ETDM, however, the speed limitation of electronic devices such as DACs makes it difficult to achieve transmission speeds of beyond 1 Tbit/s. On the other hand, with OTDM, by using ultrashort optical pulses, it is possible to increase the bit rate to 1 Tbit/s and beyond. Several epoch making experimental results on OTDM have been reported. Nakazawa et. al. reported a 1.28 Tbit/s transmission experiment over 70 km in the year 2000, which was the first single channel Tbit/s transmission experiment [8]. In 2005, Weber et. al. reported both 1.28 Tbit/s and 2.56 Tbit/s transmission experiments utilizing differential quadrature phase shift keying (DQPSK) [9]- [10]. In 2010, a demonstration of a 5.1 Tbit/s modulation and demodulation experiment using differential

quadrature phase shift keying (DQPSK) was reported [11]. In the same year, a 2.56 Tbit/s, DQPSK transmission over 300 km was also reported [12]. Despite the fact that transmission speeds obtained using OTDM can be scaled to over 1 Tbit/s, ultrashort pulses used in OTDM require very broad signal bandwidth that limits the maximum achievable spectral efficiency to below 1 bit/s/Hz.

The other approach under intensive research is the use of multilevel modulation formats such as quadrature amplitude modulation (QAM). Unlike conventional modulation formats such as on-off keying (OOK) which transmits 1 bit per symbol, 16-QAM, for example, transmits 4 bits per symbol as shown in Fig. 1.2. In general, 2^N-QAM enables N bits to be transmitted for each symbol. This means that the spectral efficiency can be increased by N-fold compared to OOK when a 2^N-QAM modulation format is adopted. This comes at an expense of having to use advanced electronic devices such as high quantization-resolution DACs at the transmitter and ADCs at the receiver, in combination with digital signal processing (DSP) for demodulation. Several higher order QAM transmission experimental results have been reported. A 54-Gbit/s, 512-QAM coherent optical transmission over 150 km has been reported [13]. A transmission experiment with 1024 QAM over the same distance of 150 km has been demonstrated [14]. Furthermore, more recently, a record 2048 QAM transmission experiment achieving a spectral efficiency of 15.3 bit/s/Hz has been demonstrated [15]. However, it is difficult to achieve a transmission speed of 1 Tbit/s or beyond with this technique due to the bandwidth limitation of electronics such as DACs and ADCs.

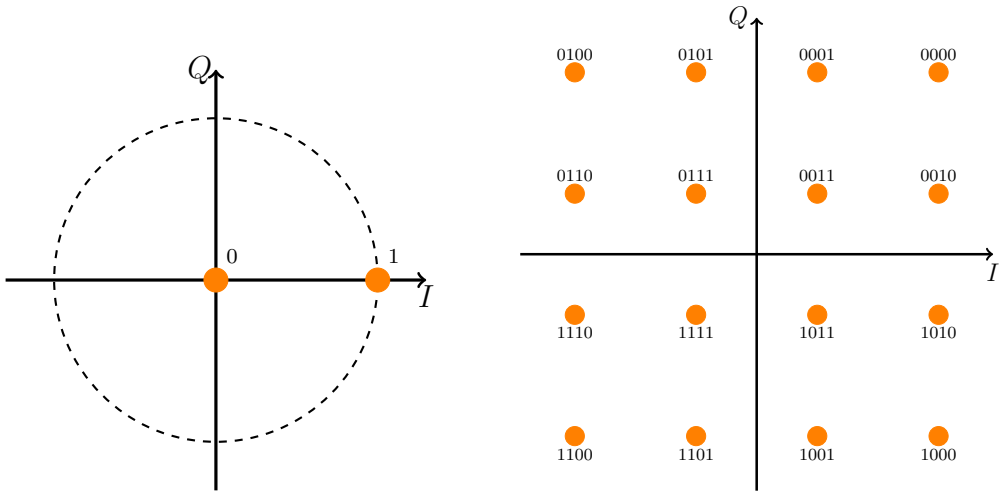

(a) OOK (b) 16 QAM

Figure 1.2: Constellations and the corresponding Gray coding

1.2 Trends in high speed and high spectrally efficient optical transmission

In order to overcome the spectral efficiency limitation in conventional TDM transmission, TDM of coherent optical pulses has been recently proposed, where the pulses are modulated with QAM data and bit interleaved to higher symbol rate with OTDM. Fig. 1.3 summarises recent experimental results on high speed coherent TDM transmission. First, an ETDM-based 110 Gbaud, polarization-division multiplexed (PDM)-QPSK transmission (440 Gbit/s $\times$ 20 ch) giving rise to a spectral efficiency of 4 bit/s/Hz has been demonstrated [16]. In addition, a single-carrier transmission of 107 Gbaud PDM-16 QAM signal at a bit rate of 856 Gbit/s was also demonstrated at a spectral efficiency of 5.9 bit/s/Hz [17]. Furthermore, with a high speed DAC, a demonstration of a 72 Gbaud PDM-64 QAM signal transmission at a bit rate of 864 Gbit/s leading to a spectral efficiency of 6.4 bit/s/Hz has also been reported [18]. On the other hand, by using OTDM, a QPSK transmission at bit rate of 640 Gbit/s has been demostrated [19]. Precise phase locking of the receiver local oscillator to the data signal achieved by use of an optical phase-locked loop (OPLL) technique made it possible to increase the QAM multiplicity further to 32 QAM, where both 400 and 800 Gbit/s, 32 QAM transmission experiments over 225 km have been reported [20]- [22]. Furthermore, a single-carrier 5.1 Tbit/s, 16-QAM coherent transmission at 10 Gbaud $\times$ 64 OTDM over 80 km of fiber has been demonstrated at a

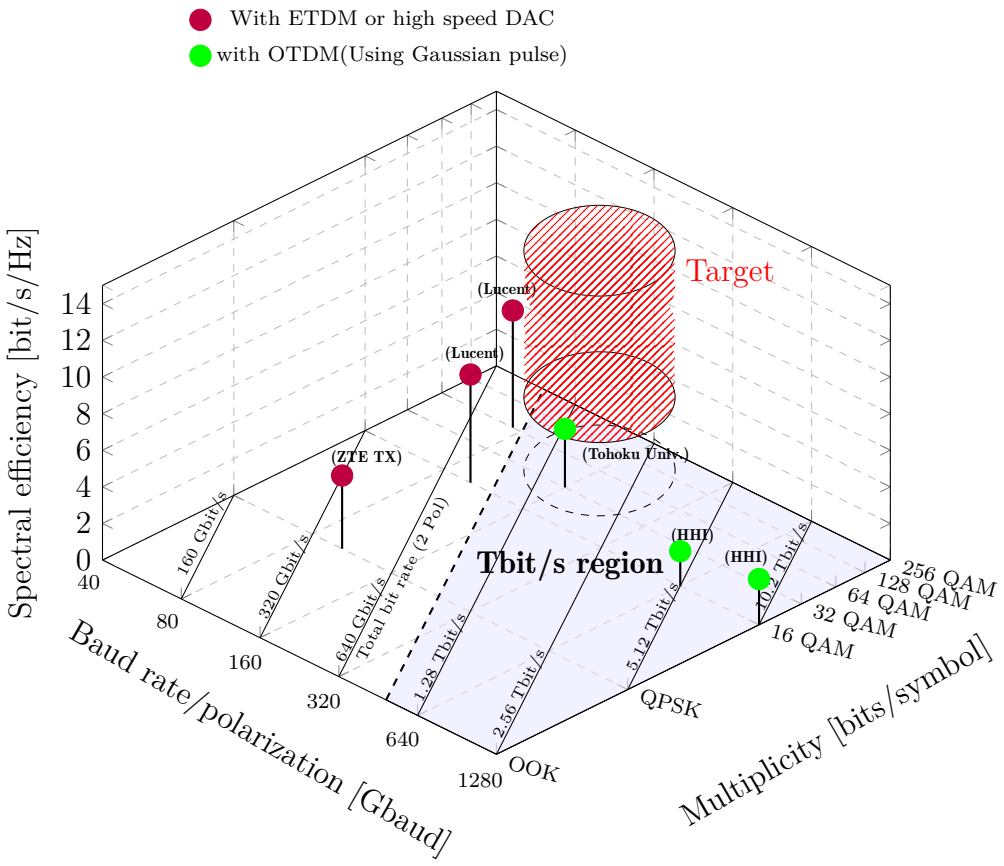

Figure 1.3: Recent trend in high speed coherent communication

spectral efficiency of 1.9 bit/s/Hz [23]. In addition, with an OTDM multiplicity of 128, a spectral efficiency of 2.5 bit/s/Hz was achieved with a 1.28 Tbaud, 16-QAM signal transmission at a 10.2 Tbit/s bit rate through 29 km of fiber using "self" homodyne method [24]. With ETDM for coherent transmission, the bandwidth of DACs and ADCs limits the symbol rates, making it difficult to achieve transmission bit rates of beyond 1 Tbit/s, even when using higher order modulation formats. On the other hand, as a result of using very short pulses for coherent OTDM, the spectral efficiency in coherent OTDM transmissions is still limited to below 2.5 bit/s/Hz. Therefore, developing a system that is of both high speed and high spectral efficiency is of utmost importance in realizing ultimate transmission capacity with the available bandwidth resources.

1.3 Objective and outline of this dissertation

As mentioned in section 1.2, developing a system that is both high speed and high spectrally efficient is vital in making the best use of the available bandwidth resources. Due to the fundamental limitation in the bandwidth of DACs and ADCs, it has been difficult to achieve a single channel bit rate of 1 Tbit/s and beyond even with ETDM. To overcome this bottleneck, coherent optical pulse and its OTDM are expected to realize a bit rate faster than 1 Tbit/s. At the same time, however, it should be noted that the inherent broad spectral width of short optical RZ pulses, such as Gaussian and sech pulses that are typically employed in OTDM, can reduce the spectral efficiency.

This work aims at achieving high speed transmission faster than 1 Tbit/s in a single channel while retaining high spectral efficiency in digital coherent optical QAM transmission. This work first demonstrates coherent pulse transmission of 64 QAM signals using a Gaussian pulse. To further increase the spectral efficiency, this work proposes a coherent Nyquist pulse transmission that enables us to realize high-speed transmission with a broad pulse width, i.e, in a narrow bandwidth, without being affected by intersymbol interference (ISI). In particular, by taking advantage of time-domain orthogonality in coherent Nyquist pulses, it is demonstrated that the spectral efficiency can be considerably increased.

This work is divided into six chapters. Chapter 2 covers the fundamental configuration of a digital coherent transmission system, describing key components such as a coherent pulse source, optical phase-locked loop (OPLL) for highly precise phase synchronization, OTDM demultiplexer, and digital signal processor. Particular focus is made on optimization of these components for coherent pulse transmission. This chapter also describes a waveform distortion compensation based on digital signal processing referred to as frequency domain equalization (FDE), which plays a crucial role in realizing high speed and high spectrally efficient coherent transmission.

In Chapter 3, I describe a digital coherent 64 QAM transmission at 1.92 Tbit/s/ch using a Gaussian pulse. Since a mode-locked pulse laser that can directly emit coherent pulses had not been realized, a 2.4 ps coherent Gaussian pulse generation is demonstrated for the first time by using a frequency-stabilized CW laser and an ultra-broadband optical comb generator. In addition, since coherent pulse transmission is largely affected by S/N degradation due to broad bandwidth compared to conventional digital coherent QAM with a CW carrier, a novel scheme of RZ-CW conversion is introduced at the receiver so that the received signal can be confined within a narrow receiver bandwidth without loss of energy. Furthermore, a precise frequency domain equalization (FDE) technique is newly developed for com-

pensation of waveform distortion that result from hardware imperfections. As a result, 1.92 Tbit/s, 64 QAM transmission is demonstrated over 150 km resulting in a spectral efficiency of 3.8 bit/s/Hz [2].

In chapter 4, I propose a high spectral-efficiency coherent pulse, known as a Nyquist pulse, that greatly reduces the signal bandwidth requirement, consequently increasing the spectral efficiency of the coherent pulse transmission [26]. Nyquist pulse has a sinc (or quasi sinc)-function waveform and a rectangular (or raised-cosine) spectral profile. In this work, a coherent Nyquist pulse is generated for the first time by combining a coherent pulse source developed in chapter 3 and a pulse shaper, in which the frequency comb is converted to the spectral profile of a Nyquist pulse with a proper control of amplitude and phase of each longitudinal mode. As a demultiplexer, an ultrafast optical sampling circuit comprising NOLM (Nonlinear Optical Loop Mirror) is newly employed so that only a portion of the signal at each symbol interval can be extracted without affected by ISI. By using coherent Nyquist pulses, it is demonstrated that the spectral efficiency of the 1.92 Tbit/s, 64 QAM transmission is increased to 7.5 bit/s/Hz, which is almost twice of that with a Gaussian pulse [27].

In Chapter 5, I propose a novel scheme for coherent Nyquist pulse transmission utilizing the time-domain orthogonality. Specifically, a new OTDM demultiplexing scheme exploiting the orthogonal property of the OTDM Nyquist pulse is demonstrated. This can be realized by using a Nyquist pulse both as a transmission signal and a local oscillator whose phase and timing are synchronized. This enables the coherent Nyquist pulse to be demultiplexed and homodyne-detected simultaneously in a coherent receiver, resulting in a high performance demultiplexing and much simpler receiver configuration compared to the ultrafast sampling scheme. With this scheme, I was able to increase the spectral efficiency further up to 10.6 bit/s/Hz, due to the ability to utilize a Nyquist pulse of the minimum spectral width [28]. Also in Chapter 5, I describe the increase in transmission speed from 1.92 Tbit/s to 3.84 Tbit/s by doubling the symbol rate. This is realized by newly employing a HCN frequency-stabilized mode-locked fiber laser (MLFL), that can directly emit a high OSNR coherent optical pulse.

In Chapter 6 , I summarize this work, and I also describe how this work compares with the theoretical Shannon limit. I also elaborate future challenges toward further increase in both the transmission speed and the spectral efficiency.

Chapter 1 References

[1] Editorial, "Community cleverness required," *Nature*, 455(1), (2008).

[2] C. Snijders, U. Matzat, and U-D. Reips, ""Big Data": Big gaps of Knowledge in the Field of Internet Science," *International Journal of Internet Science*, 7(1), 1-5, (2012).

[3] M. Yamada, A. Mori, K. Kobayashi, H. Ono, T. Kanamori, K. Oikawa, Y. Nishida, and Y. Ohishi, "Gain-flattened Tellurite-based EDFA with a Flat amplification bandwidth of 76 nm," *IEEE Photon. Techn. Lett.*, 10(9), 1244-1246, (1998).

[4] R. Kashyap and K. J. Blow, "Observation of catastrophic self-propelled self-focussing in optical fibers," *Electron. Lett.*, 24(1), 47-49, (1988).

[5] E. Desurvire, "Capacity demand and technology challenges for lightwave systems in the next two decades," *J. Lightwave Technol.*, 24(12), 4697-4710, (2006).

[6] M. Nakazawa, "Giant leaps in optical communication technologies towards 2030 and beyond," *plenary talk in European Conference on optical Communication (ECOC2010),* Torino, 2010.

[7] P. Winzer, "Beyond 100G ethernet," IEEE Commun. Mag.48(7), 26-30(2010).

[8] M. Nakazawa, T. Yamamoto, and K. R. Tamura, "1.28 Tbit/s-70 km OTDM transmission using third- and fourth-order simultaneous dispersion compensation with a phase modulator," *Electron. Lett.,* 36(24), 2027-2029 (2000).

[9] H. G. Weber, S. Ferber, M. Kroh, C. Schmidt-Langhorst, R. Ludwig, V. Merembert, C. Boerner, F. Futami, S. Watanabe, and C. Schubert, "Single channel 1.28 Tbit/s and 2.56 Tbit/s DQPSK transmission," *in Proceedings of European Conference on Optical Communication (ECOC2005),* Th4.1.2 (2005).

[10] H. G. Weber, R. Ludwig, S. Ferber, C. Schmidt-Langhorst, M. Kroh, V. Merembert, C. Boerner, and C. Schubert, "Ultra-high OTDM-transmission technology," *J. Lightwave Technol.*, 24, 4616-4627 (2006).

[11] H. C. Mulvad, M. Galili, L. K. Oxenløwe, H. Hu, Anders T. Clausen, J. B. Jensen, C. Peucheret, and P. Jeppesen, "Demonstration of 5.1 Tbit/s data capacity on a single-wavelength channel" *Opt. Exp.*,18(2), 1438-1443 (2010).

[12] P. Guan, T. Hirano, K. Harako, Y. Tomiyama, T. Hirooka, and M. Nakazawa, "2.56 Tbit/s/ch Polarization-multiplexed DQPSK transmission over 300 km using time-domain optical Fourier transformation," *Opt. Exp.,* 19(26), B567-573 (2011).

[13] S. Okamoto, K. Toyoda, T. Omiya, K. Kasai, M. Yoshida, and M. Nakazawa, "512 QAM (54 Gbit/s) Coherent Optical Transmission over 150 km with an Optical Bandwidth of 4.1 GHz," *In Proceedings of European Conference on Communication (ECOC2010)*, PD2.3, (2010).

[14] Y. Koizumi, K. Toyoda, M. Yoshida, and M. Nakazawa, "1024 QAM (60 Gbit/s) single-carrier coherent optical transmission over 150 km," *Opt. Exp.,* 20(11), 12508-12514, (2012).

[15] S. Beppu, K. Kasai, M. Yoshida, and M. Nakazawa, "2048 QAM (66 Gbit/s) single-carrier coherent optical transmission over 150 km with a potential SE of 15.3 bit/s/Hz," *Opt. Exp.,* 23(4), 4960-4969, (2015).

[16] J. Zhang, Z. Dong, H. C. Chien, Z. Jia, Y. Xia, and Y. Chen, "Transmission of 20-Gb/s Super-Nyquist-Filtered Signals over 3600 km based on Single-Carrier 110-Gbaud PDM QPSK with 100-GHz Grid," *in Proceedings of the Optical Fiber Communication Conference (OFC2014)*, San Francisco, Th5B.5 (2014).

[17] G. Raybon, S. Randel, A. Adamiecki, and P. J. Winzer, "High symbol rate transmission systems for data rates above 400 Gb/s using TDM transmitters and receivers," *in Proceedings of the European Conference on Optical Communication (ECOC2014)*, Cannes, Tu.3.3.5 (2014).

[18] S. Randel, D. Pilori, S. Corteselli, G. Raybon, A. Adamiecki, A Gnauck, S. Chandrasekhar, P. J. Winzer, L. Altenhain, A. Bielik, and R. Schmid, "All-electronic flexibly programmable 864-Gb/s single-carrier PDM-64 QAM," *in Proceedings of the Optical Fiber Conference (OFC2014)*, Th5C.8 (2014).

[19] C. Zhang, Y. Mori, M. Usui, K. Igarashi, K. Katoh, and K. Kikuchi,"Straight-line 1073-km transmission of 640-Gbit/s dual-polarization QPSK signals on a single carrier," *in Proceedings of European Conference on Optical Communication (ECOC2009)*, Vienna, Austria, PD2.8 (2009).

[20] K. Kasai, T. Omiya, P. Guan, M. Yoshida, T. Hirooka, and M. Nakazawa, "Single-channel 400 Gbit/s, OTDM-32 RZ/QAM coherent transmission over 225 km using an optical phase-locked loop technique," *IEEE Photon. Technol. Lett.,* 22(8), 562-564, (2010).

[21] M. Nakazawa, K. Kasai, M. Yoshida, and T. Hirooka, "Novel RZ-CW conversion scheme for ultra multi-level high-speed coherent OTDM transmission," *Opt. Exp.,* 19(26), B574-492 (2011).

[22] K. Kasai, T. Omiya, P. Guan, M. Yoshida, T. Hirooka, and M. Nakazawa,"Single-carrier 800-Gb/s 32 RZ/QAM coherent transmission over 225 km employing a novel RZ-CW conversion technique," *IEEE Photon. Technol. Lett.,* 24(5), 416-418 (2012).

[23] E. Palushani, C. Schmidt-Langhorst, T. Richter, M. Nolle, R. Ludwig, and C. Schubert, "Transmission of a serial 5.1-Tb/s data signalusing 16-QAM and coherent detection," *in Proceedings of the European Conference on Optical Communication (ECOC2011)*, Geneva, We.8.B.5 (2011).

[24] T. Richter, C. Schmidt-Langhorst, M. Nolle, R. Ludwig, and C. Schubert, "Single wavelength channel 10.2 Tb/s TDM-capacity using 16-QAM and coherent detection," *in Proceedings of the Optical Fiber Communication Conference (OFC2011)*, Los Angeles, 2011, PDPA9.

[25] D. O. Otuya, K. Kasai, M. Yoshida, T. Hirooka, and M. Nakazawa, "A single-channel, 64 QAM coherent optical pulse transmission over 150 km using frequency-domain equalization (FDE)," *Opt. Exp.,* 21(19), 22808-22816 (2013).

[26] M. Nakazawa, T. Hirooka, P. Ruan, and P. Guan, "Ultrahigh-speed "orthogonal" TDM transmission with an optical Nyquist pulse train," *Opt. Exp.,* 20(2), 1129-1140 (2012).

[27] D. O. Otuya, K. Kasai, M. Yoshida, T. Hirooka, and M. Nakazawa, "Single-channel 1.92 Tbit/s, pol-mux-64 QAM coherent pulse transmission over 150 km with a spectral efficiency of 7.5 bit/s/Hz," *Opt. Exp.,* 22(20), 23776-23785 (2014).

[28] D. O. Otuya, K. Kasai, T. Hirooka, and M. Nakazawa, "Single-channel 1.92 Tbit/s, 64 QAM coherent Nyquist orthogonal TDM transmission with a spectral efficiency of 10.6 bit/s/Hz," *J. Lightwave Technol.*, to be published, (2016).

Chapter 2

Principle of digital coherent pulse transmission

In this chapter, I first, describe the basic configuration of a coherent pulse transmission system. After describing the basic configuration, which is shown in Fig. 2.1, I go on to describe the principle of operation of the individual key components and devices at the transmitter and receiver. In particular, I focus on how these components are improved or optimized for coherent pulse transmission. This includes a coherent pulse source, optical phase-locked loop (OPLL) for highly precise phase synchronization, OTDM demultiplexer, and digital signal processor. Regarding a coherent pulse source, since a mode-locked pulse laser that can directly emit a coherent pulse has not been realized, I developed an optical comb generation scheme. Specifically, a coherent pulse is generated with a frequency-stabilized CW laser followed by an optical comb generator and chirp compensation. Unlike a pulse generation using fiber nonlinearities such as supercontinuum generation, this scheme is advantageous in terms of maintaining high coherence. As regards the OPLL, I improved the OPLL configuration to realize the phase synchronization between CW-LO and transmitted coherent pulses by newly introducing comb generation with an LN phase modulator inside the feedback loop. The fundamental components described in this chapter are used in the transmission experiments I carried out in chapters 3, 4 and 5.

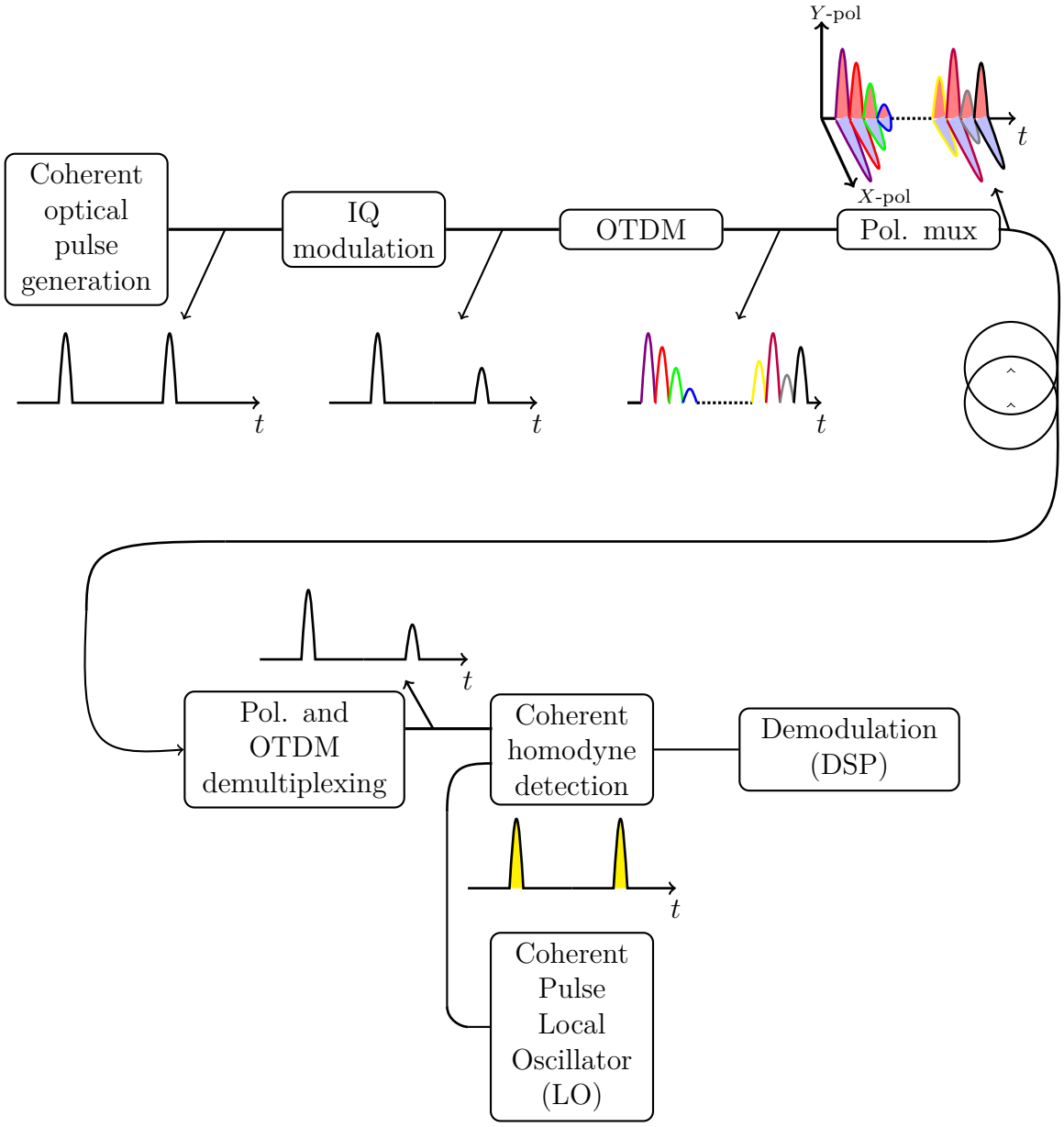

Figure 2.1: A basic configuration of a coherent pulse transmission system

2.1 Coherent pulse generation

The coherent pulse generation circuit consists of a coherent CW laser [1], an ultrabroad comb generator [2] and a pulse shaper [3]. As a coherent CW laser, a fiber laser whose frequency is stabilized to the absorption lines of ($^{13}C_2H_2$) at 1538.8 nm is described in detail in section 2.1.1.

The output from the CW fiber laser is fed into an ultrabroad comb generator giving rise to a broad comb. As an ultrabroad comb generator, a dual drive Mach-Zehnder (MZ) modulator which is driven by an RF signal of different phase and amplitude is described in detail in section 2.1.2.

From the broad comb a pulse was carved off using a pulse shaper. As a pulse shaper, a programmable optical filter consisting of a spatial amplitude and phase modulator based on liquid crystal on silicon (LCoS) is presented in detail in subsection 2.1.3. The filter is programmed so that the envelope of the longitudinal modes of the frequency comb is converted to a Gaussian or Nyquist spectral profile.

2.1.1 Acetylene frequency-stabilized fiber laser

In this subsection, the structure and operation of the frequency-stabilized fiber laser is described.

Figure 2.2 shows the structure of the frequency-stabilized laser. The laser is composed of a fiber-ring laser cavity, in which an erbium-doped fiber (EDF) is pumped by an InGaAsP laser diode (LD) operating at 1.48 μm through a WDM coupler. The EDF is wound on a piezo-electric transducer (PZT) for tuning the laser cavity length. The cavity includes a very narrow filter made of fiber-bragg grating (FBG) which was stuck on a multi-layer PZT (MLP). The MLP is controlled by a voltage output from a phase sensitive circuit. The control voltage to the MLP changes the length of the MLP, and in effect the period of the FBG thereby shifting the FBG center frequency. In order to carry out single mode operation, the FBG had to be very narrow and in this case the it had a bandwidth of 1.3 GHz and a suppression ratio of 20 dB on the side modes. This enabled single mode operation of the laser. The circulator acted as an isolator allowing only single-directional optical flow limiting the hole-burning effect. So as to stabilize the polarization state, the entire ring-cavity was made of polarization maintaining (PM) fiber. The laser output is obtained through a 80 : 20 output coupler.

In order to stabilize the frequency to the C_2H_2 absorption line, part of the of the optical output was fed into a frequency stabilization circuit, in which a frequency deviation from the C_2H_2 absorption line is detected and fed back to the PZT to control the laser frequency. The acetylene absorption

line used was $P(10)$ at 1538.80 nm whose linewidth is 500 MHz. The output power from the laser was 20 mW, with the linewidth of 4 kHz.

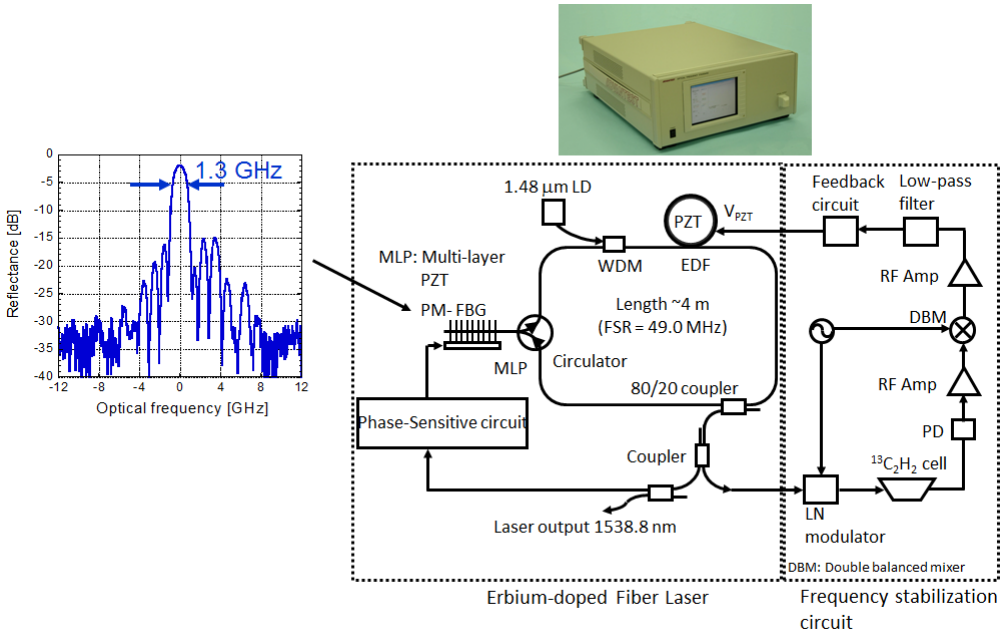

Figure 2.2: Frequency stabilized fiber laser

2.1.2 Ultrabroad comb generation

The structure and operation of the optical comb generator is described in this subsection. Figure 2.3 shows the configuration of a comb generator [2]. The two arms of the MZM modulator are driven by RF signals with the same frequency but with different amplitude and phase. The RF signals to the upper arm and the lower arm are given a phase difference of $\Delta\phi$ as shown in Fig. 2.3. To illustrate the principle of operation of the comb generator, the figure in Fig. 2.3 can be schematically represented by the figure shown in Fig. 2.4. The CW optical output from the frequency-stabilized fiber laser represented by E_{in}. The monochromatic optical signal is fed into the MZM where it is split into the two arms. The two arms were modulated independently by the signal $A_1 sin(\omega_m t)$ and $A_2 sin(\omega_m t)$, respectively. The phase of the two signals is defined as θ_1 and θ_2. The output from the two arms, E_1 and E_2 can be defined as

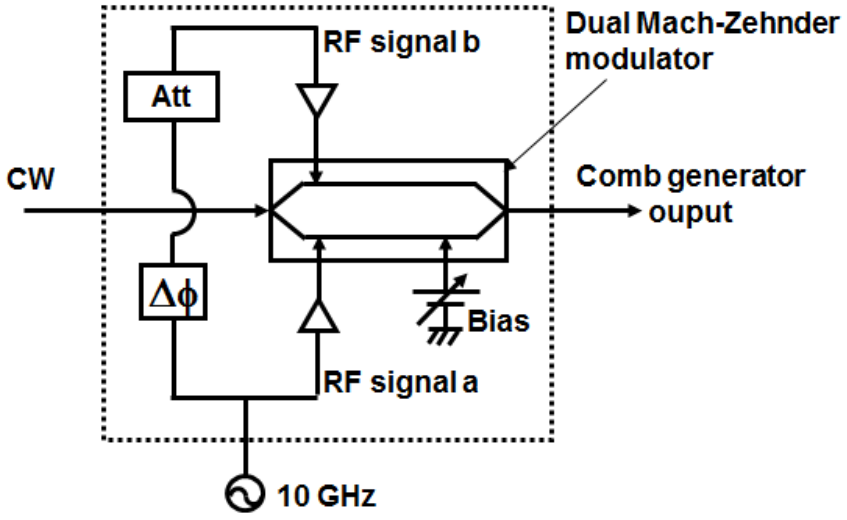

Figure 2.3: The configuration of a comb generator

$$E_1 = \frac{E_{in}}{\sqrt{2}} exp(j(A_1 \sin(\omega_m t) + \theta_1)) \tag{2.1}$$
$$E_2 = \frac{E_{in}}{\sqrt{2}} exp(j(A_2 \sin(\omega_m t) + \theta_2))$$

The two signals E_1 and E_2 are coupled, whose output E_{out}, can be expressed as

$$\begin{aligned} E_{out} &= E_1 + E_2 \\ &= \frac{E_{in}}{2}(exp(j(A_1 \sin(\omega_m t) + \theta_1)) + exp(j(A_2 \sin(\omega_m t) + \theta_2))) \\ &= \frac{E_{in}}{2} \sum_{k=-\infty}^{\infty} J_k(A_1) exp(j(k\omega_m t + \theta_1)) + J_k(A_2) exp(j(k\omega_m t + \theta_2)) \end{aligned} \tag{2.2}$$

where $J_k()$ is Bessel function of the first kind. The CW source E_{in} can be expressed as $E_{in} = |E_{in}| exp(j\omega_c t)$, therefore the result in equation (2.2) can then be expressed as

$$E_{out} = \frac{|E_{in}|}{\sqrt{2}} \sum_{k=-\infty}^{\infty} J_k(A_1) exp(j(\omega_c + k\omega_m t + \theta_1)) + J_k(A_2) exp(j(\omega_c + k\omega_m t + \theta_2)) \tag{2.3}$$

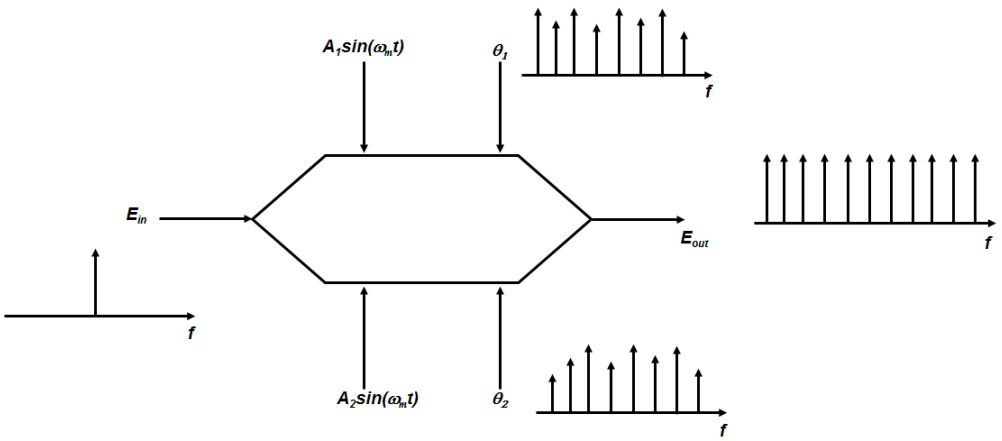

Figure 2.4: The configuration of a comb generator

The Fourier transform for equation (2.3) is given by

$$
\begin{aligned}
F\left[E_{out}\right] &= \frac{|E_{in}|}{2} \sum_{k=-\infty}^{\infty} \left[J_k(A_1)exp(j(\theta_1)) + J_k(A_2)exp(j(\theta_2))\right] \qquad (2.4)\\
&\times \int_{-\infty}^{\infty} exp(j(\omega_c + k\omega_m - \omega)t)dt \\
&= \frac{|E_{in}|}{2} \sum_{k=-\infty}^{\infty} \left[J_k(A_1)exp(j(\theta_1)) + J_k(A_2)exp(j(\theta_2))\right] \delta(\omega - \omega_c - k\omega_m)
\end{aligned}
$$

From equation (2.4), the k^{th} power spectral density P_k can be expressed as

$$
\begin{aligned}
P_k &= \frac{|E_{in}|^2}{2} |J_k(A_1)exp(j\theta_1) + J_k(A_2)exp(j\theta_2)|^2 \qquad (2.5)\\
&= \frac{|E_{in}|^2}{2} (J_k(A_1)exp(j\theta_1) + J_k(A_2)exp(j\theta_2))(J_k(A_1)exp(j\theta_1) + J_k(A_2)exp(j\theta_2))^* \\
&= \frac{|E_{in}|^2}{2} (J_k(A_1)exp(j\theta_1) + J_k(A_2)exp(j\theta_2))(J_k(-A_1)exp(-j\theta_1) + J_k(-A_2)exp(-j\theta_2)) \\
&= \frac{|E_{in}|^2}{2} (J_k^2(A_1) + J_k^2(A_2) + J_k(A_1)J_k(A_2)(exp(j(\theta_1 - \theta_2)) + exp(-j(\theta_1 - \theta_2)))) \\
&= \frac{|E_{in}|^2}{2} (J_k^2(A_1) + J_k^2(A_2) + 2J_k(A_1)J_k(A_2)\cos(\theta_1 - \theta_2))
\end{aligned}
$$

When A_i, $i = 1, 2$ is large enough, the Bessel function $J_k(A_i)$ can be approximated to

$$J_k(A_i) \approx \sqrt{\frac{2}{\pi A_i}} \cos(A_i - \frac{2k+1}{4}\pi) \tag{2.6}$$

Taking this approximation into account, the equation (2.5) can be approximated to

$$\begin{aligned} P_k \approx \frac{|E_{in}|^2}{\pi} \Bigg[& \frac{1}{A_1} \cos^2(A_1 - \frac{2k+1}{4}\pi) + \frac{1}{A_2} \cos^2(A_2 - \frac{2k+1}{4}\pi) \\ & + \frac{2}{\sqrt{A_1 A_2}} \cos(A_1 - \frac{2k+1}{4}\pi) \cos(A_2 - \frac{2k+1}{4}\pi) \cos(\theta_1 - \theta_2) \Bigg] \end{aligned} \tag{2.7}$$

Taking $\tilde{A} = (A_1 + A_2)/2$, $\Delta A = (A_1 - A_2)/2$ and $\Delta\theta = (\theta_1 - \theta_2)/2$, $2\Delta A$ and $2\Delta\theta$ are the amplitude and phase differences on the two arms respectively. If ΔA is too small, the approximation $A_1 \approx A_2 \approx \tilde{A}$ can be made. Therefore, the equation (2.7) can be further approximated to

$$\begin{aligned} P_k &\approx \frac{|E_{in}|^2}{\pi\tilde{A}} \Bigg[\cos^2(A_1 - \frac{2k+1}{4}\pi) + \cos^2(A_2 - \frac{2k+1}{4}\pi) \\ &\quad + 2\cos(A_1 - \frac{2k+1}{4}\pi) \cos(A_2 - \frac{2k+1}{4}\pi) \cos(2\Delta\theta)) \Bigg] \\ &= \frac{|E_{in}|^2}{\pi\tilde{A}} \Bigg[1 + \frac{1}{2}\cos(2A_1 - \frac{2k+1}{2}\pi) + \frac{1}{2}\cos(2A_2 - \frac{2k+1}{2}\pi) \\ &\quad + [\cos(A_1 + A_2 - \frac{2k+1}{2}\pi) + \cos(A_1 - A_2)] \cos(2\Delta\theta) \Bigg] \\ &= \frac{|E_{in}|^2}{\pi\tilde{A}} \Bigg[1 + \cos(A_1 + A_2 - \frac{2k+1}{2}\pi) \cos(A_1 - A_2) \\ &\quad + [\cos(2\tilde{A} - \frac{2k+1}{2}\pi)] \cos(2\Delta\theta) \Bigg] \\ &= \frac{|E_{in}|^2}{\pi\tilde{A}} \Bigg[1 + (\cos(2\Delta A) + \cos(2\Delta\theta)) \cos(2\tilde{A} - \frac{2k+1}{2}\pi) \\ &\quad + \cos(2\Delta A) \cos(2\Delta\theta)] \end{aligned} \tag{2.8}$$

If $P_{in} = |E_{in}|^2$, the conversion efficiency for the k^{th} harmonic can be expressed

as

$$\eta_k = \frac{P_k}{P_{in}} = \frac{1}{\pi\tilde{A}}\Big[1 + (\cos(2\Delta A) + \cos(2\Delta\theta))\cos(2\tilde{A} - \frac{2k+1}{2}\pi) + \cos(2\Delta A)\cos(2\Delta\theta)\Big] \tag{2.9}$$

As it can be seen in equation (2.9), the conversion efficiency for the k^{th} harmonic is dependent on k. In order to obtain an ultra-flat comb, this k-dependence ought to be eliminated. This can be achieved by equating the following term to zero

$$\begin{aligned}(\cos(2\Delta A) + \cos(2\Delta\theta)) &= 0 \\ 2\cos(\Delta A + \Delta\theta)\cos(\Delta A - \Delta\theta) &= 0\end{aligned} \tag{2.10}$$

This satisfied when

$$\Delta A \pm \Delta\theta = \frac{\pi}{2} \tag{2.11}$$

The condition in equation (2.11), leads to the conversion efficiency η_k to be independent of k, and hence

$$\eta_k = \frac{1 - \cos(4\Delta\theta)}{2\pi\tilde{A}} \tag{2.12}$$

The conversion efficiency η_k attains a maximum value of

$$\eta_{k,max} = \frac{1}{2\pi\tilde{A}} \tag{2.13}$$

which is achieved when

$$\Delta A = \Delta\theta = \frac{\pi}{4} \tag{2.14}$$

is satisfied. Therefore, an ultra-flat comb can be generated when the condition represented in equation (2.14) is satisfied.

Assuming that $V_\pi = 1.75\ V$, and the phase difference between the two arms $2\Delta\theta = \pi/2$, if the amplitude difference between the two arms $2\Delta A = \pi/2$ as well, the comb shown in Fig. 2.5 is obtained. The external and internal view of the comb generator used in this work is shown in Figs. 2.6(a) and (b) respectively.

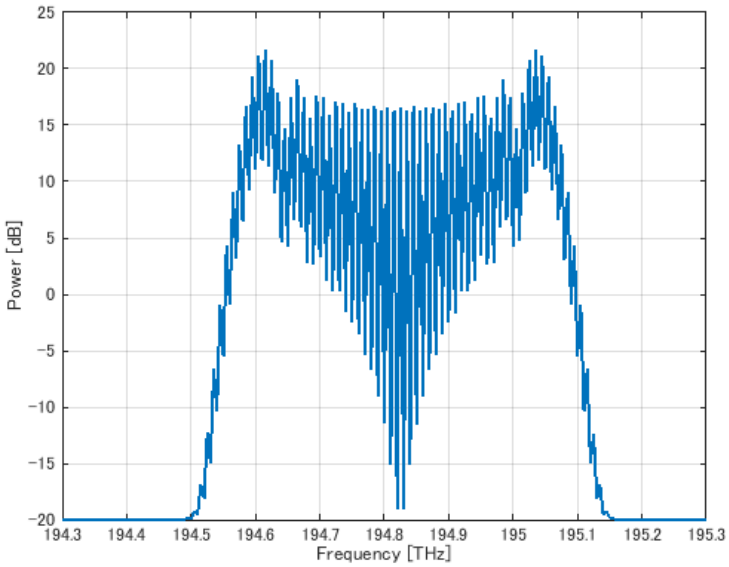

Figure 2.5: A simulated comb spectrum

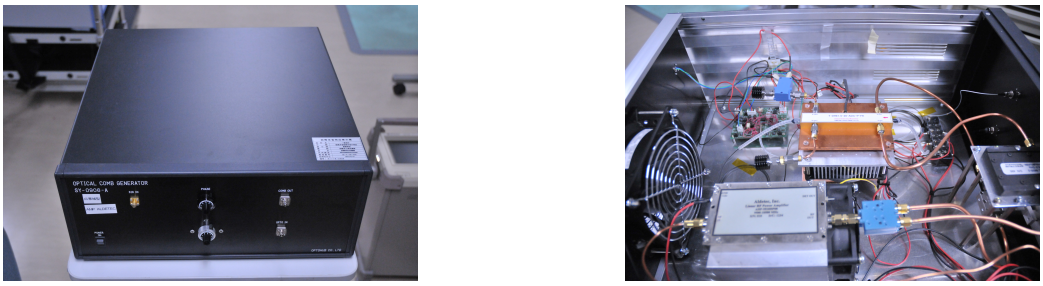

(a) External view

(b) View of the MZ modulator

Figure 2.6: The comb generator

2.1.3 Pulse shaping

This section covers the pulse shaping process employed in this work. As mentioned earlier, a programmable pulse shaper [3] was employed to carve off a desired pulse profile from the broad comb that was generated as described in subsection 2.1.2.

Figure 2.7 shows the configuration of the pulse shaper. First, the input signal passes through a set of wave plates, optimizing the polarization of the beam. The beam is then reflected by a cylindrical mirror to a diffraction grating, where the light is angularly dispersed. The different spectral components of the dispersed beam are then reflected again on the cylindrical

mirror to a liquid crystal on silicon (LCoS) surface. By programming the attenuation and phase of each pixel of the LCoS, different spectral components can be manipulated as desired and thus a filter profile can be programmed. The spectral components are reflected back to the cylindrical mirror and the output is obtained through a diffraction grating.

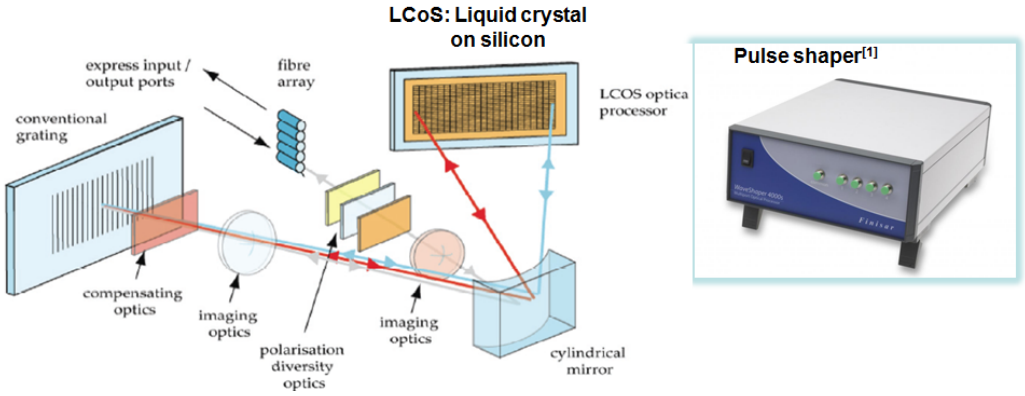

Figure 2.7: The structure of a pulse shaper

For example, if the LCoS pixels are programmed with an attenuation profile shown in Fig. 2.8(b), when the signal possessing a spectrum shown in Fig. 2.8(a) is fed into the pulse shaper, the spectrum of the signal out of the pulse shaper takes the profile shown in Fig. 2.8(c).

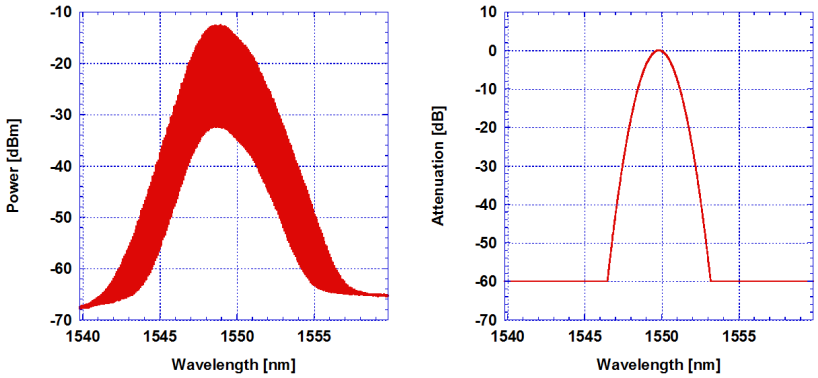

(a) Pulse shaper input

(b) Pulse shaper filter profile

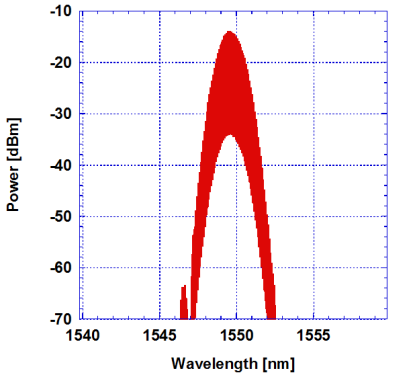

(c) Pulse shaper output

Figure 2.8: The pulse shaper filtering process

2.2 Modulation, transmission and detection of coherent pulse

This section covers key devices and components used for data modulation, multiplexing, transmission and coherent detection. The optical signal from the pulse generator is passed through an IQ modulator, where two quadrature optical beams are amplitude modulated independently. This process is explained in detail in subsection 2.2.1. The modulated data signal is then OTDM multiplexed using a PLC type OTDM multiplexer, which is described in 2.2.2. After OTDM multiplexing, the signal undergoes polarization multiplexing, which is explained in subsection 2.2.3. The multiplexed data signal is transmitted through a dispersion-managed fiber link whose details are covered in subsection 2.2.4. At the receiver, clock recovery and OTDM de-

multiplexing are carried out, which is elaborated further in subsection 2.2.5. Finally, the process of coherent detection is explained in subsection 2.2.6.

2.2.1 IQ modulator

The IQ modulation process is described here in detail. Fig. 2.9 shows the configuration of the IQ modulation used. It is an SSB modulator made of Ti-diffused $LiNbO_3$ (LN) waveguides indicated by the black lines in Fig. 2.9 [4].

The modulator consists of the main interferometer MZ_C with two sub interferometers MZ_A and MZ_B placed on each arm. Furthermore, there are electrodes placed on each interferometer which adjust the refractive index of the respective waveguides in proportion to the voltage applied to them. Threfore, as illustrated in Fig. 2.9, the refractive index change on one arm of the sub interferometers can lead to a corresponding variation in the degree of interference of the optical signal through the each arm of the main interferometer MZ_C.

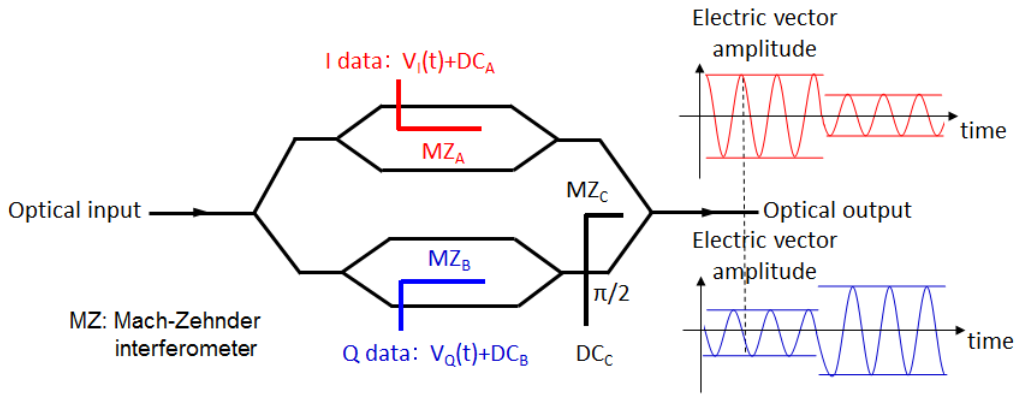

Figure 2.9: The configuration of an IQ modulator

The voltage applied to the two sub interferometers result in an optical transmittance that takes the sin-curve as shown in Fig. 2.10. By setting the DC voltage to the electrodes such that the transmittance is zero (null-point), amplitude modulated electrical data can be applied to the electrodes on two arms independently such that the optical transmittance through the two arms follows the sin-curve distribution shown in Fig. 2.10. Ideally, when the DC voltage (DC-bias) V_0 is applied, the transmittance is zero, however when random I- and Q-data are fed to the upper and lower V_0-biased sub interferometers respectively, having an allowable range of of $-V_\pi \sim +V_\pi$, their optical transmittances change following a sin-curve.

Furthermore, a DC-voltage can be applied to one of the arms on the main interferometer MZ_C such that the phase difference between the arms results in the two independently amplitude modulated beams to be quadrature or orthogonal to other, hence quadrature amplitude modulated (QAM) data.

In the course of this work, IQ modulators of V_π around 2.5 V was used. The exact values of the driving voltage will be provided in successive chapters and when the respective experiments is described.

The loss on the optical signal through the IQ-modulator can be broken down into the following:

1 The intrinsic insertion loss of the modulator, which was about 5 dB for this case.

2 Loss due to the level of modulation depth used, i.e, the peak to peak voltage value of the I- and Q- data used.

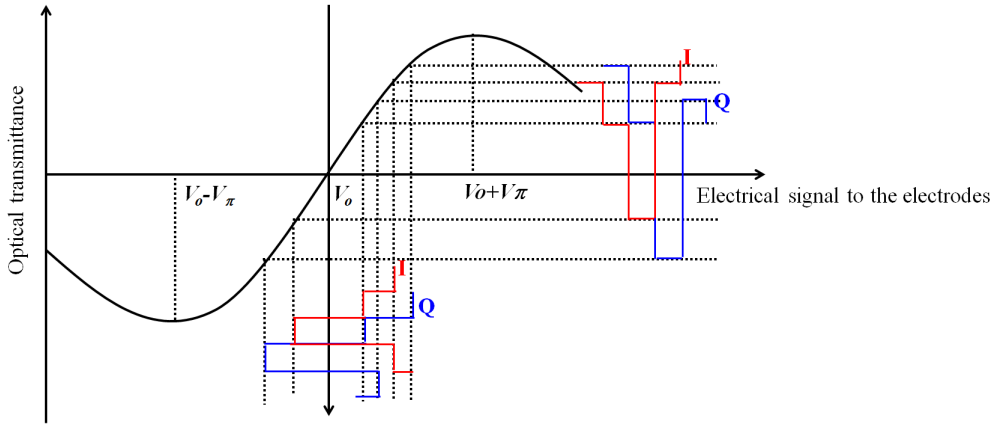

Figure 2.10: The principle of IQ modulation

2.2.2 OTDM multiplexer

The configuration of optical time division multiplexing (OTDM) circuit is shown in Fig. 2.12. For simplicity, a single data channel is multiplexed through several stages eventually increasing the baud rates. First, a pulse train of base repetition rate, for example 10 GHz in Fig. 2.12, is modulated and fed into the OTDM multiplexer. The multiplexer contains several multiplexing steps where on each step the signal is divided into two arms, with one arm given a delay relative to the other. In the particular example shown in Fig. 2.12, a 10 Gbaud data train is split into two arms. One arm is delayed

by 150 ps relative to the second arm and then combined giving rise to a 20 Gbaud data train. The reason for setting the delay to be 150 ps instead of 50 ps is to reduce the correlation between neighboring pulses after OTDM. The 20 Gbaud pulse data train is then divided into two branches with arm given a 75 ps delay relative to the other, giving rise to a 40 Gbaud data train. The third step involves splitting the 40 Gbaud into two, and one arm delayed by 37.5 ps, giving rise to an 80 Gbaud data train when finally recombined. The last stage involves giving one arm a delay of 18.75 ps, resulting in a 160 Gbaud data signal when the two arms are combined again. Generally, the aggregate baud rate is given by the baseline (initial) baud rate multiplied by 2 raised to the number of multiplexing steps n, i.e., (2^n). In this work, the bit-delay line interleaver is implemented on a planar lightwave circuit (PLC).

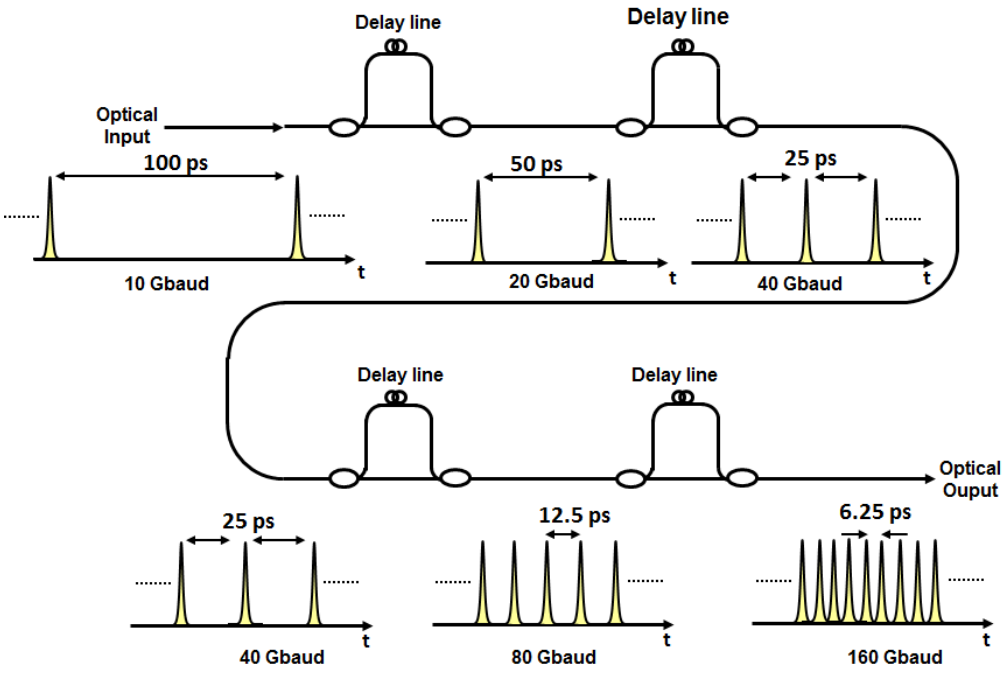

Figure 2.11: The configuration of an OTDM multiplexer

In practical implementations, unlike with the laboratory experiments where all the OTDM tributaries consist of the same modulated data, practical systems would entail different tributaries carrying different data or serving different clients. The main advantage of OTDM is that it makes it possible for generation of serial data rates that exceed limits set by data generation by electronics.

2.2.3 Polarization multiplexing

While OTDM multiplexing increases the serial baud rate greatly, it is also possible to further take advantage of ability of both TE and TM modes to coexist in a single fiber and hence double the bit rates that can be transmitted through the fiber.

For polarization multiplexing to be achieved, first the signal is split into two arms using a 50 : 50 optical coupler. The signal on one arm is given a delay, while the polarization state of the signal on the arm is rotated using a polarization controller (PC) such that it is perpendicular to that of the other arm. The two beams are then combined using a polarization beam combiner (PBC), with the resultant signal having a bit rate twice that at the input. In order to decorrelate the two polarization channels, a delay of about 1 ns is introduced between the two arms.

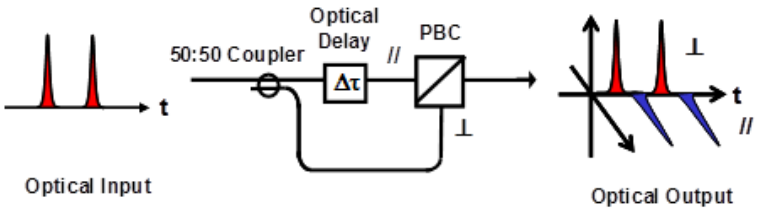

Figure 2.12: The principle of polarization multiplexing

2.2.4 Dispersion-managed fiber link

In this subsection details on the dispersion-managed fiber (DMF) used in this work is explained. When narrow pulses propagate through fiber of large dispersion and dispersion slope, they broaden and that leads to signal degradation during detection. Furthermore, for proper clock extraction at the receiver, the pulse broadening must be compensated for precisely. Therefore, dispersion compensation is indispensable.

A fiber whose dispersion is close to zero such as dispersion-shifted fiber (DSF) are not ideal for optical coherent transmission due to the enhanced nonlinear phase rotation during data signal propagation. Here, a fiber of large core effective area known as super large area (SLA) fiber is adopted. The SLA used in this work was of length 50 km/span, core effective area A_{eff} of 106 μm^2, dispersion of 19.5 ps/nm/km and a dispersion slope of 0.06 $ps/nm^2/km$. To compensate for the anomalous dispersion in the SLA, a fiber with the dispersion and dispersion slope having the opposite sign was used. The fiber used was inverse dispersion fiber (IDF), whose length was 25

km/span, core effective area of 31 μm^2, dispersion of -40 ps/nm/km and the dispersion slope of $-$ 0.12 $ps/nm^2/km$. IDF enables simultaenous compensation of dispersion and dispersion slope. The detailed fiber configuration and property are illustrated in Fig. 2.13. The residual uncompensated dispersion was compensated for using small lengths of single mode fiber (SMF) or dispersion compensating fiber (DCF) of dispersion < 0.1 ps/nm.

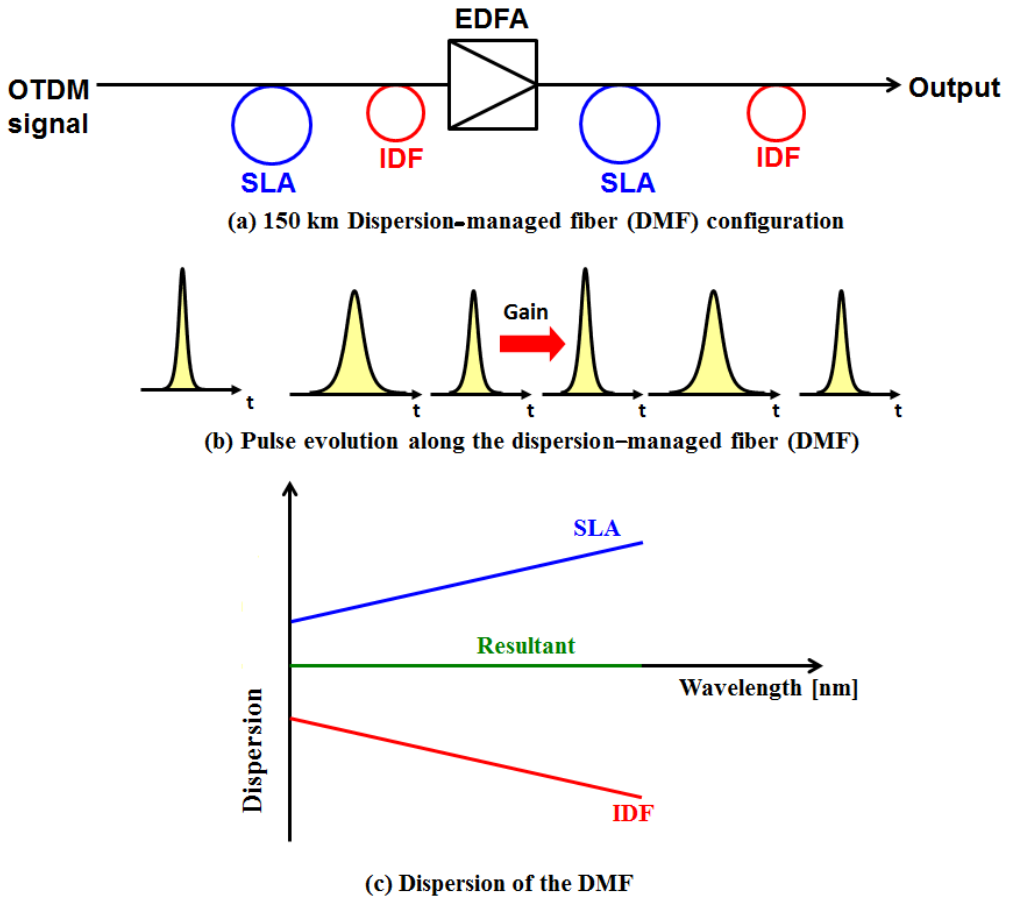

Figure 2.13: Dispersion-managed fiber (DMF) link

2.2.5 OTDM demultiplexing

OTDM demultiplexing is described in this subsection. In this work, I used a nonlinear optical loop mirror (NOLM) [5] for the OTDM demultiplexing process. Here, the focus is on the operation principle of NOLM, its structure, and characteristics. In order to carry out optical switching, a control pulse

that is synchronized to the data signal has to be generated. Therefore a reference clock that contains the repetition rate has to be either transmitted with the data or extracted from the data signal itself. In this work a mechanism that involved clock extraction from the data signal was adopted and the principle of this process is also discussed in this subsection.

(a) Optical switching by Nonlinear optical loop mirror (NOLM)

NOLM is an optical interferometer whose principle of operation is based on Sagnac interferometry [6]. The configuration of a NOLM is shown in Fig. 2.14, where the OTDM signal E_{OTDM} is coupled to a loop of highly non-linear fiber (HNLF) via a 50 : 50 coupler. There is also a separate signal called the control signal E_{cntrl} that is fed into the counter-clockwise direction via a coupler. With no control signal fed into the loop, the OTDM signal is divided into two counter-propagating beams which end up back at the coupler, where they interfere constructively and the signal is coupled to the input port.In this case, the entire OTDM signal is reflected back through the input port with no signal out of the output port, hence the name "mirror." To compensate for fiber birefringence, a polarization controller is sometimes placed in the middle of the NOLM loop. NOLM acts as a switch in such a way that when a control pulse train is fed into the loop, the phase of the data signal propagating in the counter-clockwise direction gets modulated by cross phase modulation (XPM), and induces a phase change $\Delta\Phi$ to the co-propagating beam relative to the beam travelling in the opposite direction. When this phase change is equal to π, instead of being reflected back through the input port, the signals aligned to the control pulse get transmitted through the output port. Hence, the control pulse train switches the tributary of interest through the output port.

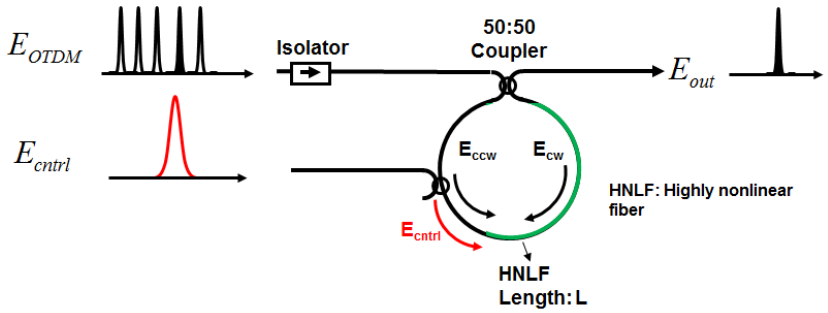

Figure 2.14: NOLM operation and OTDM demultiplexing

Next, the analytical description of the NOLM operation is presented. First, when we consider the case when the control pulse train is fed into the

NOLM, the clockwise beam E_{cw} and the counter-clockwise beam E_{ccw} after a 3-dB coupler can expressed as a function of the input OTDM signal E_{OTDM} as follows:

$$\begin{aligned} E_{cw}(0) &= i\frac{E_{OTDM}}{\sqrt{2}} \\ E_{ccw}(0) &= \frac{E_{OTDM}}{\sqrt{2}} \end{aligned} \tag{2.15}$$

.

When the control pulse is co-propagating with E_{ccw} then the XPM-induced phase change $\Delta\Phi = 2\gamma LP_{cntrl}$ is given to E_{ccw}, through the propagation in HNLF over a length of L. As a result, the pulse envelope of the two beams become

$$\begin{aligned} E_{cw}(L) &= E_{cw}(0) \\ E_{ccw}(L) &= E_{ccw}(0)\exp(i\Delta\Phi) \end{aligned} \tag{2.16}$$

The two counter-propagating beams arriving at the 3-dB coupler are coupled out in the following manner

$$\begin{aligned} E_{reflected} &= \frac{E_{cw}(L)}{\sqrt{2}} + i\frac{E_{ccw}(L)}{\sqrt{2}} \\ E_{out} &= i\frac{E_{cw}(L)}{\sqrt{2}} + \frac{E_{ccw}(L)}{\sqrt{2}} \end{aligned} \tag{2.17}$$

When equations (2.15) and (2.16) are substituted into equation (2.17), the expression reflected $E_{reflected}$ and transmitted E_{out} beams take the form

$$\begin{aligned} E_{reflected} &= i\frac{E_{OTDM}}{2}(1+\exp(i\Delta\Phi)) \\ E_{out} &= \frac{E_{OTDM}}{2}(1-\exp(i\Delta\Phi)) \end{aligned} \tag{2.18}$$

The reflectance $R = \frac{|E_{reflected}|^2}{|E_{OTDM}|^2}$ and transmittance $T = \frac{|E_{out}|^2}{|E_{OTDM}|^2}$ of the NOLM can now be derived from equation (2.18) to be:

$$T = \frac{1}{2}(1 - \cos(\Delta\Phi)) = \sin^2(\frac{\Delta\Phi}{2}) \qquad (2.19)$$
$$R = \frac{1}{2}(1 + \cos(\Delta\Phi)) = \cos^2(\frac{\Delta\Phi}{2})$$

from which we can deduce that when the phase difference between the two counter-propagating beams is π, the transmittance is 1, while when there is no control pulse and the phase difference between the two beams is zero, then the transmittance becomes zero while all the optical signal is reflected as shown in Fig. 2.15. Therefore, by carefully adjusting the control pulse power into the NOLM such that it induces a phase difference of π to the two counter-propagating arms, i.e., $\Delta\Phi = 2\gamma LP_{cntrl} = \pi$, the tributaries that overlap with the control pulse can be switched through the output, while the remaining tributaries reflected back through the input port.

Here, one important assumption is that is the control pulse travels with the same group velocity as the OTDM signal in the counter-clockwise direction. However, in real case since the wavelength of the control pulse is usually different from that of the OTDM signal, there is a "walk-off" between the control pulse and the OTDM signal, which originates from the group velocity dispersion of the HNLF. The "walk-off" problem is a very important issue especially when very narrow pulses have to be switched through the output. There is also performance degradation attributed to time jitter on both the OTDM data signal and the control pulse train that can limit the performance of the NOLM.

(b) The clock recovery process

In order to carry out OTDM demultiplexing, a control pulse must be synchronized precisely with the transmitted OTDM tributaries. In this work, a clock recovery unit that uses a bidirectional electro-absorption (EA) modulator in combination with opto-electrical PLL is employed [7].

Figure 2.16 shows the structure of the clock recovery unit. The OTDM data signal is first fed through a 50 : 50 coupler. The optical signal from the two arms of the coupler are given a differential delay $\Delta\tau$ and then each passed through a circulator. There is also a polarization controller placed on one arm of the coupler output. The signals from the coupler outputs are then fed to the electro-absorption modulator (EAM). The other circulator outputs are then fed to a low-speed PD. The photocurrents U_1 and U_2 are then given a differential amplification using an op-AMP. The electrical signal

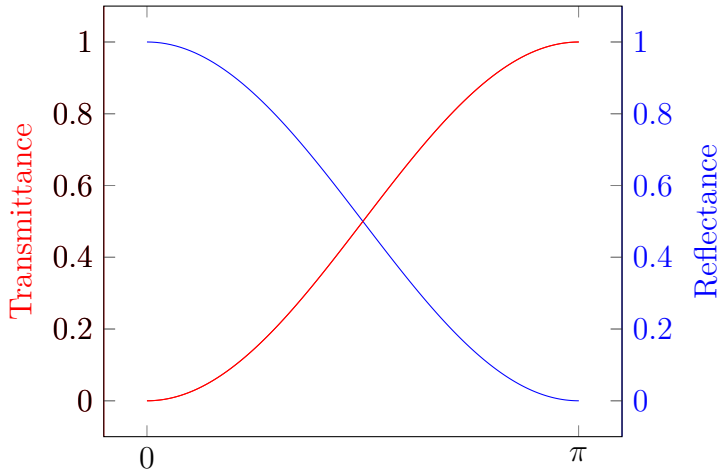

Figure 2.15: Transmittance and reflectance through a NOLM

after amplification is the passed through a low-pass filter (LPF). The signal after filtering is fed to a voltage controlled oscillator (VCO) with a 10 GHz clock signal generated at the VCO output. The clock generator does also have a 40 GHz clock output.

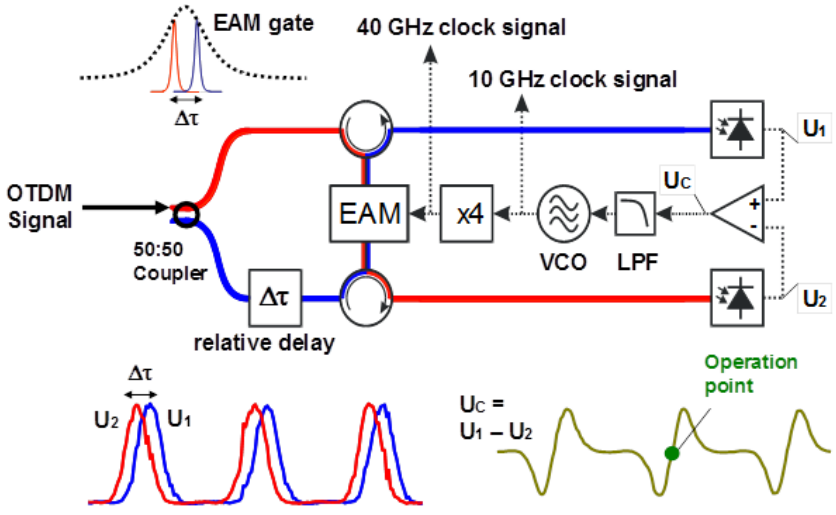

Figure 2.16: The structure of the clock recovery unit

2.2.6 Coherent detection

Intensity-Modulation/Direct-Detection (IM/DD) is widespread in communication systems today due to its simplicity and the fact that the receiver sensitivity is independent of the received signal phase and state of polarization (SOP) [8]. However, there exists a fundamental limitation to this form of detection where only the intensity is detected. On the other hand, coherent detection enables the in-phase and quadrature-phase component of the transmitted data to be detected, which makes it possible to reconstruct the optical field. This leads to an enormous advantage of being able to apply DSP for dispersion compensation and other forms of equalization by treating the received data as a complex field. This comes with great complexity in terms of having a separate optical source at the receiver known as a local oscillator (LO), whose phase must be synchronized to the data. There is also a need to precisely control the polarization signal received so that it is properly aligned to the LO signal.

Figure 2.17 shows the fundamental configuration of a simplified coherent detector. The received coherent signal E_s is combined with the optical beam from the LO, E_{LO}, into an optical coupler. The two outputs $E_1(t)$ and $E_2(t)$ from the optical mixer can be represented as

$$E_1(t) = \frac{1}{\sqrt{2}}\left[E_s + E_{LO}\right] \tag{2.20}$$
$$E_2(t) = \frac{1}{\sqrt{2}}\left[E_s + E_{LO}\exp(j\pi)\right] = \frac{1}{\sqrt{2}}\left[E_s - E_{LO}\right]$$

If the received coherent signal has a modulated envelope $A_s(t)$ and a frequency f_s, then can formulated as $E_s = A_s(t)\exp(j2\pi f_s t)$, while if the corresponding LO envelope is A_{LO} with the frequency being f_{LO}, it can be ex-

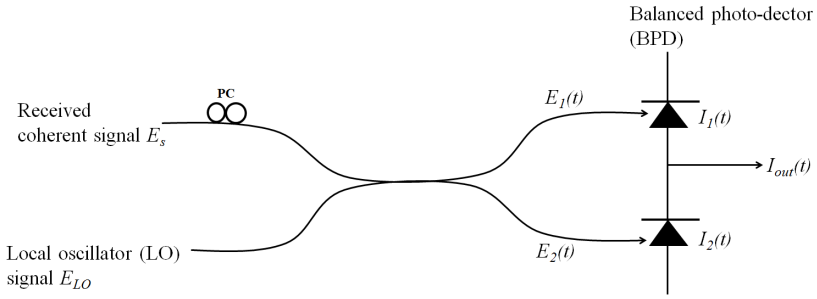

Figure 2.17: The configuration of a coherent detector

pressed as $E_{LO} = A_{LO}\exp(j2\pi f_{LO}t)$. The data signal and LO signal power can be expressed as $P_s = |A_s|^2/2$ and $P_{LO} = |A_{LO}|^2/2$, respectively.

From the above expressions, the photo-current $I_1(t)$ and $I_2(t)$ from the balanced photo-detector (BPD) becomes

$$\begin{aligned} I_1(t) &= R_0|\frac{A_s(t)\exp(j2\pi f_s t) + A_{LO}\exp(j2\pi f_{LO}t)}{\sqrt{2}}|^2 \qquad (2.21)\\ &= R_0|\sqrt{2P_s(t)}\exp(j2\pi f_s t + \phi_s(t)) + \sqrt{2P_{LO}}\exp(j2\pi f_{LO}t + \phi_{LO}(t))|^2 \\ &= R_0|\exp(j2\pi f_{LO}t)\left[\sqrt{2P_{LO}} + \sqrt{2P_s(t)}\exp(j2\pi(f_s - f_{LO})t + (\phi_s(t) - \phi_{LO}(t)))\right]|^2 \\ &= \frac{R_0}{2}|\sqrt{2P_{LO}} + \sqrt{2P_s(t)}\exp(j2\pi(f_{LO} - f_{LO})t + (\phi_s(t) - \phi_{LO}(t)))|^2 \\ &= \frac{R_0}{2}(P_{LO} + P_s(t) + 2\sqrt{P_{LO}P_s(t)}\cos(2\pi f_{IF}t + \phi_{IF}(t))) \end{aligned}$$

Similarly,

$$I_2(t) = \frac{R_0}{2}(P_{LO} + P_s(t) - 2\sqrt{P_{LO}P_s(t)}\cos(2\pi f_{IF}t + \phi_{IF}(t))) \qquad (2.22)$$

where $f_{IF} = f_s - f_{LO}$, while $\phi_{IF}(t) = \phi_s(t) - \phi_{LO}(t)$; the phase difference between the received data signal and the local oscillator. R_0 is the responsivity of the PDs [1]. The current out of the BPD $I_{out}(t)$ being the difference between the above currents is

$$\begin{aligned} I_{out}(t) &= I_1(t) - I_2(t) \qquad (2.23)\\ &= 2\sqrt{P_{LO}P_s(t)}\cos(2\pi f_{IF}t + \phi_{IF}(t)) \end{aligned}$$

The photocurrent out of the BPD is proportional to both the data signal power, and the LO signal power. Coherent detection offers an advantage where by increasing the power of the LO signal, a low power data signal can be detected at an increased sensitivity.

Coherent detection mainly takes two forms, namely heterodyne detection where the detected signal has finite intermediate frequency f_{IF}. The other form of coherent detection is a special case of heterodyne detection where the intermediate frequency is zero i.e., $f_{IF} = 0$, popularly known as "homodyne" detection.

[1] $R_0 = e\eta/2\pi f_s\hbar$ with e being the electron charge, η the quantum efficiency and $\hbar$ being Planck's constant.

(a) Heterodyne detection

As mentioned previously, *heterodyne detection* is when the intermediate frequency is finite, i.e.,$f_{IF} \neq 0$. The other implied condition is that the IF frequency is greater than the data bandwidth, otherwise the form of detection would be what is known as "intradyne" detection.

Fig. 2.18(a) shows the optical spectra for both the data signal and LO signal. As illustrated in the figure, the two frequency do not coincide. Fig. 2.18(b) shows the IF spectrum of the signal after heterodyne detection represented by the expression in equation (2.23). The main advantage of this type of detection is that linear detection is possible, where after detection the signal can be taken through a series of distortion compensation. The other merit worth mentioning is that it makes it possible for phase restoration after detection. The big limitation with this method for detection is that the IF frequency has to be greater than the data bandwidth and that puts a limitation to the bit rate taking account of the available bandwidth that can be utilized especially when using low speed electronics such as ADCs.

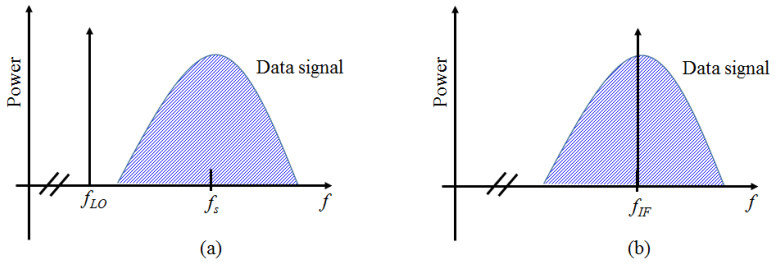

Figure 2.18: (a)optical spectrum of the data signal and LO, (b) the IF spectrum the heterodyne detected data ($f_{IF} = f_s - f_{LO} \neq 0$)

(b) Homodyne detection

Homodyne detection is a special form of heterodyne detection where the IF frequency is zero ($f_{IF} = 0$) as shown by the spectral relationship between the data signal and the LO in Fig. 2.19(a), and the baseband signal in Fig. 2.19(b). This means that the expression in equation (2.23) takes the form

$$I_{out} = 2\sqrt{P_{LO}P_s(t)}\cos(\phi_s(t) - \phi_{LO}(t)) \tag{2.24}$$

In coherent transmission, the phase component $\phi_s(t)$ of the incoming signal can be used as an important carrier of information. Therefore if the laser

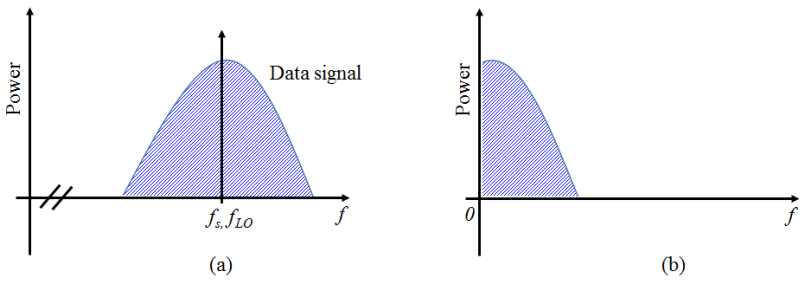

Figure 2.19: (a)optical spectrum of the data signal and LO, (b) the IF spectrum the homodyne detected data (baseband signal) ($f_{IF} = f_s - f_{LO} = 0$)

at the transmitter has an extra phase noise $\phi_n(t)$ added to the modulated phase, then the actual phase of the signal can be represented as

$$\phi_s(t) = \phi_{s\prime}(t) + \phi_n(t) \tag{2.25}$$

where, $\phi_{s\prime}(t)$ is the information carrying phase component. In order for this phase component to be properly extracted from equation (2.24) at the receiver, the local oscillator has to keep track of this time dependent phase noise or deviation. This is achieved by the adoption of an optical phase-locked loop (OPLL) which is discussed in details in section 2.3. As mentioned previously, the phase component of the current in equation (2.24) can utilized to carry information in what are called *phase diversity* coherent detection schemes. QAM data, consisting of two quadrature modulated signals require a phase-diversity coherent detection scheme. A description of how phase diverse "homodyne" coherent detection will be treated next.

(c) Phase diversity homodyne coherent detection scheme

This form of "homodyne" detection is very suitable for QAM transmission in that, both the In-phase data (I data) and the quadrature data (Q data) can be simultaneously detected. This is achieved by an extension of the coherent detector shown in Fig. 2.17 to one that is shown in Fig. 2.20. Here, both the received data signal and LO signal are each first divided into two arms, with one arm of the LO signal given a $\pi/2$ phase shift and then used for coherent detection of the second arm of the data signal. The optical outputs

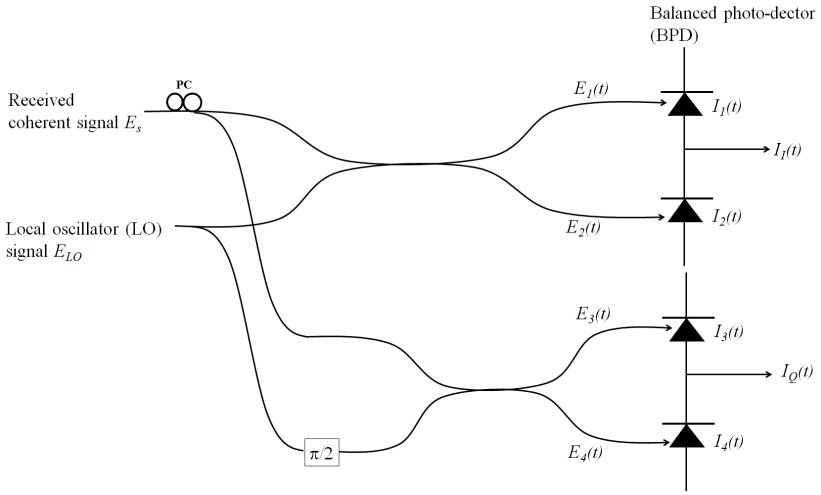

Figure 2.20: The configuration of a phase diversity coherent detector

$E_1(t) \sim E_4(t)$ can be expressed as follows:

$$
\begin{aligned}
E_1(t) &= \frac{1}{2}(E_s + E_{LO}) \\
E_2(t) &= \frac{1}{2}(E_s - E_{LO}) \\
E_3(t) &= \frac{1}{2}(E_s + jE_{LO}) \\
E_4(t) &= \frac{1}{2}(E_s - jE_{LO})
\end{aligned}
\tag{2.26}
$$

After the optical signals in equation (2.26) are detected with a set of balanced photodetectors as shown in Fig. 2.20, a set of quadrature photocurrent is obtained. The orthogonal photocurrent can be represented as:

$$
\begin{aligned}
I_I(t) &= R\sqrt{P_s P_{LO}}\cos(\phi_s(t) - \phi_{LO}(t)) \\
I_Q(t) &= R\sqrt{P_s P_{LO}}\sin(\phi_s(t) - \phi_{LO}(t))
\end{aligned}
\tag{2.27}
$$

The two photocurrents in equation (2.27) are $\pi/2$ out of phase with one another, implying that on condition that the local oscillator tracks the phase noise of the laser at the transmitter, QAM data can be "homodyne" detected, with the two quadrature data signals recovered.

The optical arrangement shown in Fig. 2.20 is known as a 90^o optical hybrid. There are several types of optical hybrids, ranging from the simple

single polarization 90^o optical hybrids with 2 inputs (data signal and LO signal) and 4 outputs ($E_1(t) \sim E_4(t)$) 2×4-port 90^o optical hybrids to the complex polarization diverse 2×8 hybrids.

2.2.7 2×4-port 90^o optical hybrid circuit

A 2×4-port 90^o optical hybrid consists of two 2 inputs (received optical signal and that from an LO) and 4 outputs (two optical signals for both I and Q data). The schematic representation of a 2×4 optical hybrid is shown in Fig. 2.21. In order to carry out coherent detection for both I and Q-data signals, the LO signal has to be divided into two branches with the one arm of the LO used to detect the I-data. The other branch is given a 90^o-phase shift and used for "homodyne" detection of the Q-data signal. Without loss of generality, we first focus on coherent detection of the I-data, if we consider the electrical field of the QAM data to be $E_s(t) = E_I(t) + jE_Q(t)$, the first coupler divides the signal into branches of $\frac{1}{\sqrt{2}}E_s(t)$ and $\frac{-j}{\sqrt{2}}E_s(t)$. The $\frac{1}{\sqrt{2}}E_s(t)$ branch is used for I-data homodyne detection. Meanwhile the LO signal is divided into two $\frac{-j}{\sqrt{2}}E_{LO}$ branches. The I-data signal after homodyne mixing results into two optical outputs $E_1 = \frac{1}{2}(E_s(t) - E_{LO})$ and $E_2 = \frac{-j}{2}(E_s(t) + E_{LO})$. After the two optical beams are detected using a balanced photodetector, the current $I_I(t)$ can be expressed as:

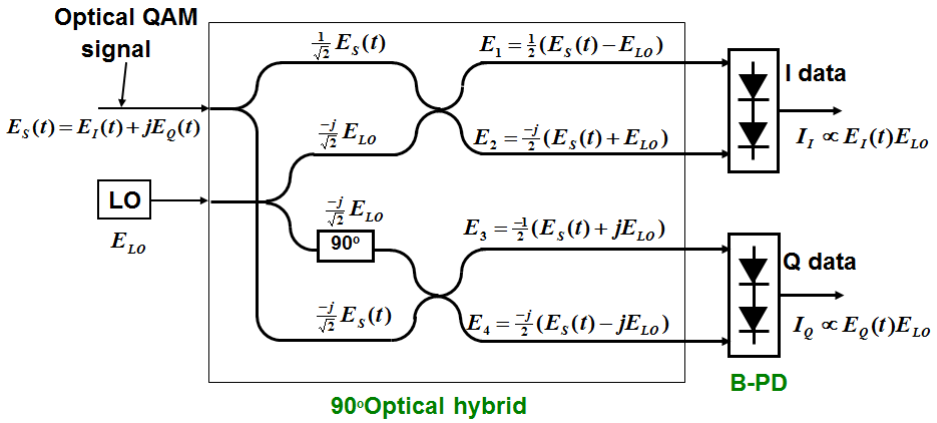

Figure 2.21: The configuration of a 2×4 90^o optical hybrid

$$
\begin{aligned}
I_I(t) &= |E_2(t)|^2 - |E_1(t)|^2 \\
&= \frac{1}{4}\{\underbrace{|E_s(t)|^2 + |E_{LO}|^2}_{selfbeat} + \underbrace{E_{LO}(E_s(t) + E_s^*(t))}_{baseband}\} \\
&- \frac{1}{4}\{\underbrace{|E_s(t)|^2 + |E_{LO}|^2}_{selfbeat} - \underbrace{E_{LO}(E_s(t) + E_s^*(t))}_{baseband}\} \\
&= E_I(t)E_{LO}
\end{aligned} \tag{2.28}
$$

The current from the Q-side of the hybrid can be expressed as:

$$
\begin{aligned}
I_Q(t) &= |E_4(t)|^2 - |E_3(t)|^2 \\
&= \frac{1}{4}\{\underbrace{|E_s(t)|^2 - |E_{LO}|^2}_{selfbeat} - \underbrace{jE_{LO}(E_s(t) - E_s^*(t))}_{baseband}\} \\
&- \frac{1}{4}\{\underbrace{|E_s(t)|^2 - |E_{LO}|^2}_{selfbeat} + \underbrace{jE_{LO}(E_s(t) - E_s^*(t))}_{baseband}\} \\
&= E_Q(t)E_{LO}
\end{aligned} \tag{2.29}
$$

2.2.8 2×8-port 90^o optical hybrid circuit

If the coherent receiver can be implemented in a polarization-diversity configuration, it is possible to receive the two polarization channels simultaneously in a polarization multiplexed transmission. This allows us to demultiplex the two polarization channels using DSP. In addition, it can be applied to compensation of nonlinear interaction between two polarizations. To compensate for the nonlinear phase rotation arising from the presence of two polarizations in the fiber, which is a phenomenon known as cross phase modulation (XPM), digital back propagation [10] can be adopted. This requires that both polarizations are simultaneously received. Unlike with the single polarization receivers which employ the 2×4 90^o optical hybrid, a polarization diversity receiver system would require a 90^o optical hybrid that can receive both polarizations. Fig. 2.22 shows the configuration of the polarization diversity 90^o optical hybrid employed in this work. As with the 2×4 90^o optical hybrid, there are two input ports to the 2×8 hybrid: one for the data signal and the other for the LO signal. There is a polarizing beam splitter (PBS) on the signal input port that separates the incoming orthogonal polarizations into the constituent principle polarization states. There is also a 50/50 beam splitter on the port for the LO signal, that divides the

signal into two equal components. There are also half waveplates ($\lambda/2$ wave plates), and quarter waveplates ($\lambda/4$ wave plates) placed on the LO and data signal paths, respectively. In Fig. 2.22, the main orthogonal components are expressed as:

$$\begin{aligned} \underline{S_1} &= S_1 \exp(j(\omega_s t + \phi(t))) \\ \underline{S_2} &= S_2 \exp(j(\omega_s t + \phi(t))) \end{aligned} \tag{2.30}$$

On the other hand, the LO signal is expressed as:

$$\underline{LO} = LO \exp(j(\omega_{LO} t)) \tag{2.31}$$

After a series of half waveplates, quarter waveplates, polarization beam splitters and 50/50 beam splitters, the X-polarization set of optical outputs from port $5 \sim 8$, while those for Y-polarization data from port $1 \sim 4$. If the optical outputs corresponding to ports $1 \sim 8$ are $\underline{E_1} \sim \underline{E_8}$, they can expressed as:

$$\left.\begin{aligned} \underline{E_1} &= \frac{1}{4}|S_2|^2 + \frac{1}{8}|LO|^2 + \frac{1}{2\sqrt{2}} S_2 LO \cos[(\omega_s - \omega_{LO})t + \phi(t)] \\ \underline{E_2} &= \frac{1}{4}|S_2|^2 + \frac{1}{8}|LO|^2 - \frac{1}{2\sqrt{2}} S_2 LO \cos[(\omega_s - \omega_{LO})t + \phi(t)] \\ \underline{E_3} &= \frac{1}{4}|S_2|^2 + \frac{1}{8}|LO|^2 + \frac{1}{2\sqrt{2}} S_2 LO \cos[(\omega_s - \omega_{LO})t + \phi(t) - \frac{\pi}{2}] \\ \underline{E_4} &= \frac{1}{4}|S_2|^2 + \frac{1}{8}|LO|^2 + \frac{1}{2\sqrt{2}} S_2 LO \cos[(\omega_s - \omega_{LO})t + \phi(t) - \frac{\pi}{2}] \end{aligned}\right\} Y - polarization \tag{2.32}$$

$$\left.\begin{aligned} \underline{E_5} &= \frac{1}{4}|S_1|^2 + \frac{1}{8}|LO|^2 + \frac{1}{2\sqrt{2}} S_1 LO \cos[(\omega_s - \omega_{LO})t + \phi(t) - \frac{\pi}{2}] \\ \underline{E_6} &= \frac{1}{4}|S_1|^2 + \frac{1}{8}|LO|^2 - \frac{1}{2\sqrt{2}} S_1 LO \cos[(\omega_s - \omega_{LO})t + \phi(t) - \frac{\pi}{2}] \\ \underline{E_7} &= \frac{1}{4}|S_1|^2 + \frac{1}{8}|LO|^2 + \frac{1}{2\sqrt{2}} S_1 LO \cos[(\omega_s - \omega_{LO})t + \phi(t)] \\ \underline{E_8} &= \frac{1}{4}|S_1|^2 + \frac{1}{8}|LO|^2 - \frac{1}{2\sqrt{2}} S_1 LO \cos[(\omega_s - \omega_{LO})t + \phi(t)] \end{aligned}\right\} X - polarization \tag{2.33}$$

After the optical signals in equation (2.32) $\sim$ (2.33) are detected using set of four balanced detectors, the photo currents for both polarizations are:

$$\left.\begin{aligned} I_{Q,X} = PD_1 &= \frac{1}{\sqrt{2}} S_1 LO \sin[(\omega_s - \omega_{LO})t + \phi(t)] \\ I_{I,X} = PD_2 &= \frac{1}{\sqrt{2}} S_1 LO \cos[(\omega_s - \omega_{LO})t + \phi(t)] \end{aligned}\right\} X - polarization \tag{2.34}$$

$$\left.\begin{aligned} I_{Q,Y} = PD_3 &= \frac{1}{\sqrt{2}} S_2 LO \sin[(\omega_s - \omega_{LO})t + \phi(t)] \\ I_{I,Y} = PD_4 &= \frac{1}{\sqrt{2}} S_2 LO \cos[(\omega_s - \omega_{LO})t + \phi(t)] \end{aligned}\right\} Y - polarization \tag{2.35}$$

Therefore, both polarizations can be effectively received and digital back propagation used to compensate for the nonlinear phase distortion that occurs during transmission in form of SPM and XPM.

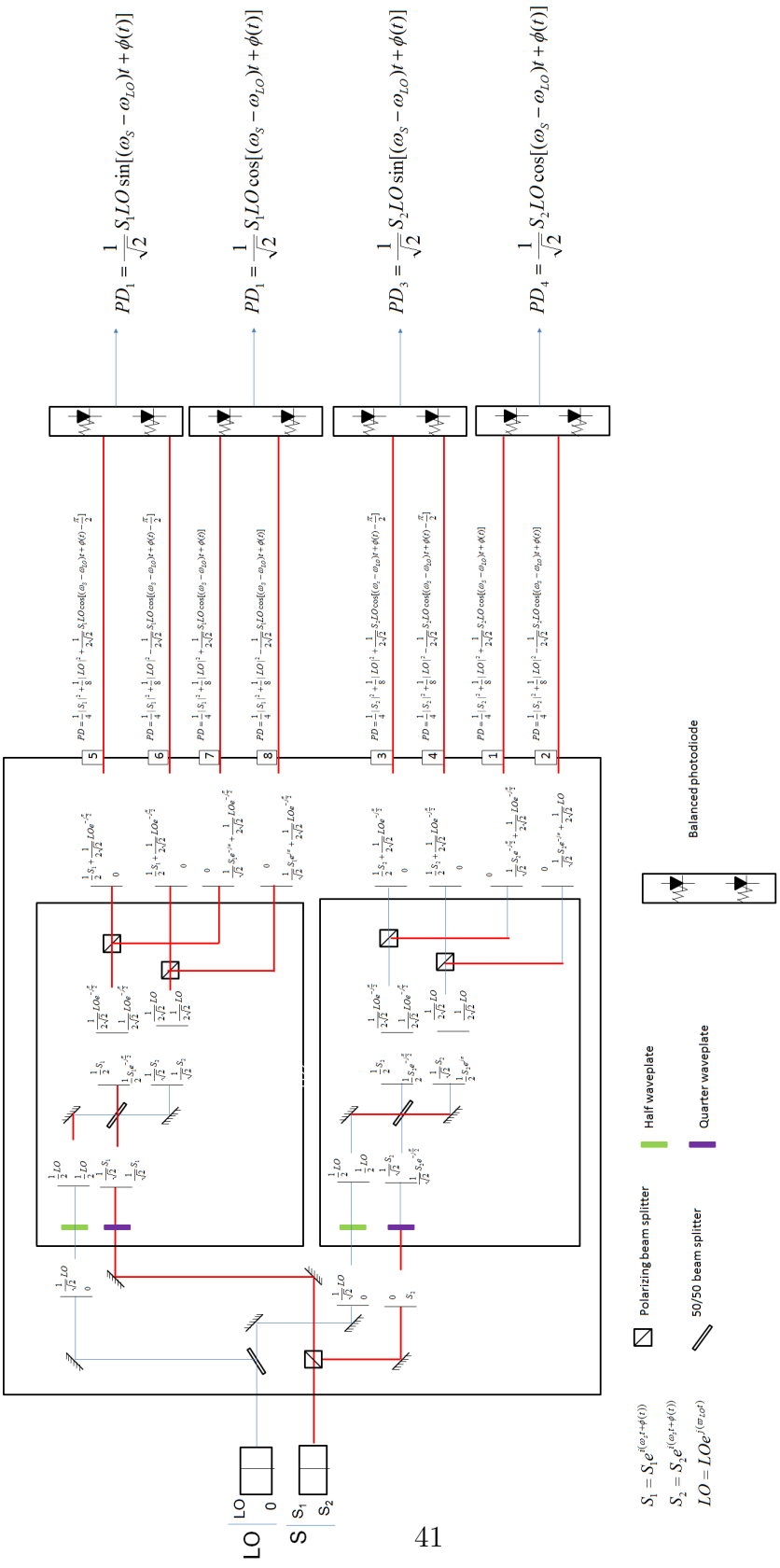

Figure 2.22: The configuration of a 2×8 90^o optical hybrid

2.3 Optical phase-locked loop (OPLL) circuit

In order to obtain stable and accurate demodulation, the local oscillator has to keep track of phase fluctuation of the incoming data signal. An OPLL circuit is a well-established technology that can be used for data-LO phase synchronization and it has so far been mainly used in CW-based optical communication. We have extended that to a coherent pulse system as illustrated in Fig. 2.23. The principle involves creating a non-modulated tone signal at the transmitter. The pilot tone signal is transmitted with the data and undergoes the same phase fluctuation as the data signal. In the receiver, a local comb is generated from a CW-LO. This is because the pilot tone is widely separated from the carrier frequency associated with the high-speed pulse transmission. As a result, higher-order harmonics of the CW-LO must be generated, whose phase is compared with that of the pilot tone. The pilot and locally generated comb signals are fed into a phase sensitive circuit where their phase difference is kept at finite difference by the reference signal from a synthesizer. Any deviation from this difference is fed back as a voltage error signal via a loop filter to the pulse generation circuit which changes the phase of the LO pulse train accordingly. The performance of an OPLL circuit is mainly measured by the amount of phase noise of the intermediate frequency signal that is coming out of the PD when the beat signal of the pilot and LO is generated. By assuming that the pilot tone signal is the nth harmonic of the comb generated at the transmitter whose repetition rate is f_R, the comb at the receiver is generated such that the repetition frequency is f_{OPLL}, and the frequency difference Δf between the pilot tone signal nf_R and the closest locally generated harmonic mf_{OPLL} is kept constant. As a result, the phase of the CW-LO can be synchronized to the phase of the data signal.

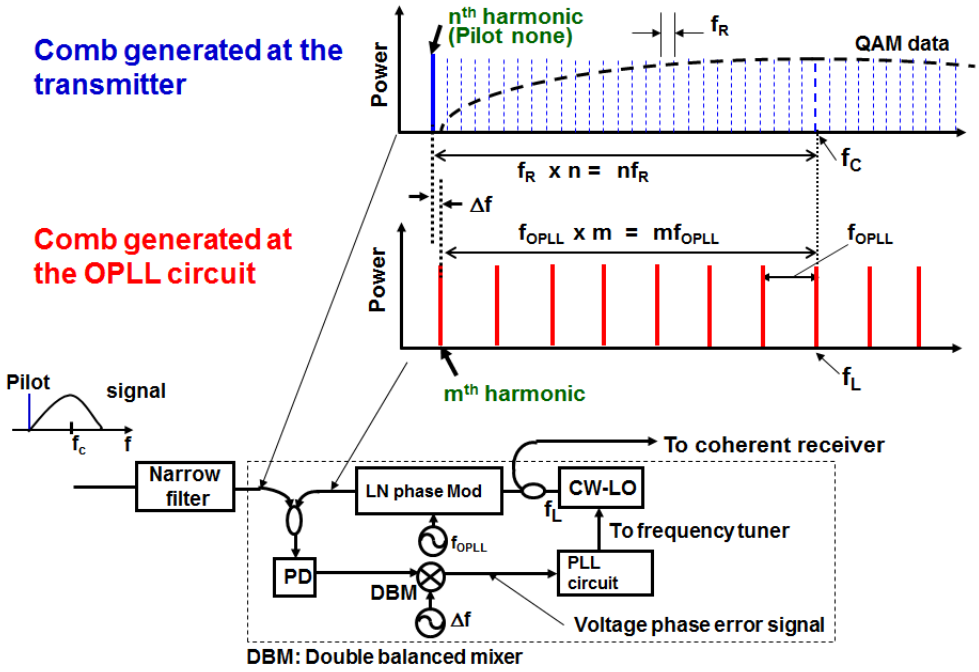

Figure 2.23: The optical phase-locked loop circuit

2.4 Waveform distortion compensation by digital signal processing

After the received QAM data signal is coherently detected, the photocurrents from the BPDs are then fed to a digital sample oscilloscope, where the analog data is converted to digital data before demodulation is carried out in an offline condition with the aid of software.

The digital sample oscilloscope used for most of this work was made by Agilent Technologies, whose vector spectrum analyzer (VSA) software was also used for the demodulation process. Fig. 2.24 outlines the individual steps that the QAM signal goes through before modulation. As shown in the figure, the I and Q-data are first converted into digital data by a set of ADCs at a fixed sampling rate. In this work at different stages we used digital oscilloscopes with sampling rates of first 40 and then 80 GSample/s at later stages.

For waveform distortion compensation, a finite impulse response (FIR) filter is widely used. An FIR filter suppresses waveform distortion, by changing the tap constants of the filter in an adaptive manner. The tap constants are sequentially updated in such as a way as to minimize the EVM of the

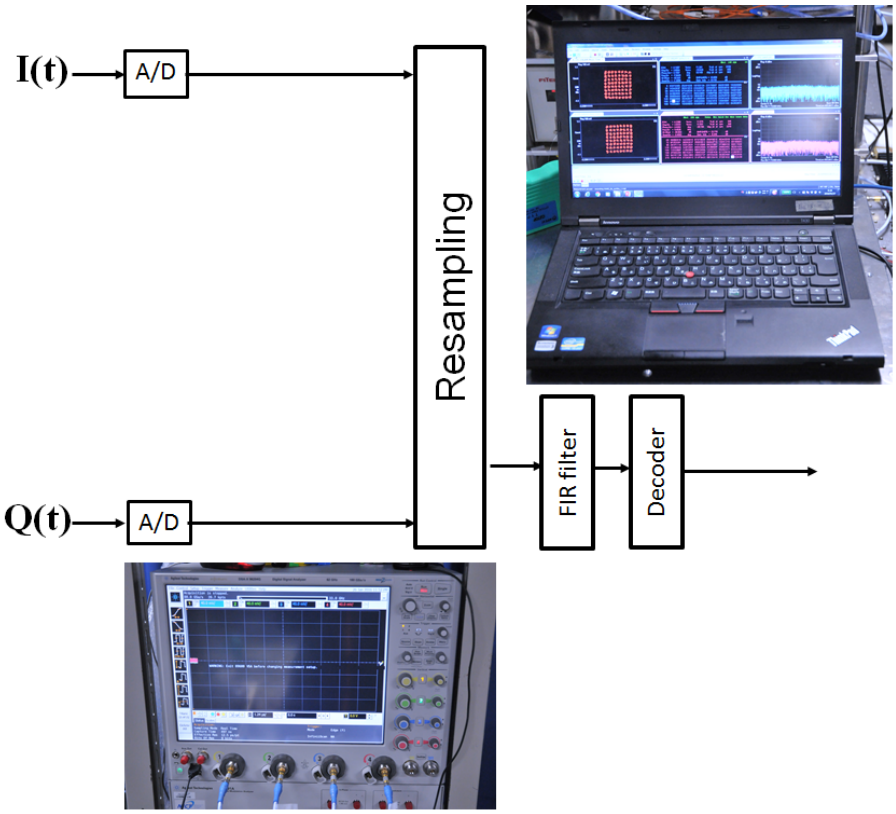

Figure 2.24: The schematic diagram of the digital processing unit

demodulated data signal.

The process of waveform distortion using an FIR filter is illustrated in Fig. 2.25. The incoming data signal $x(t)$ is branched and given incremental delays of T and weighted appropriately at each delay branch. The output output of the FIR signal can be represented as:

$$y(n) = \sum_{k=-n}^{n} h_k \cdot x(t - kT) \tag{2.36}$$

The tap constants are updated using algorithms such as the least mean square (LMS) algorithm with decision directed motion towards smaller EVM. Specifically, if the error between the output $y(n)$ and the ideal signal $d(t)$ is expressed as $e(t) = |d(t) - y(t)|$, the algorithm updates the tap constants in order to realize a minimum $e(t)$. By doing so, linear waveform distortion compensation is achieved.

The error vector magnitude (EVM) is a metric for measurement of de-

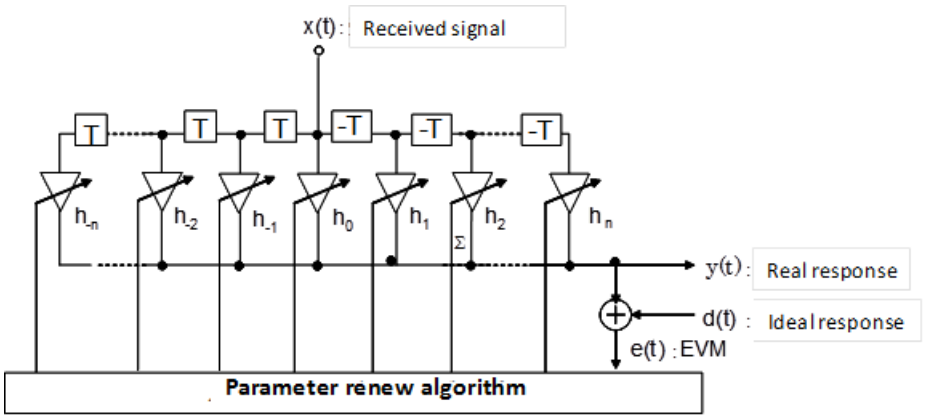

Figure 2.25: The schematic view of an FIR filter used for waveform compensation

modulation performance. EVM is a percentage representation of the total deviation of the symbols from their ideal position on the constellation map. Figure 2.26 illustrates the definition of EVM, where if we consider the measured signal to be $y(t)$, while the ideal signal is supposed to be $d(t)$, the deviation expressed as EVM is given by:

$$EVM = \frac{|y(t) - d(t)|}{|d(t)|} \times 100(\%) \tag{2.37}$$

$$= \sqrt{\frac{\sum_{n=1}^{N} |y(t) - d(t)|^2}{\sum_{n=1}^{N} |d(t)|^2}}$$

where $y(t)$ and $d(t)$ are vector quantities and the value in equation (2.37) is expressed as the root mean square of the relative deviation over N samples. This value is a very important metric in evaluation of transmission performance.

The algorithm for FIR filter equalization is shown in Fig. 2.27, where the QAM signal is received and the EVM value is estimated. If the difference between the obtained EVM and the target value is less than some value ϵ, then no further tap updates are carried out, but if the test fails, the FIR filter continues to update the filter tap weights. This process continues in a loop until the EVM value is less than a certain target value ϵ.

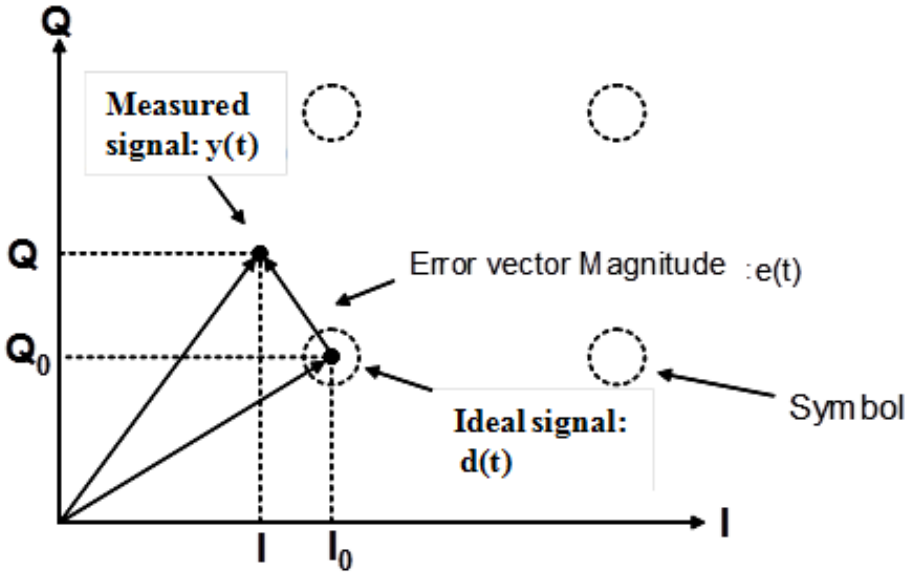

Figure 2.26: The error vector magnitude (EVM)

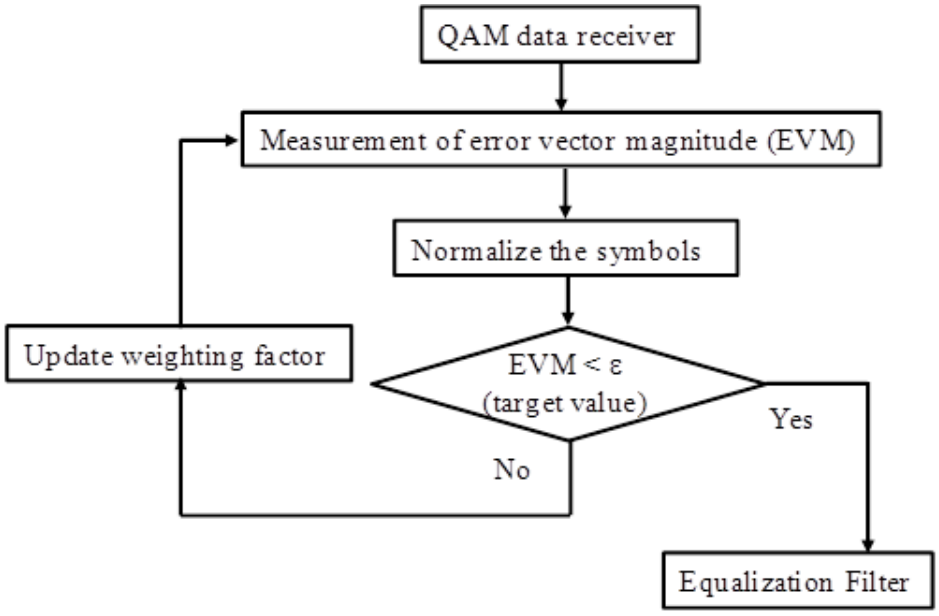

Figure 2.27: The flow chart for the equalization process when using the FIR filter

2.5 SNR improvement by RZ-CW conversion

Coherent OTDM transmission may suffer from problems such as the signal modulated on the optical carrier spreading beyond the receiver bandwidth

which leads to diminished demodulation performance. The details on this limitation is covered in more detail in subsection 2.5.1

Coherent OTDM systems, while attractive in that they exploit the high speed of light, they suffer from the input power limitation of coherent receivers. This either puts a limitation on how many tributaries can be employed or the amount of power that can be fed into the coherent receivers, leading to degradation of the demodulation performance. This is covered in more detail in subsection 2.5.2. In order to solve this problem, an RZ-CW conversion scheme is newly introduced. The technique involves first demultiplexing the incoming OTDM signal as described in section 2.5.3 and the converting the signal from a signal that is modulated on a return-to-zero (RZ) pulse carrier to one modulated on a continuous wave (CW) carrier in a process called RZ-CW conversion [3]. The principle of this process is described in subsection 2.5.3 with the proof of principle experiment results explained in subsection 2.5.4.

2.5.1 Reduction in power within the demodulation bandwidth

When using RZ pulses as compared to CW optical, the signal spreads beyond the receiver bandwidth as shown in Fig. 2.28. This means that the fraction of the power that is actually detected is smaller as compared to when CW carrier is employed. This brings about serious SNR degradation of the detected signal and hence limited performance.

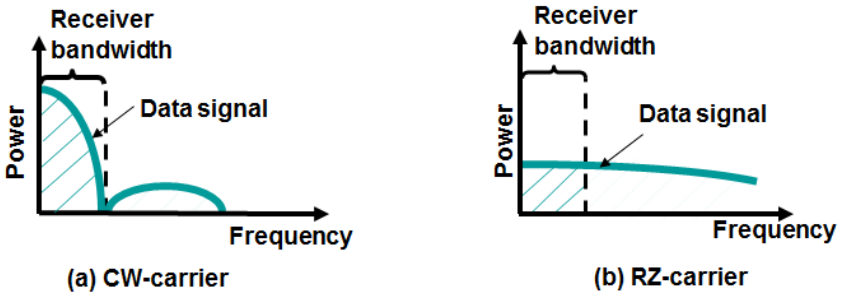

Figure 2.28: Receiver bandwidth power limitation

2.5.2 Input power limitation into the coherent detection circuit

The other big drawback to OTDM transmission is also at the receiver. As shown in Fig. 2.29, for all the N OTDM tributaries that are fed into a co-

herent receiver, only one of the tributaries is subjected to coherent detection and finally demodulation. This means that for an OTDM signal of a given power only $1/N$th of the power actually contributes to demodulation. This limitation on the power of the actual detected tributary, compounded by the bandwidth limitation of the receiver, is a serious issue that has to be overcome in coherent OTDM transmission systems.

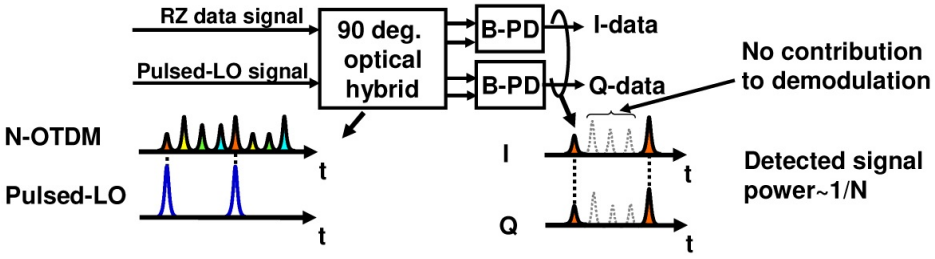

Figure 2.29: Receiver bandwidth power limitation

2.5.3 Principle of RZ-CW conversion

The principle behind RZ-CW conversion is shown in Fig. 2.30. The aim of this process is to increase the power of a pulse data within the narrow demodulation bandwidth of a coherent receiver electronics such as PD and ADCs. It involves passing the data modulated on the RZ-data via a normal dispersive medium which in effects spreads the pulse to a CW-like signal. The chirp that applied in the process of pulse spreading is cancelled out by passing the CW-like signal through a phase modulator driven so as to induce a down chirp to the signal. As a result a chirpless CW-like signal is obtained with most of its power concentrated within the bandwidth that can be fully received by the coherent receiver.

Here, I describe a simplified analytical description of the RZ-CW conversion process. If we consider the input signal into the RZ-CW conversion circuit, as shown in Fig. 2.31, to be $u_{in}(t)$. After passing through the dispersive medium of dispersion $D = \beta_2 L$ (where β_2 is the group veleocity dispersion and L the length of the fiber which is used as a dispersive medium), the spectrum of the signal $F[u_{disp}(t)] = U_{disp}(\omega)$ becomes:

$$\begin{aligned} U_{disp}(\omega) &= F[u_{in}(t)] \exp(j\frac{D}{2}\omega^2) \\ &= U_{in}(\omega) \exp(j\frac{D}{2}\omega^2) \end{aligned} \tag{2.38}$$

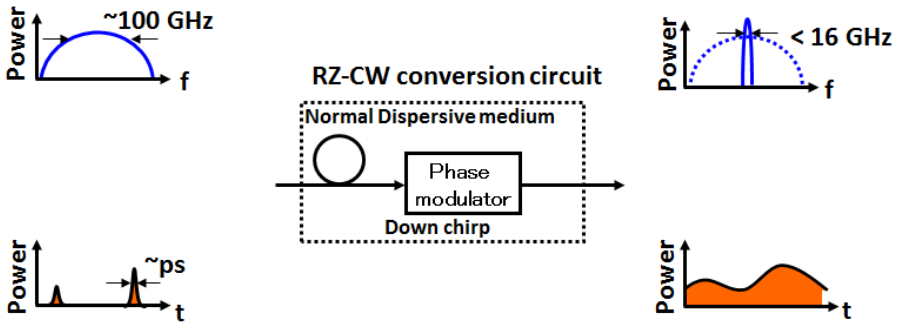

Figure 2.30: The principle of RZ-CW conversion

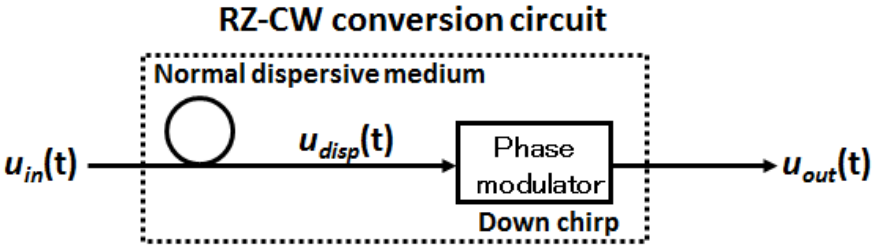

Figure 2.31: The principle of RZ-CW conversion

$u_{disp}(t)$ then can be expressed as:

$$\begin{aligned} u_{disp}(t) &= F^{-1}[U_{disp}(\omega)] \\ &= \int_{-\infty}^{\infty} U_{disp}(\omega)\exp(-j\omega t)d\omega \\ &= \int_{-\infty}^{\infty} U_{in}(\omega)\exp(j\frac{D}{2}\omega^2)\exp(-j\omega t)d\omega \end{aligned} \tag{2.39}$$

When the signal $u_{disp}(t)$ goes through a phase modulator, if we take the chirp coefficient to be K, the signal out of the phase modulator $u_{out}(t)$ becomes

$$u_{out}(t) = u_{disp}\exp(j\frac{K}{2}t^2) \tag{2.40}$$

whose spectrum is a convolution of the dispersed signal spectrum $U_{disp}(\omega)$ and the Fourier transform of the phase modulation term, which can be expressed

as

$$\begin{aligned} U_{out}(\omega) &= U_{disp}(\omega) \otimes F[\exp(j\frac{K}{2}t^2)] \\ &= \frac{1}{2\pi}U_{disp}(\omega) \otimes \sqrt{\frac{2\pi j}{K}}\exp(-j\frac{\omega^2}{2K}) \\ &= \sqrt{\frac{j}{2\pi K}}\int_{-\infty}^{\infty} U_{disp}(\omega')\exp(-j\frac{(\omega-\omega')^2}{2K})d\omega' \end{aligned} \tag{2.41}$$

By substituting equation (2.38) into equation (2.41),

$$U_{out}(\omega) = \sqrt{\frac{j}{2\pi K}}\int_{-\infty}^{\infty} U_{in}(\omega')\exp(j\frac{D}{2}\omega'^2)\exp(-j\frac{(\omega-\omega')^2}{2K})d\omega' \tag{2.42}$$

For a special case when $D = 1/K$, the expression in equation (2.42) can be condensed to:

$$\begin{aligned} U_{out}(\omega) &= \sqrt{\frac{j}{2\pi K}}\int_{-\infty}^{\infty} U_{in}(\omega')\exp(-j\frac{\omega^2}{2K} + j\frac{\omega\omega'}{K})d\omega' \\ &= \sqrt{\frac{j}{2\pi K}}\exp(-j\frac{\omega^2}{2K})\int_{-\infty}^{\infty} U_{in}(\omega')\exp(j\frac{\omega\omega'}{K})d\omega' \end{aligned} \tag{2.43}$$

If we take ω/K to be equivalent to time t, the expression in (2.43) then be considered to be the Fourier transform of $u_{in}(-\omega/K)$, such that the spectrum out of an RZ-CW conversion circuit $U_{out}(\omega)$ is

$$U_{out}(\omega) = \sqrt{2\pi jD}\exp(-j\frac{\omega^2}{2K})u_{in}(-\omega/K) \tag{2.44}$$

which means when a signal $u_{in}(t)$ is fed into an RZ-CW conversion circuit, it's time waveform becomes the shape of the spectrum of what is obtained at the output. The scaling, however, is that time $t = -\omega/K$ is transformed to ω.

For a special case when $u_{in}(t)$ is a Gaussian profile,

$$u_{in}(t) = A\exp(-\frac{t^2}{2\tau^2}) \tag{2.45}$$

The spectrum out of the RZ-CW conversion circuit takes the form

$$U_{out}(\omega) = \sqrt{2\pi j D} A \exp(-j\frac{\omega^2}{2K}) \exp(-\frac{\omega^2}{2K^2\tau^2}). \tag{2.46}$$

The spectral bandwidth (FWHM) of $U_{out}(\omega)$ in equation (2.46) is then

$$\Delta\nu = \frac{\sqrt{\ln 2}}{\pi K \tau} \tag{2.47}$$

Therefore by increasing the value of K, the spectral bandwidth can be narrowed further to approach a CW-like signal. Furthermore, looking at equation (2.46), the intensity of the signal at $\omega = 0$, i.e., $|U_{out}(\omega = 0)|^2$, can be scaled by a factor of D as well.

For an ideal RZ-CW conversion, a linear chirp denoted by the constant chirp coefficient K is preferable. However when using phase modulators such as LN modulator, the phase induced to the signal is sinusoidal and therefore not perfectly parabolic for a spectrally broad signal. For example, for an LN phase modulator driven with a signal of angular frequency ω_m, taking the peak-to-peak voltage to be V_0 and the half-wave voltage to be V_π, the phase induced on the signal through the phase modulator becomes

$$\Delta\phi = (V_0/V_\pi)\cos(\omega_m t) \tag{2.48}$$

which can be expanded around $t = 0$ using Taylor expansion to

$$\Delta\phi \approx (V_0/V_\pi)(1 - \frac{\omega_m^2}{2}t^2). \tag{2.49}$$

From equation (2.49), it can be deduced that for a phase modulator, the chirp coefficient $K = -V_0\omega_m^2/V_\pi$. Moreover, for a signal that approximates a Gaussian profile, the necessary chirp coefficient is

$$|K| = 1/|D| = 1/\tau^2 \tag{2.50}$$

Since τ is proportional to the pulse width of the Gaussian pulse, it means that the narrower the pulse, the greater the chirp coefficient needed. This means that in order to be able to provide sufficient modulation within a narrow pulse, one would need a bigger chirp coefficient.

2.5.4 Proof of concept experiment

As a proof of concept experiment, first a non-modulated pulse train was passed through an RZ-CW conversion circuit. The experimental setup is

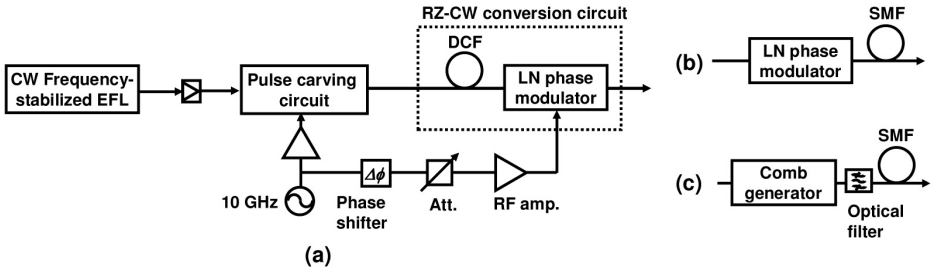

Figure 2.32: The pulse generating circuits

shown in Fig. 2.32. The pulse train was generated by a circuit composed of an acetylene frequency-stabilized fiber laser described in subsection 2.1.1. The output from this laser was used to generate a pulse in two ways. The first way consisted of feeding the CW light into a combination of an LN phase modulator and SMF. The other way involved using a comb generator [2] to generate a broad comb and carving out a pulse profile it using an optical filter. After pulse generation, the pulse was then fed to an RZ-CW conversion circuit consisting of a DCF and phase modulator. The pulse was spread from the RZ shape to a CW-like signal and the chirp cancelled out using a phase modulator.

Figure 2.33(a) shows the spectrum of the pulse train generated using the CW laser and phase modulator combination. The pulse width as shown by the waveform in Fig. 2.33(b) was abouf 10 ps. DCF of dispersion -24 ps/nm ~ -42 ps/nm was used and the spectrum and time waveform with the best conversion is shown in Fig. 2.34(a) and 2.34(b). The spectrum shown in Fig. 2.34(a) shows that the converted signal is close to a CW signal, however there are sideband components with a suppression ratio of about $25 \sim 30$ dB. This imperfect conversion can be attributed the difference in performance of the two phase modulators employed for pulse generation. The phase modulators were both driven at a modulation depth of 2.5π hence a chirp rate of $K = 0.016\ ps^{-2}$.

When using the comb generator for pulse generation, the optical spectrum and waveform are shown in Fig. 2.35(a) and 2.35(b) before RZ-CW conversion. After RZ -CW conversion, the optical spectrum and waveform take the form of what is shown in Fig. 2.36(a) and 2.36(b), respectively. When compared to when a phase modulator was used for pulse generation, there is a greater degree of imperfection to the RZ-CW conversion process. This can be attributed to the amplitude modulation that remains when the pulse passes through the comb generator. The phase modulator in the RZ-CW conversion circuit was driven at a modulation depth of 2.5π as before.

The experiment above with the two methods of pulse generation provides

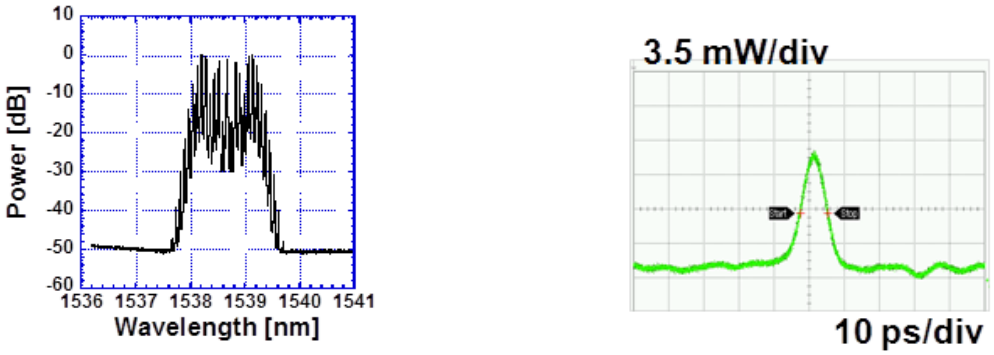

(a) Optical spectrum (b) waveform.

Figure 2.33: Optical spectrum and waveform before RZ-CW conversion

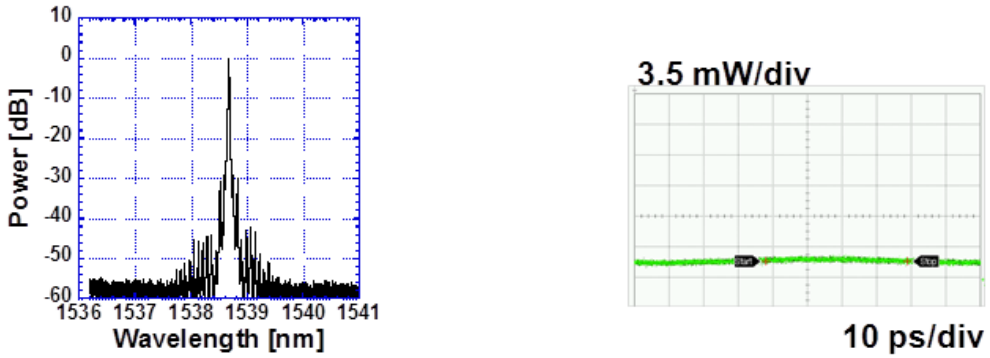

(a) Optical spectrum (b) Waveform

Figure 2.34: Optical spectrum and waveform after RZ-CW conversion

the merits and demerits on both pulse generation mechanisms. When the phase modulator was used, the waveform generated had a pedestal making it less suitable for OTDM transmission, despite the near-perfect RZ-CW conversion performance. On the other hand, when the comb generator was used, the pulse train obtained had no pedestal, with the drawback that the intensity modulation that remains leads to an imperfect RZ-CW conversion process.

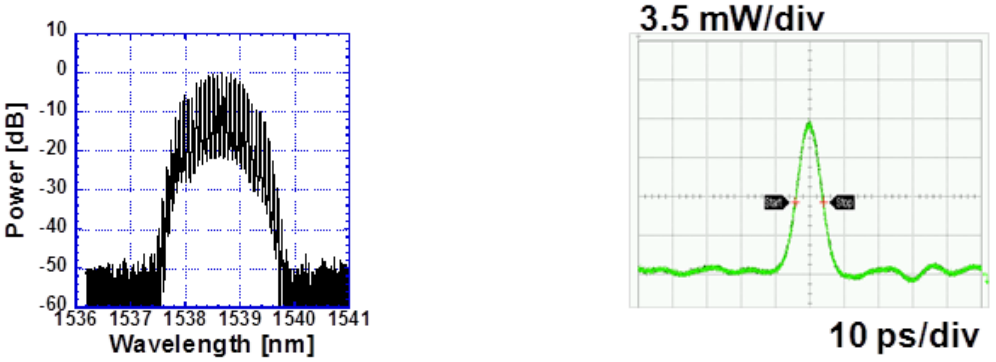

(a) Optical spectrum (b) Waveform

Figure 2.35: Optical spectrum and waveform before RZ-CW conversion

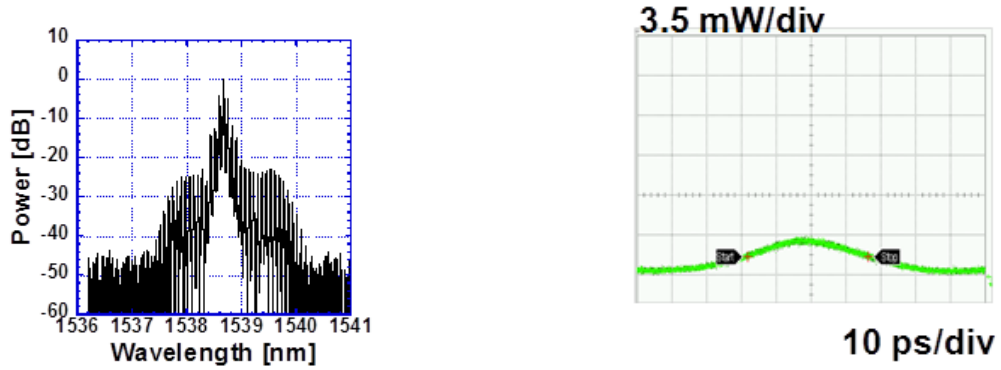

(a) Optical spectrum (b) Waveform

Figure 2.36: Optical spectrum and waveform after RZ-CW conversion

2.6 Frequency domain equalization (FDE)

As mentioned in section 2.4, waveform distortion caused by factors such as hardware imperfections can be done using a time-domain equalization (TDE) technique that uses a finite impulse response (FIR) filter. However, the main drawback to this form of compensation is that the frequency resolution of FIR filters is usually limited to 100 MHz because of the tap number limitations designed to avoid computational complexity. This limitation has made it impossible to achieve an error free performance under back-to-back condition for a 160 Gbaud, 64 QAM Gaussian pulse modulation-demodulation experiment as shown in Fig. 2.37.

In order to increase the QAM multiplicity from 32 to 64, there is a need to increase the resolution of equalization at the receiver, instead of the time

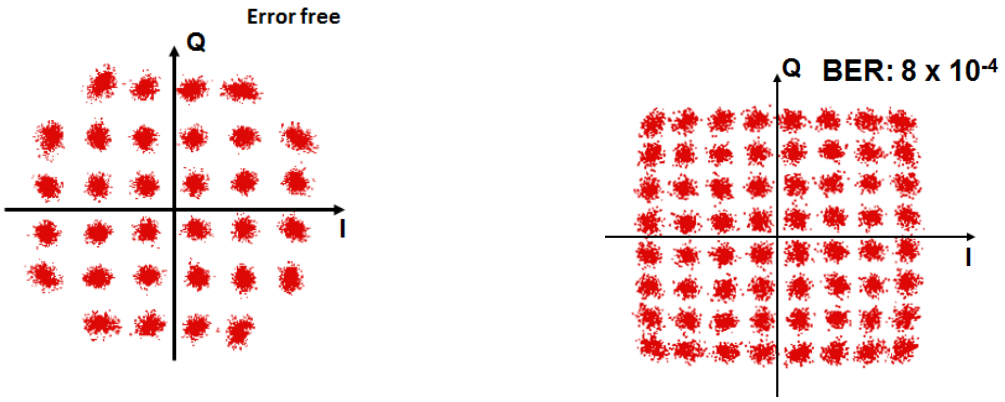

(a) 32 QAM (b) 64 QAM

Figure 2.37: Optical spectrum and waveform after RZ-CW conversion

domain based FIR filter equalization. This is done by devising a high resolution frequency domain equalization (FDE) to compensate for the static waveform distortion in the transmission system. This technique has a better equalization capacity, since with the FIR filter the equalization resolution is limited by the number of taps that can be used. This is because equalization resolution expressed as

$$\Delta f = \frac{Symbol\ rate}{N_{FIR}} \tag{2.51}$$

where N_{FIR} is the number of taps in the FIR filter. For our FIR equalization system, the number of taps is limited to 100, making the maximum attainable equalization resolution for a 10 Gbaud to be 100 MHz.

However, with FDE,since the equalization resolution is expressed as

$$\Delta f = \frac{sample\ rate}{N_{FFT}} \tag{2.52}$$

where N_{FFT} is the number of FFT steps involved, the resolution can be easily improved by taking advantage of the reduced computational complexity in FFT computations. For example, with an FFT size of 16384, the resolution is 2.44 MHz.

With the CW carrier the transciever distortion function $F_{distortion}(f)$ can be defined from by comparing the input ideal input signal $F_{in}(f)$ and the hardware distorted output signal $F_{out}(f)$ as shown in Fig. 2.38. The distortion function can be directly derived from the input and output signals as shown in the figure, but this is not the case with a pulse transmission system.

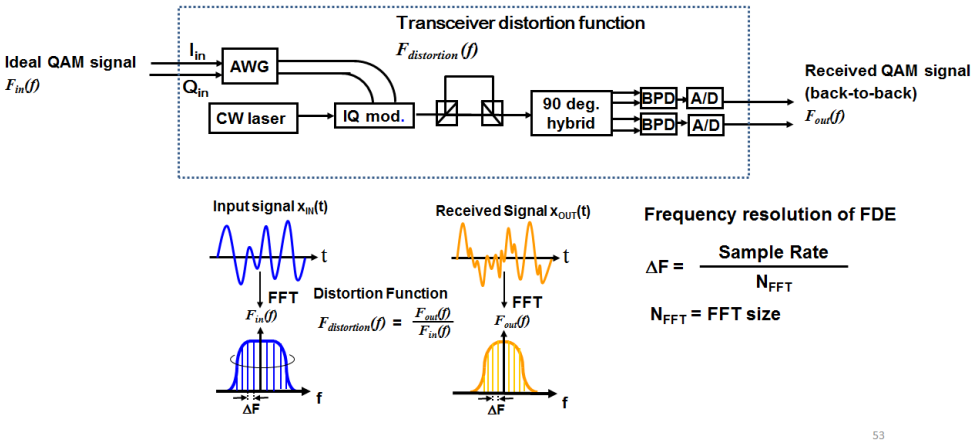

Figure 2.38: Frequency domain equalization for coherent optical transmission

2.7 Summary

In this chapter, the key devices and technologies used for coherent pulse transmission have been explained in detail. The section began with a general description of a fundamental configuration of coherent pulse transmission. Section 2.1 outlined the process of coherent pulse generation, where a frequency stabilized fiber laser was used in combination with a comb generator to give rise to a broad optical comb, from which a coherent pulse of desired shape is carved using a pulse shaper. After coherent pulse generation, the process of data modulation was elaborated in section 2.2. Data multiplexing, both in the time domain and polarization multiplexing was also discussed in the same section. The details on the dispersion managed fiber used was also discussed in subsection 2.2.4.

At the receiver, the signal was first polarization demultiplexed; this was discussed in subsection. After polarization demultiplexing, the signal was OTDM demultiplexed using a nonlinear loop mirror (NOLM), this process is explained in subsection 2.2.5.

Coherent pulse data is first homodyne detected before the data is demodulated using a vector spectrum analyzer software. The process of coherent detection was extensively discussed in section 2.2.6. Here OPLL circuit for the phase of CW-LO to be synchronized with a pulse plays an important role. Unlike conventional OPLL circuit, here a new scheme is developed where a comb is generated from CW-LO and the phase is compared between its harmonics and the pilot tone widely separated from the carrier frequency. The digital signal processing used for data demodulation was covered in section 2.4, where details in the equalization process is discussed.

In order to improve the SNR of the demodulated signal, an RZ-CW conversion circuit was proposed as means to improve the demodulation performance. Furthermore, in order to enhance waveform distortion compensation at the receiver, a high resolution frequency domain equalization (FDE) was proposed and described in detail.

Chapter 2 References

[1] K. Kasai, A. Suzuki, M. Yoshida, and M. Nakazawa, "Performance improvement of an acetylene (C_2H_2) frequency-stabilized fiber laser," *IEICE Electron. Express* 3(22), 487- 492 (2006).

[2] T. Sakamoto, T. Kawanishi, and M. Izutsu, "Asymptotic formalism for ultraflat optical frequency comb generation using a Mach-Zehnder modulator," *Opt. Lett.* 32(11), 1515- 1517 (2007).

[3] G. Baxter, S. Frisken, D. Abakoumov, H. Zhou, I. Clarke, A. Bartos, and S. Poole, "Highly programmable wavelength selective switch based on liquid crystal on silicon switching elements," in Proceedings of the *Optical Fiber Communication Conference (OFC)*,Anaheim, 2006, OTuF2.

[4] S. Shimotsu, S. Oikawa, T. Saitou, N. Mitsugi, K. Kubodera, T. Kawanishi, and M. Izutsu, "Single Side-Band Modulation Performance of a LiNbO3 Integrated Modulator Consisting of Four-Phase Modulator Waveguides," *IEEE Photon. Technol. Lett.*, 13(4), (2001).

[5] N. Doran and D. Wood, "Nonlinear-optical loop mirror", *Opt. Lett.*, 13(1), 56-58, (1988).

[6] G. Agrawal. "Nonlinear Fiber Optics", *5th Edition*, (2012).

[7] C. Boerner, V. Marembert, S. Ferber, C. Schubert, C. Schmidt-Langhorst, R. Ludwig, and H. G. Weber, "320 Gbit/s clock recovery with electro-optical PLL using a bidirectionally operated electroabsorption modulator as phase comparator," in Proceedings of the *Optical Fiber Communication Conference (OFC)*, Anaheim, 2005, OTuO3.

[8] M. Nakazawa et al. (eds), "High spectral density optical communication technologies: chapter 2, coherent optical communication."

[9] T. Okoshi, and K. Kikuchi, "Coherent optical fiber communications,"cha *Advances in Optoelectronics*, Chapter 2, KTK, Tokyo, 1988.

[10] C. Paré , A. Villeneuve, P.-A. Bé langer, and N. J. Doran, "Compensating for dispersion and the nonlinear Kerr effect without phase conjugation," *Opt. Lett.* 21(7), 459- 461, (1996).

[11] M. Nakazawa, K. Kasai, M. Yoshida, and T. Hirooka, "Novel RZ-CW conversion scheme for ultra multi-level, high-speed coherent OTDM transmission,"*Opt. Exp.* 19(26), $B574$- $B580$, (1996).

Chapter 3

1.92 Tbit/s, 64 QAM coherent Gaussian pulse transmission

In this chapter, I describe a digital coherent optical pulse transmission using a Gaussian pulse. Specifically, single carrier 1.92 Tbit/s transmission is demonstrated by OTDM multiplexing of 10 Gbaud, 64 QAM signals to 160 Gbaud. Coherent pulse transmission at such a high symbol rate and high multiplicity has not been demonstrated, because of the difficulty in generating a short pulse with sufficient phase coherence, SNR degradation due to insufficient receiver bandwidth compared to the data bandwidth, and compensating for distortions in such a broadband QAM signal. In order to solve these problems, I first developed a short coherent pulse generation using an ultra-broadband optical comb generator based on a dual-drive Mach-Zehnder modulator. Regarding the SNR degradation, I proposed a novel scheme of RZ-CW conversion at the receiver. In this scheme, the received RZ signal is converted to a data modulated on a CW carrier so that the data components can be confined within a narrow receiver bandwidth. In terms of waveform distortion compensation, I newly introduced a precise frequency domain equalization (FDE) technique which I proposed for coherent optical pulse transmission. This compensation technique enabled a more precise compensation of waveform distortion that arises from frequency dependent hardware imperfections when compared to time domain equalization (TDE), which employed an FIR filter. With these technologies, the 1.92 Tbit/s/ch transmission was achieved at a spectral efficiency of 3.8 bit/s/Hz.

3.1 Frequency domain Equalization for OTDM transmission

FDE has been applied to QAM transmission using a CW carrier but it has not been applied to coherent pulse transmission. This is because the transceiver distortion function required for FDE is not derived directly from the input and output signals in a pulse modulated system. In order to obtain the distortion function, the ideal signal has to have the same spectral extent as the received distorted signal. This is done in a process explained in Fig. 3.1. Here, I describe the process I used in FDE for the the pulse transmission system employing RZ-CW conversion technique, and how it is used for waveform distortion compensation. As shown in Figure 3.1, first, a training signal $x_{in}(t)$ is sent through a back-to-back system. The output from the digital sampling oscilloscope $x_{out}(t)$ is then converted to the frequency domain $X_{out}(f)$. In order to account for spectral changes on the baseband signal due to processes such as modulation on the RZ-carrier and the eventual RZ-CW conversion, in which the training signal is numerically loaded on an RZ-carrier and then RZ-CW converted, this signal is then passed through a low pass filter to mimic the frequency limitation posed by the receiver bandwidth by devices such as A/D converters. The filtered signal $x'_{in}(t)$ is thereafter converted to the frequency domain by FFT, with the signal $X'_{in}(f)$ then compared with that of the distorted output signal $X_{out}(f)$, giving the transceiver distortion function as:

$$F_{distortion}(f) = \frac{X_{out}(f)}{X'_{in}(f)} \tag{3.1}$$

This distortion function is used to compensate for the waveform distortion on any data signal that passes through the hardware in the system, by dividing the data signal with the distortion function $F_{distortion}(f)$.

The advantage of this FDE process over TDE in terms of decreased complexity can be derived from the number of real-valued multiplications in FDE as opposed to that when using an FIR filter. The number of real-valued multiplications with FDE n_{FDE} if given by $n_{FDE} = 8\log_2(N_{FFT})$, where N_{FFT} is the FFT size of the training signal used during equalization. Meanwhile with TDE, the numerical complexity expressed as the number of real-valued multiplications n_{FIR} is given by $n_{FIR} = 4N_{FIR}$, where N_{FIR} is the number of FIR taps used. These two metrics n_{FFT} and n_{FIR} plotted as a function of the equalization resolution is shown in Fig. 3.2.

As it can be seen from Fig. 3.2, in order to decrease the resolution of equalization to about 1 MHz, the computational complexity of the TDE process has to be increased to a value 10^3 times that required with FDE.

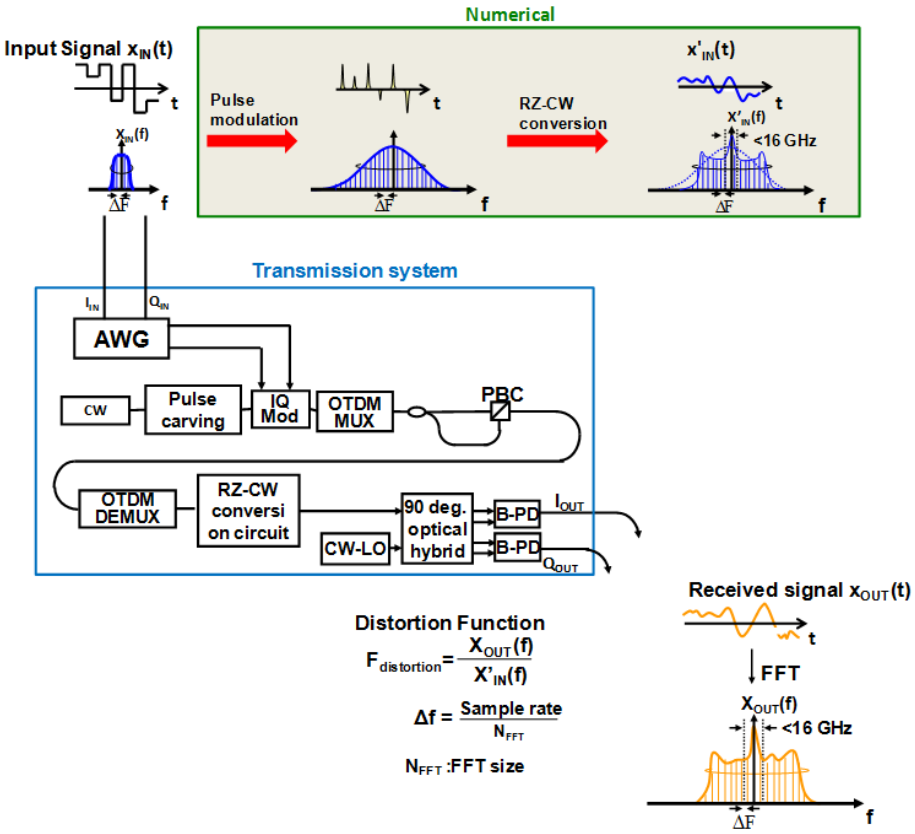

Figure 3.1: Frequency domain equalization for coherent optical transmission

The training signal I used was a fixed pattern 64 QAM signal. The constellation of this ideal fixed patern 64 QAM signal is shown in Fig. 3.3. This ideal training signal is first used to modulate an RZ signal before RZ-CW converted to a CW-like signal numerically. The signal is then given a bandwidth limitation to mimic the receiver bandwidth limitation. The constellation map of the bandwidth limited training signal is shown in Fig.3.4(a). As it can be seen the training signal is greatly distorted by the bandwidth limitation process. This distortion is compensated for using a 99 tap FIR filter leading to the signal shown in constellation map shown in Fig. 3.4(b). This signal is what is used for the FDE equalization process.

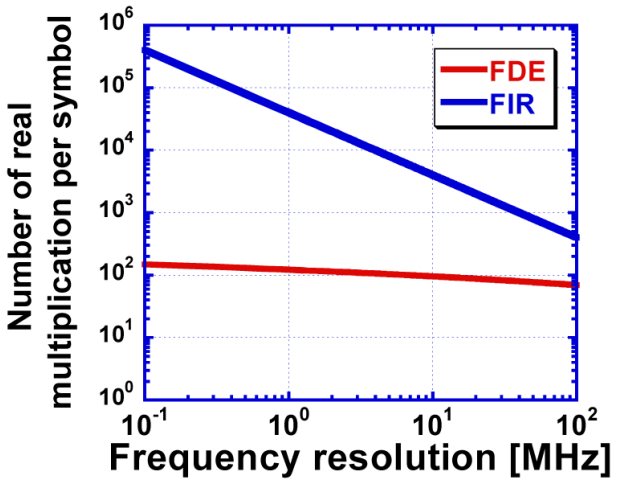

Figure 3.2: Numerical complexity of both FDE and TDE expressed as a function of resolution of equalization.

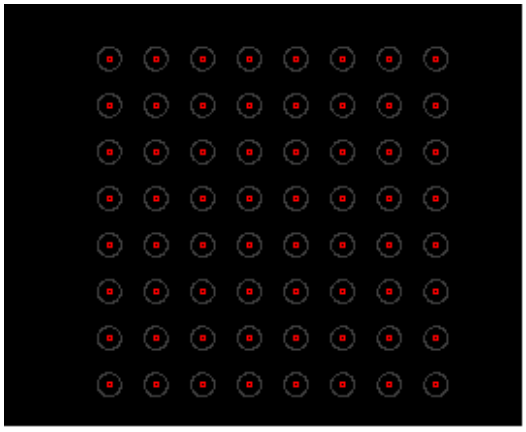

Figure 3.3: The ideal training 64 QAM signal.

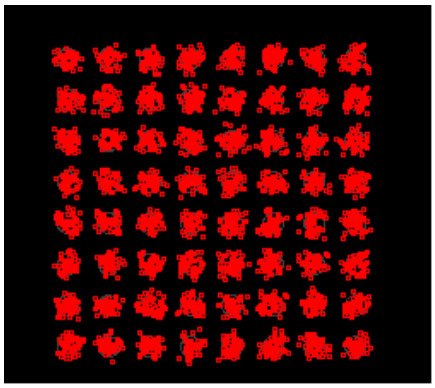

(a) After bandwidth limitation

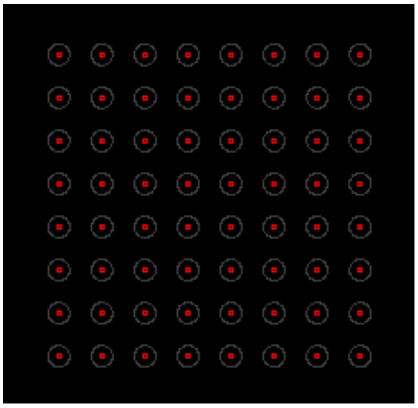

(b) After equalization

Figure 3.4: Training signal generation

3.2 Experimental setup

Figure 3.5 shows the experimental setup used for the 1.92 Tbit/s, 64 QAM coherent pulse transmission using Gaussian pulses. First, a 10 GHz coherent Gaussian pulse is generated using a coherent pulse generator described in 2.1. After QAM modulation, where the QAM modulator was driven by an arbitrary waveform generator, the modulated data signal is OTDM and polarization multiplexed using a PLC-type multiplexer and polarization beam combiner, respectively. The data was further combined with a pilot tone signal, which was used for phase synchronization at the receiver. After traversing a 150 km dispersion managed fiber link, the signal went through a demultiplexing process; first polarization demultiplexing using a polarizing beam splitter and lastly OTDM demultiplexing using NOLM. After RZ-CW conversion, the demultiplexed data signal was fed into a coherent detection circuit consisting of a 90^o optical hybrid and two sets of balanced photodetectors (BPDs). Here, the phase of the CW-LO is synchronized to the transmitted data through a pilot tone using an OPLL circuit described in section 2.3. The detected signal was then digitized using a 40 Gsample/s digital oscilloscope, after which it was demodulated in offline condition using the VSA software. Waveform distortion compensation was carried out using frequency domain equalization to compensate for distortions arising from hardware imperfections.

As mentioned in chapter 2, in the pulse generation circuit, an acetylene frequency-stabilized fiber laser oscillating at 1538.8 nm with a 4 kHz linewidth was used [3]. The CW optical output from the laser was amplified to 10 dBm and fed into a comb generator [4], which consisted of a dual-drive $LiNbO_3$ (LN) Mach-Zehnder modulator (MZM) of V_π of 2.2 V. The RF signal from a synthesizer placed at the transmitter was used to drive the comb generator at a frequency of 9.95328 GHz and RF power of -7.2 dBm. The optical spectrum of the comb produced is shown in Fig. 3.6. The harmonics on the comb are precisely separated by the RF modulation frequency and the spectral bandwidth and the -10 dB bandwidth being 490 GHz.

After passing the broad comb through a pulse shaper the waveform and spectrum obtained are shown in Figs.3.7(a) and 3.7(b), respectively. The pulse width was 2.4 ps, while the spectral bandwidth was 1.5 nm. This corresponds to the time bandwidth product of 0.45, close to the 0.44 transform-limit condition of the Gaussian pulse. As it can be seen from Fig. 3.7(a), the generated spectrum accurately fitted the Gaussian profile.

Pulse train generation is then followed by data modulation using an IQ modulator, where the amplitude and phase of the pulse train were modulated. The IQ modulator was driven by an arbitrary waveform generator (AWG)

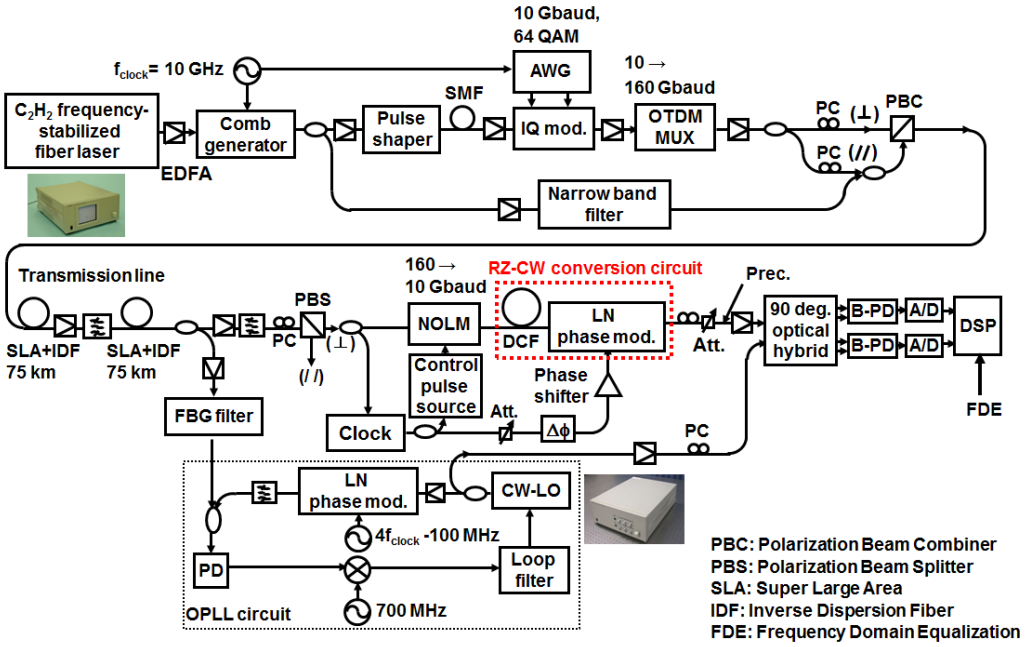

Figure 3.5: The experimental setup for 1.92 Tbit/s, 64 QAM coherent pulse transmission using Gaussian pulses

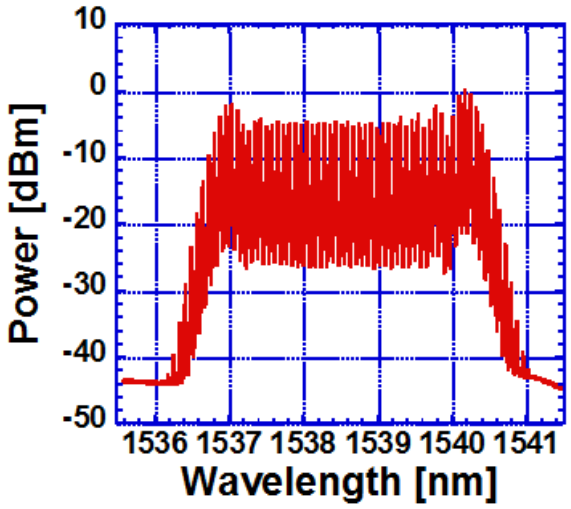

Figure 3.6: The optical comb spectrum of the comb generator output

whose timing and rate was synchronized to that of the Gaussian pulse train coming out of the coherent pulse generation circuit. Here, the AWG sampling rate was 10 Gsample/s, the data resolution was 10 bits and the data length was set at 4096 symbols. The 10 Gbaud, 64 QAM pulse data train was

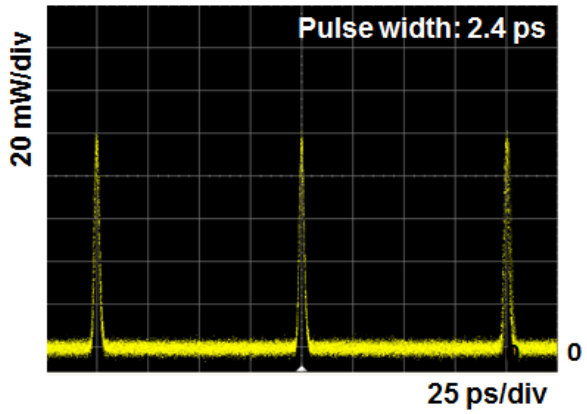

(a) Waveform

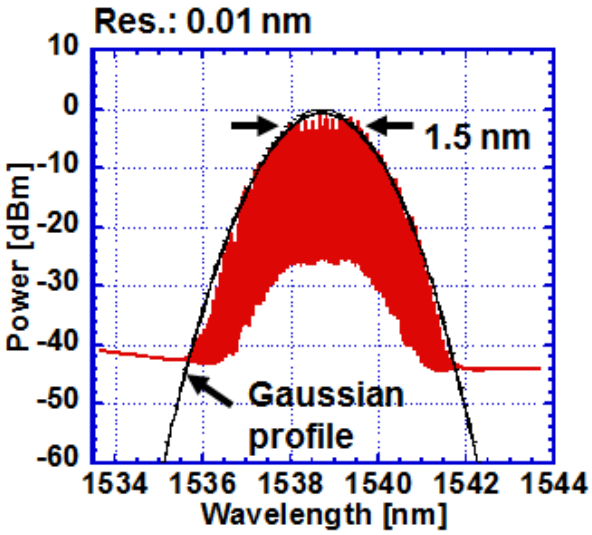

(b) Optical spectrum

Figure 3.7: Optical waveform and spectrum of the generated Gaussian pulse

fed into a PLC-type multiplexer, where the baud rate was increased to 160 Gbaud. The OTDM signal out of the multiplexer was divided into two arms by the use of a 50 : 50 optical couplers, where polarization controllers (PCs) placed on both arms were used to orient the polarizations of the two branches such that they are mutually orthogonal to one another. They were then combined using a polarization beam combiner. Simultaneously, in order to carry out phase synchronization of the CW-local oscillator used for homodyne detection at the receiver, a non modulated tone was generated by extracting the 28th harmonic from the center frequency by using a very narrow grating

filter. The generated tone is shown in Fig. 3.8. This pilot tone signal was then combined with the polarization multiplexed 1.92 Tbit/s, 64 QAM pulse data signal at power ratio of 4 dBm (data):−12 dBm (pilot tone) using an optical coupler. The resultant waveform and spectrum are shown in Figs.

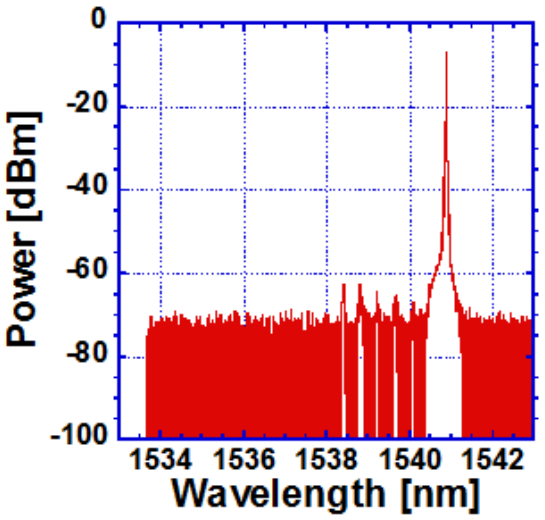

Figure 3.8: Pilot tone generation

3.9(a) and 3.9(b), respectively.

The transmission fiber link was a dispersion managed fiber, where each span was composed of 50 km SLA and 25 km IDF of dispersion 19.5 ps/nm/km and -40 ps/nm/km, respectively. The average loss per span was 18 dB/span, which was compensated for by EDFAs.

The configuration of the OTDM demultiplexing circuit is shown in Fig. 3.10. The polarization multiplexed data signal at the receiver was first polarization demultiplexed and the signal divided by an 80 : 20 coupler. The 20% of the OTDM data signal was fed into a clock recovery unit [7] for clock regeneration. This clock signal was used to drive a comb generator placed the receiver to generate a control pulse used for OTDM demultiplexing. This comb was similar to that used at the transmitter. The CW-optical source used for the comb generation process was a tunable DFB laser diode oscillating at 1565 nm. The CW optical output from the DFB LD was fed into the comb generator at a power of 10 dBm. The broad comb generated at the receiver was fed into a dielectric filter from which a pulse train, used as a control pulse for the NOLM process, was carved out. SMF of length 300 m was used to compensate for the chirp induced by the comb generator. The optical spectrum and waveform of the control pulse generated is shown in

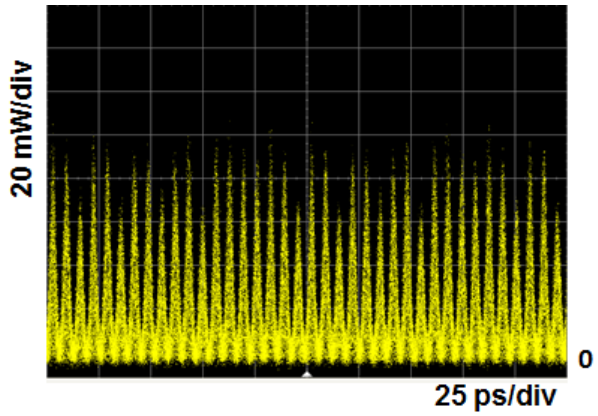

(a) Time waveform

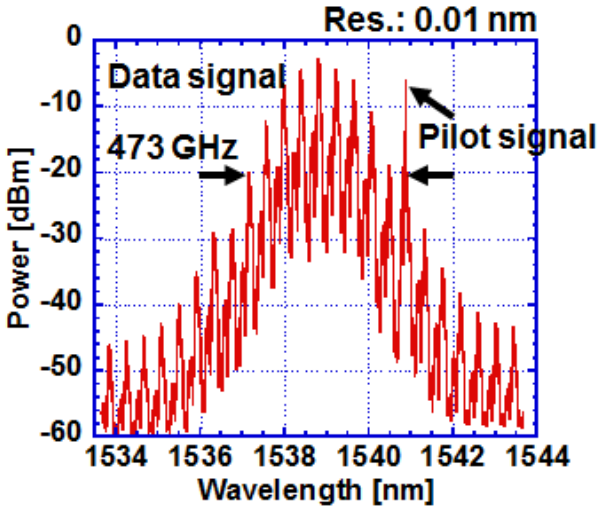

(b) Optical spectrum

Figure 3.9: 1.92 Tbit/s, 64 QAM Gaussian pulse data signal

figure Fig. 3.11. The pulse width was 5.2 ps. This is much broader than the 2.4 ps of the pulse generated at the transmitter for data transmission but sufficient for the demultiplexing operation.

A NOLM with a highly nonlinear fiber (HNLF) of length 100 m, dispersion slope 0.029 ps/nm^2 and nonlinear coefficient γ of 20.4 $W^{-1}km^{-1}$ was used. The zero dispersion wavelength the HNLF was 1522 nm. The polarization demultiplexed data signal was fed into the NOLM at a power of 7 dBm, and the control pulse at 23 dBm. The demultiplexed 10 Gbaud, 64 QAM data signal is shown in Fig. 3.12. The demultiplexed data signal was then

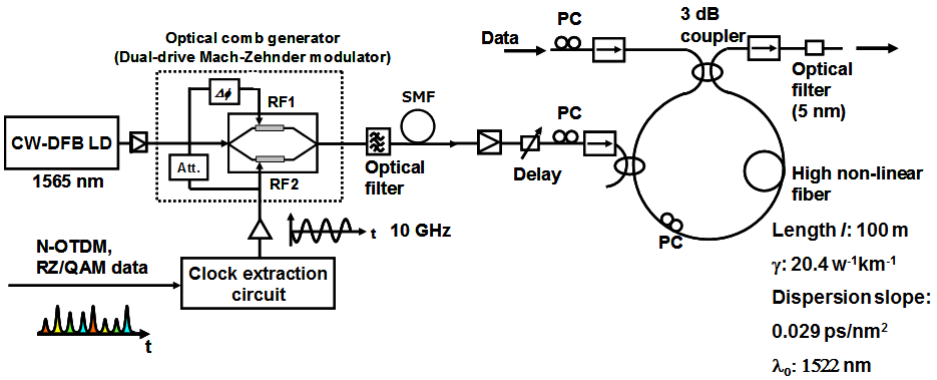

Figure 3.10: OTDM demultiplexing using NOLM

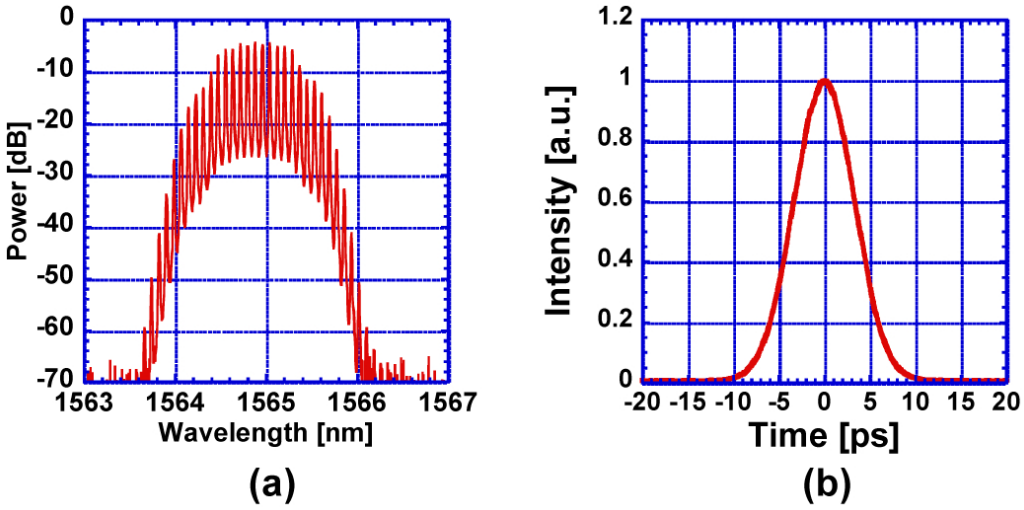

Figure 3.11: Optical spectrum (a) and waveform (b) of the control pulse

fed into an RZ-CW conversion circuit. The results on RZ-CW conversion are described in subsection 3.2.1.

3.2.1 The RZ-CW conversion characteristics

As mentioned in chapter 2, an RZ-CW conversion circuit consisted of a dispersive medium and a phase modulator. I carried out an optimization experiment and obtained an dispersion value of -69 ps/nm using a dispersion compensating fiber (DCF). At dispersion values greater than -69 ps/nm, there was excessive pulse broadening resulting in interference between adjacent symbol points. With smaller values of dispersion, there was insufficient

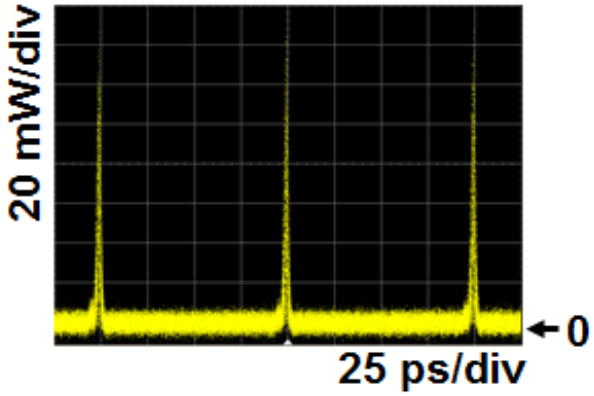

Figure 3.12: The demultiplexed 10 Gbaud, 64 QAM pulse data signal

pulse broadening leading to less increase in peak power at the center frequency. The phase modulator was driven at a modulation depth of 2.5π. First, the demultiplexed 10 Gbaud data signal is passed through the -69 ps/nm DCF. The dispersed signal was chirped and in order to cancel the chirp, part of the clock generated at the clock recovery unit is amplified and used to modulate the dispersed signal at the 2.5π modulation depth. The spectra of the data signal before and after RZ-CW conversion is shown in Fig. 3.13. As a result of RZ-CW conversion, there was an increase of about 6 dB in the peak power. The constellation maps in Fig. 3.14 show the demodulation performance without RZ-CW conversion and that when RZ-CW conversion was used. As shown in Fig. 3.14(a), the demodulation was not possible but with the introduction of RZ-CW conversion, it was possible to carry out demodulation as shown in Fig. 3.14(b). This was due to increase in SNR of the demodulated signal that resulted from RZ-CW conversion.

3.2.2 The OPLL process and performance

The 28th harmonic of the optical comb generated at the transmitter was extracted and made the pilot tone signal. At the receiver, the pilot tone signal was extracted from the data signal using an FBG filter. This pilot tone signal was used for phase synchronization of the CW-LO oscillator by first generating a local comb. This is done by feeding the CW light into phase modulator. This phase modulator was driven by a signal of frequency $4f_{clock} - 100$ MHz, and its 7th harmonic was 700 MHz above the pilot tone frequency. By keeping this difference constant through a feedback of the voltage error via a PLL circuit to the CW-LO, the phase of the CW-LO is

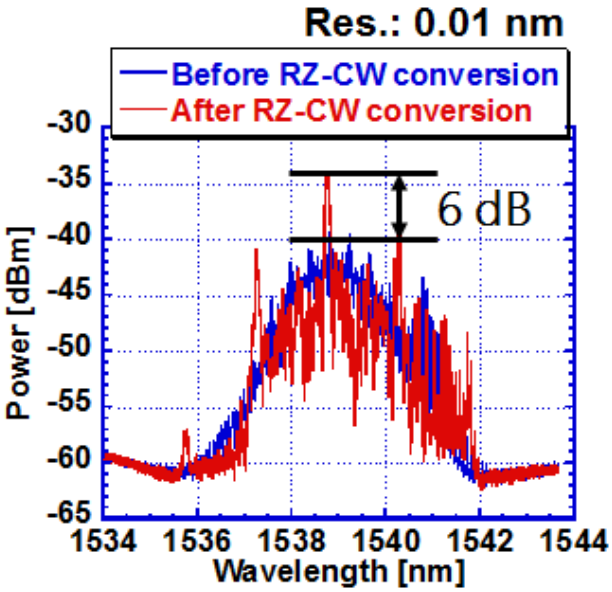

Figure 3.13: Optical spectra before and after RZ-CW conversion

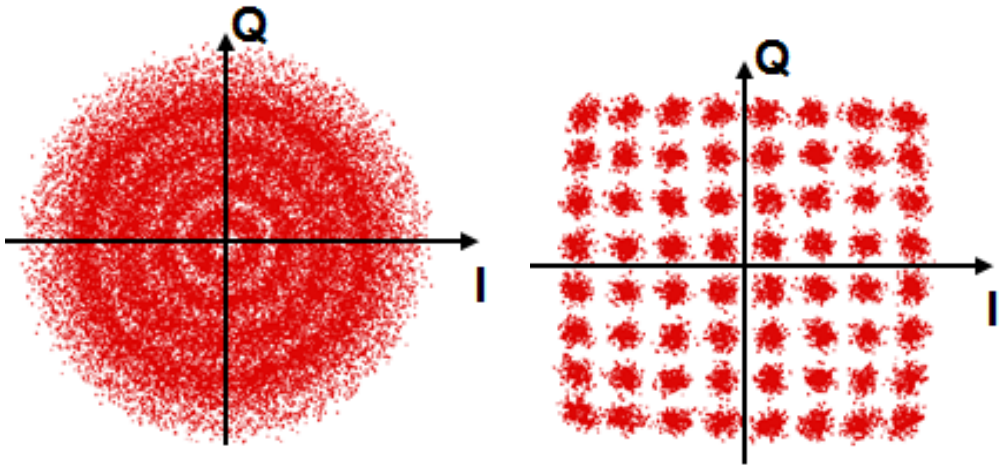

(a) Without RZ-CW conversion (b) With RZ-CW conversion

Figure 3.14: Optical spectrum and waveform before RZ-CW conversion

locked to the phase of the data signal. The IF spectrum of the beat signal between the pilot signal and the 7th harmonic is shown in Fig. 3.15. The CW-LO used was a fiber ring laser with a linewidth of as narrow as 4 kHz.

As shown by the IF spectrum in Fig. 3.15(a), the linewidth was narrower than 10 Hz, which is the resolution limit, and the phase noise integrated from

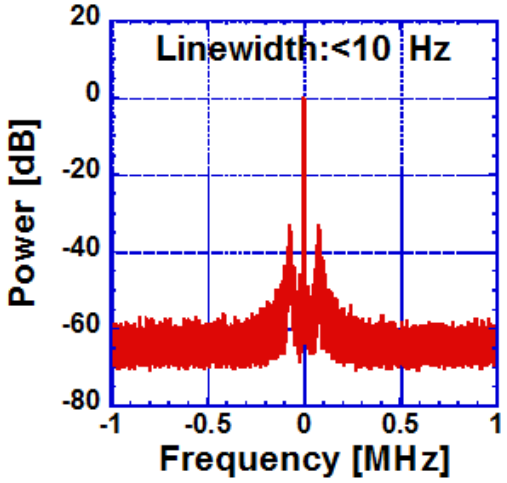

(a) The IF spectrum

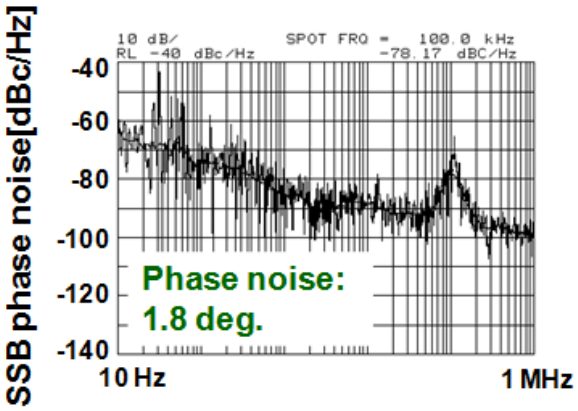

(b) The SSB IF spectrum

Figure 3.15: The IF spectra of the beat signal between the pilot signal and 7th harmonic of the local comb

10 Hz $\sim$ 10 MHz was 1.8 deg. This value is three times smaller than the phase allowance[1] of the 64 QAM constellation map as shown in 3.16. Therefore, the OPLL was sufficient for the demodulation of a 64 QAM signal.

[1]phase allowance: the phase difference between two closest points on the constellation map

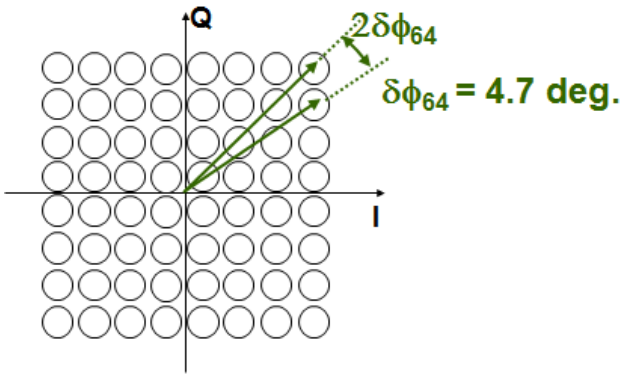

Figure 3.16: The ideal 64 QAM constellation map

3.3 Experimental results

After homodyne detection, the signal was digitized using a 16 GHz, 40 Gsample/s oscilloscope. The digital data was demodulated using VSA software and the error counted in an offline condition for 245760 bits of data. First, demodulation was performed with and without Frequency domain equalization. Figure 3.17 shows constellation maps with and without FDE. With the use of FDE, there was an improvement in the EVM value from 4.4%, to 3.6%. This was as a result of the precise waveform distortion compensation by FDE of the hardware imperfections in devices such as IQ-modulator.

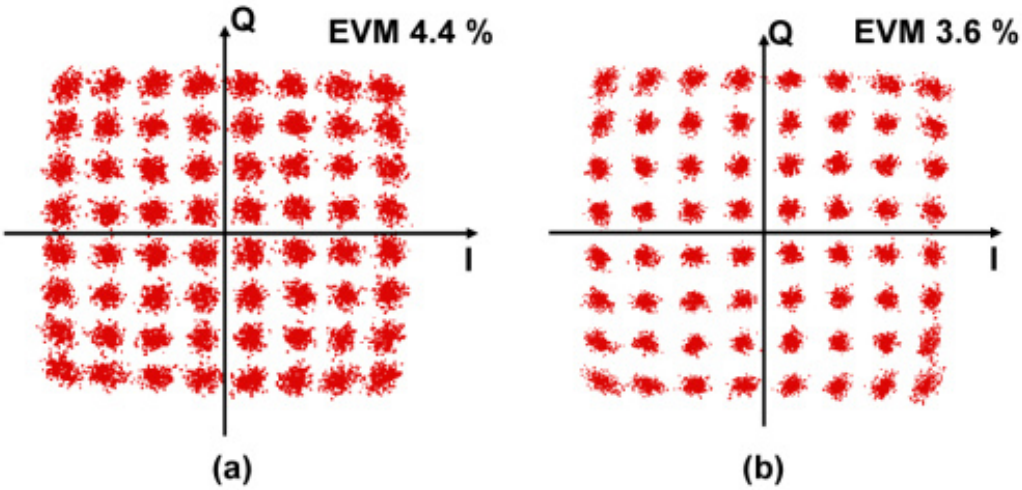

Figure 3.17: Constellation maps, (a) without FDE and (b) with FDE

Next, the signal power into the transmission fiber was optimized with the aim of maintaining a high OSNR after transmission, while suppressing the nonlinear phase rotation that takes place in the fiber. The launch power of the signal into the fiber was varied while the demodulation performance was estimated. Fig. 3.18 shows the BER as a function of launch power. At lower values of launch power, due to diminished OSNR after transmission, the demodulation performance decreased. While with launch powers greater than 4 dBm, the BER increases due to the increased fiber nonlinearity at high powers. The 1.92 Tbit/s, 64 QAM pulse data signal was then transmitted at 4 dBm. It is worth nothing that self phase modulation (SPM) pre-compensated at the AWG in the transmitter, where the QAM data was given a phase rotation prior to transmission.

The OSNR of the data signal, before and after transmission was measured as shown in Figs. 3.19(a) and 3.19(b), respectively. There was an OSNR degradation of 9 dB that occurred during transmission. The BER perfor-

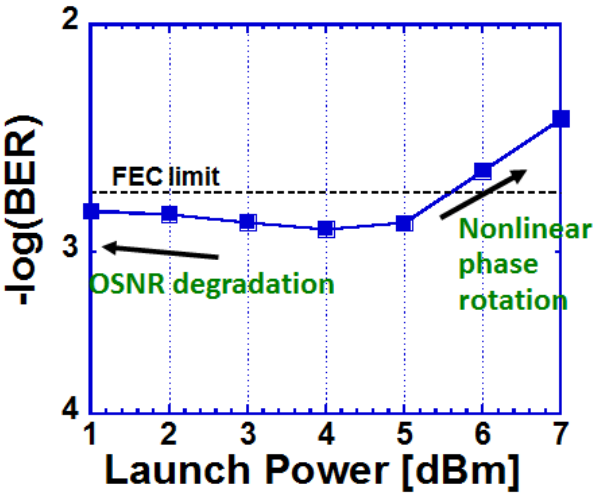

Figure 3.18: Launch power optimization

mance was evaluated. In Fig. 3.20(a), the red plot is the BER performance under back-to-back condition. The plot in blue is the performance after 150 km of transmission. The power penalty between the back-to-back and 150 km transmission at a BER of 2×10^{-3} was 5 dB. There was an error floor on the BER after 150 km of transmission. This is attributable to the cross phase modulation (XPM) between two polarizations during transmission.

The corresponding BER for all the 16 tributaries is shown in Fig. 3.20b. A BER of below FEC limit was obtained for all the tributaries.

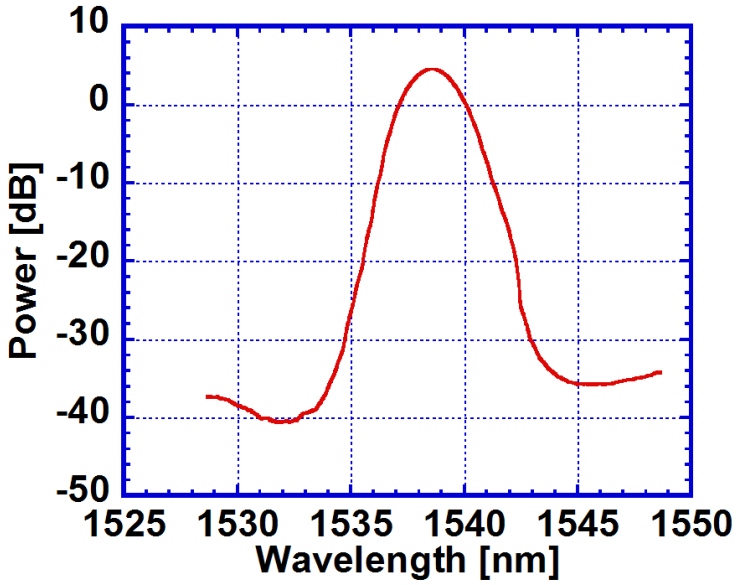

(a) Back-to-back (OSNR 50 dB at 2 nm Res.)

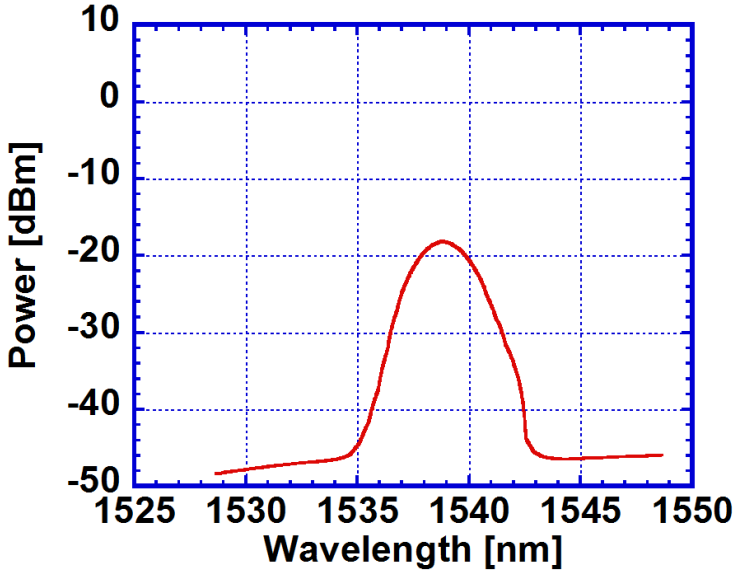

(b) After 150 km (OSNR 41 dB at 2 nm Res.)

Figure 3.19: Optical spectra, before and after 150 km transmission measured at 2 nm Res.

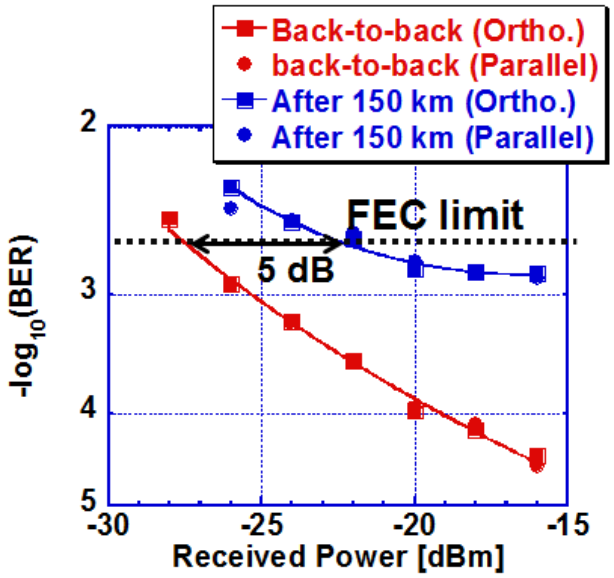

(a) BER for a single tributary as a function of the received power

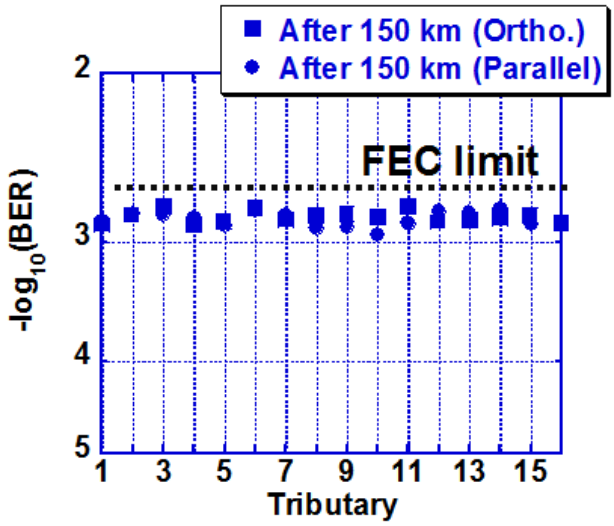

(b) The BER for all the 16 tributaries

Figure 3.20: The bit error rate (BER) characteristics

3.4 Discussion and conclusion

This chapter presented the first demonstraton of 1.92 Tbit/s/ch coherent pulse transmission using a Gaussian pulse. Section 3.2 described coherent pulse generation from a CW optical source. Here, a 10 GHz, 2.4 ps coherent Gaussian pulse was successfully generated by using a broadband optical comb generator comprising a dual-drive Mach-Zehnder modulator. The low V_π of the modulator played a very important role to expand the bandwidth. The following section described data modulation and multiplexing. Transmission and launch power optimization is described in the following section. The last two sections covered aspects on polarization and OTDM demultiplexing. Thereafter, the signal was RZ-CW converted before homodyne detection. As a result of the RZ-CW conversion, the SNR of the demultiplexed signal was improved by as much as 6 dB. This led to successful demodulation of the 64 QAM signal. The demodulation was carried out in an offline condition were the bit error was counted.

By combining these technologies, the spectral efficiency achieved for the 1.92 Tbit/s, 64 QAM Gaussian pulse signal transmitted within the approximately 473 GHz was:

$$\begin{aligned} SE &= \frac{1.92\ Tbit/s}{(473\ GHz\ \times 1.07(7\%\ FEC))} \\ &\approx 3.8\ bit/s/Hz \end{aligned} \tag{3.2}$$

This spectral efficiency is still low compared to other 64 QAM transmission experiments employing a CW carrier [7]- [9].There is a need for a new transmission format so as to improve the spectral efficiency further, which is the main subject of the following chapters.

Chapter 3 References

[1] M. Nakazawa, K. Kasai, M. Yoshida, and T. Hirooka, "Novel RZ-CW conversion scheme for ultra multi-level, high-speed coherent OTDM transmission,"*Opt. Exp.* 19(26), *B*574- *B*580, (1996).

[2] D. O. Otuya, K. Kasai, M. Yoshida, T. Hirooka, and M. Nakazawa, "A single-channel, 64 QAM coherent optical pulse transmission over 150 km using frequency-domain equalization (FDE)," *Opt. Exp.,* 21(19), 22808-22816 (2013).

[3] K. Kasai, A. Suzuki, M. Yoshida, and M. Nakazawa, "Performance improvement of an acetylene (C_2H_2) frequency-stabilized fiber laser," *IEICE Electron. Express* 3(22), 487- 492 (2006).

[4] T. Sakamoto, T. Kawanishi, and M. Izutsu, "Asymptotic formalism for ultraflat optical frequency comb generation using a Mach-Zehnder modulator," *Opt. Lett.* 32(11), 1515- 1517 (2007).

[5] G. Baxter, S. Frisken, D. Abakoumov, H. Zhou, I. Clarke, A. Bartos, and S. Poole, "Highly programmable wavelength selective switch based on liquid crystal on silicon switching elements," in Proceedings of the *Optical Fiber Communication Conference (OFC)*,Anaheim, 2006, OTuF2.

[6] C. Boerner, V. Marembert, S. Ferber, C. Schubert, C. Schmidt-Langhorst, R. Ludwig, and H. G. Weber, "320 Gbit/s clock recovery with electro-optical PLL using a bidirectionally operated electroabsorption modulator as phase comparator," in Proceedings of the *Optical Fiber Communication Conference (OFC)*, Anaheim, 2005, OTuO3.

[7] H. Goto, M. Yoshida, T. Omiya, K. Kasai, and M. Nakazawa, "Polarization and frequency division multiplexed 1 Gsymbol/s, 64 QAM coherent optical transmission with 8.6 bit/s/Hz spectral efficiency over 160 km," *IEICE Electron. Exp.*. 5(18), 776- 781, (2005).

[8] X. Zhou, L. E. Nelson, P. Magill, R. Isaac, B. Zhu, D. W. Peckham, P. I. Borel, and K. Carlson,"High Spectral Efficiency 400 Gb/s Transmission Using PDM Time-Domain Hybrid 32- 64 QAM and Training-Assisted Carrier Recovery," *J. Lightwave Technol.*, 31(7), 999- 1005, (2013).

[9] R. Maher, D. Lavery, D. Millar, A. Alvarado, K. Parsons, R. Killey, and P. Bayvel, "Reach Enhancement of 100% for a DP-64QAM Super-Channel using MC-DBP," *in proceedings of Optical Fiber Communication Conference (OFC).* Th4D.5, (2015).

Chapter 4

1.92 Tbit/s, 64 QAM coherent Nyquist pulse transmission

In order to increase the spectral efficiency further, I proposed the utilization of a Nyquist pulse for digital coherent optical pulse transmission. Optical Nyquist pulse enables us to transmit data with a much broader pulse width and narrower spectral width compared to Gaussian pulse without affected by intersymbol interefence (ISI). So far, a Nyquist pulse has been applied to non-coherent transmission such as DPSK (Differential Phase Shift Keying) or DQPSK (Differential Quadrature Phase Shift Keying) and its advantage has been demonstrated such as increased tolerance to chromatic dispersion and polarization-mode dispersion. However, the Nyquist pulse has not been applied to coherent transmission yet. If Nyquist pulse is used for coherent QAM transmission, it will bring us enormous advantages in terms of high spectral efficiency in an ultrahigh-speed transmission. With a coherent Nyquist pulse, I demonstrated a 1.92 Tbit/s, 64 QAM transmission experiment within a bandwidth of 240 GHz. I was therefore able to increase the spectral efficiency of coherent optical pulse transmission from 3.8 bit/s/Hz with a Gaussian pulse[1] to 7.5 bit/s/Hz. In this chapter, I describe the generation of a coherent Nyquist pulse train, and the 1.92 Tbit/s, 64 QAM coherent Nyquist pulse data transmission over 150 km. A special focus is made on a coherent Nyquist pulse generation where a pulse shaper for precise spectral manipulation is newly added in the transmitter, and an ultrafast optical sampling circuit comprising NOLM (Nonlinear Optical Loop Mirror) so that only a portion of the signal at each symbol interval can be extracted without affected by ISI.

[1] Chapter 3, conclusion

4.1 Principle of Nyquist pulse TDM transmission

A Nyquist pulse is a pulse with a sinc-like waveform [7], that has an oscillating head and tail that cross zero at periodic intervals. The pulse waveform and spectral distribution of a Nyquist pulse is shown by the equations

$$r(t) = \frac{\sin(\frac{\pi t}{T})}{\frac{\pi t}{T}} \frac{\cos(\frac{\alpha \pi t}{T})}{1 - \left(2\frac{\alpha t}{T}\right)^2} \tag{4.1}$$

$$R(f) = \begin{cases} 1, & 0 \leq |f| \leq \frac{1-\alpha}{2T} \\ \frac{1}{2}\left\{1 - \sin\left(\frac{\pi}{2\alpha}(2T|f| - 1)\right)\right\}, & \frac{1-\alpha}{2T} \leq |f| \leq \frac{1+\alpha}{2T} \\ 0, & |f| \geq \frac{1+\alpha}{2T} \end{cases}$$

where T is the symbol period, and α is the roll-off factor which exists in the range $0 \leq \alpha \leq 1$. Figure 4.1(a) shows the time waveform for Nyquist pulses with the roll-off factors $\alpha = 0$, 0.5 and 1. The corresponding spectrum is shown in Fig. 4.1(b). $r(t)$ and $R(f)$ are generally known as an impulse response and transfer function of a Nyquist filter [7], which is used in wireless communication.

As shown in Fig. 4.1(a), when the roll-off factor $\alpha = 0$, the oscillation of the sidelobes is more prominent and persists for longer durations. As the value of the roll-off factor increases, the magnitude of the oscillation of the tail dampens and quickly dissipates. The zero crossing points of the oscillating tail is independent of the roll-factor. Figure 4.1(b) shows the spectra of the Nyquist pulses for the different roll-off factors. At the roll-off factor $\alpha = 0$, the spectrum is rectangular with spectral bandwidth being $1/T$. As the roll-off factor increases the spectral bandwidth increases in proportion given by the equation

$$B_\alpha = (1 + \alpha)\frac{1}{T} \tag{4.2}$$

Therefore, in order to increase the spectral efficiency, a Nyquist pulse of a lower roll-off factor is desirable.

Since the zero-crossing interval is periodic and independent of the roll-off factor, Nyquist pulses can be bit-interleaved to a higher symbol rate $1/T$ in which the intersymbol interference (ISI)-free points are maintained despite strong overlap with neighboring pulses, as shown in Fig. 4.2.

Comparing the Nyquist pulse for 160 Gbaud with a Gaussian pulse required for the same performance, a graph shown in Fig. 4.3 is obtained. As shown in Fig. 4.3, the 40% duty cycle Gaussian pulse required for the 160

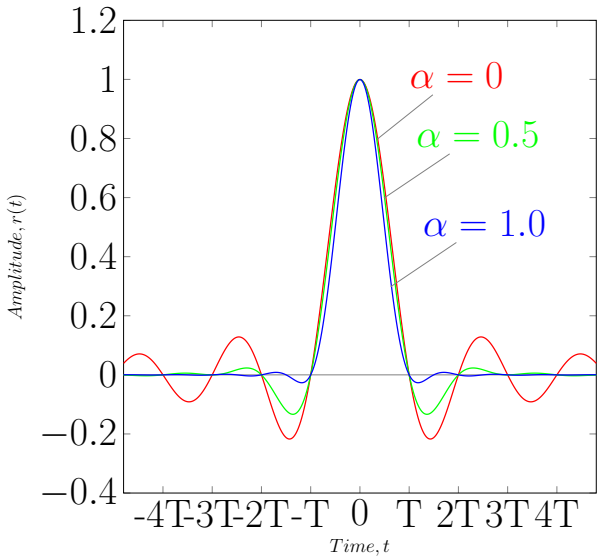

(a) Waveform

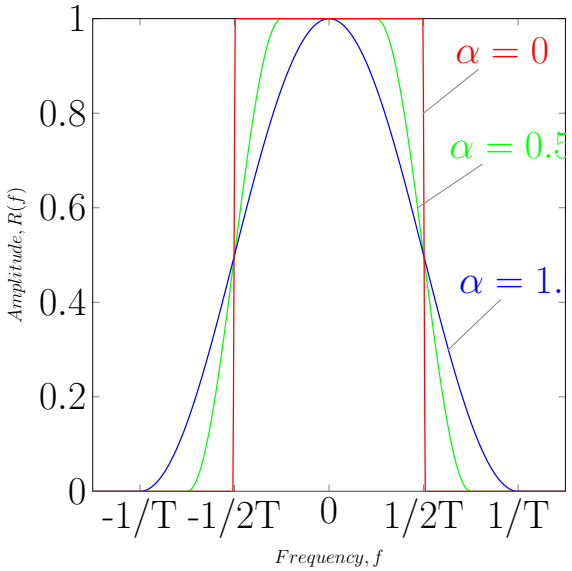

(b) Spectrum

Figure 4.1: Nyquist waveform and spectrum

Gbaud transmission experiment would have a pulse width of 2.4 ps. This is much shorter than 5.2 ps of the Nyquist pulse. The spectral bandwidths shown in Fig. 4.3(b) show that a Gaussian pulse signal would require close to twice the bandwidth of 473 GHz, compared to 240 GHz for a Nyquist pulse data. This indicates a possibility of doubling the spectral efficiency

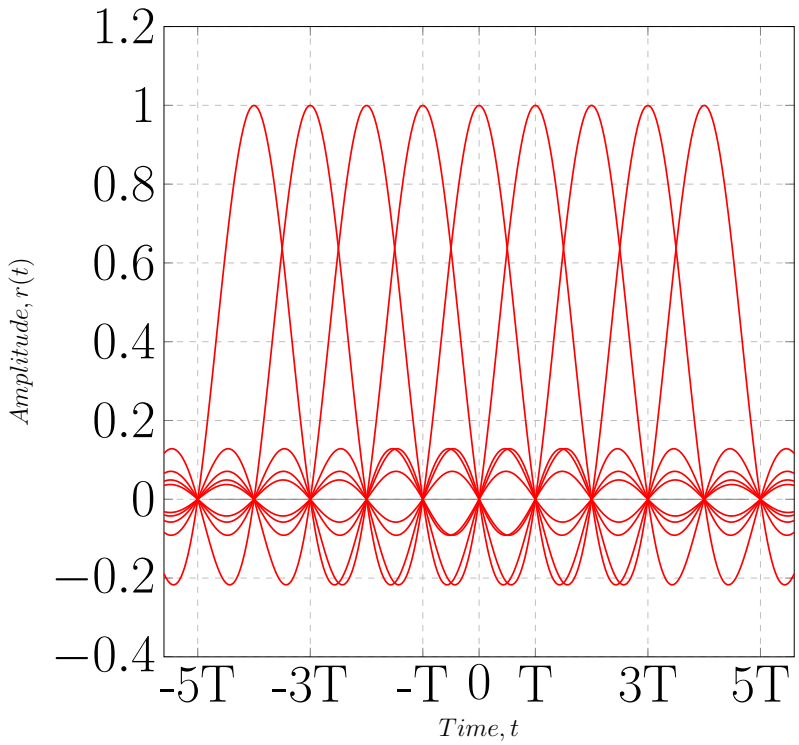

Figure 4.2: The multiplexed Nyquist pulse

with Nyquist pulse compared to the Gaussian pulse transmission.

The fundamental configuration for a transmission experiment that uses Nyquist pulses is shown in Fig. 4.4. First, a broad optical comb is generated from a combination of CW laser and a comb generator. This comb is subsequently passed through a pulse shaper, thus generating a Nyquist pulse train. Here, the waveform and spectral profile of Nyquist pulses are given by equation (4.1). After the Nyquist pulse is generated, the optical signal is QAM modulated at a baud rate of f_s. The modulated signal is then multiplexed to a baud rate of Nf_s with a bit interleaver by aligning the zero-crossing points of adjacent tributaries, which can be achieved by setting the symbol period T of the optical Nyquist pulses at $T = 1/Nf_s$. In this way, high symbol rates can be achieved at a reduced signal bandwidth without ISI as shown in Fig. 4.4. After transmission, the signal is OTDM demultiplexed and converted to a data signal loaded on a CW carrier by employing an RZ-CW conversion process [3].The experimental demonstration of coherent Nyquist pulse transmission is described in extensive detail in section 4.2.

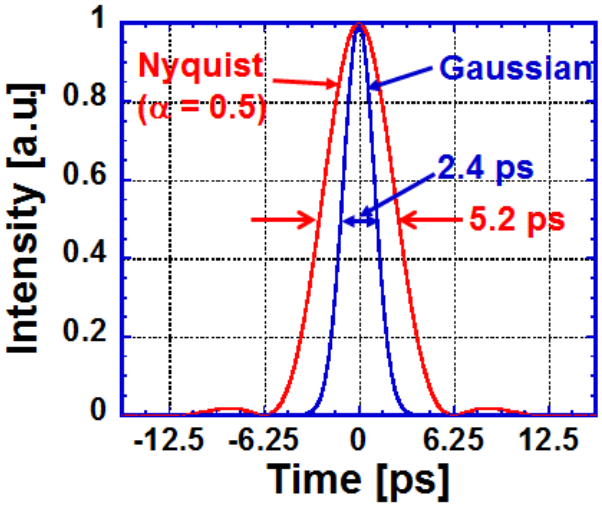

(a) Waveform

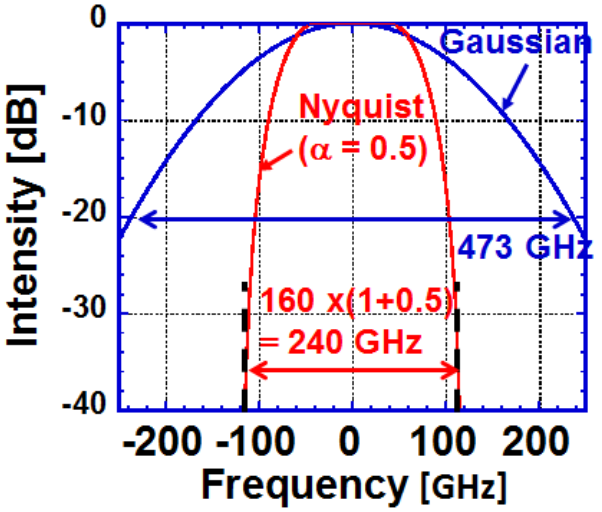

(b) Spectrum

Figure 4.3: Comparison of Gaussian and Nyquist pulses for the 160 Gbaud experiment

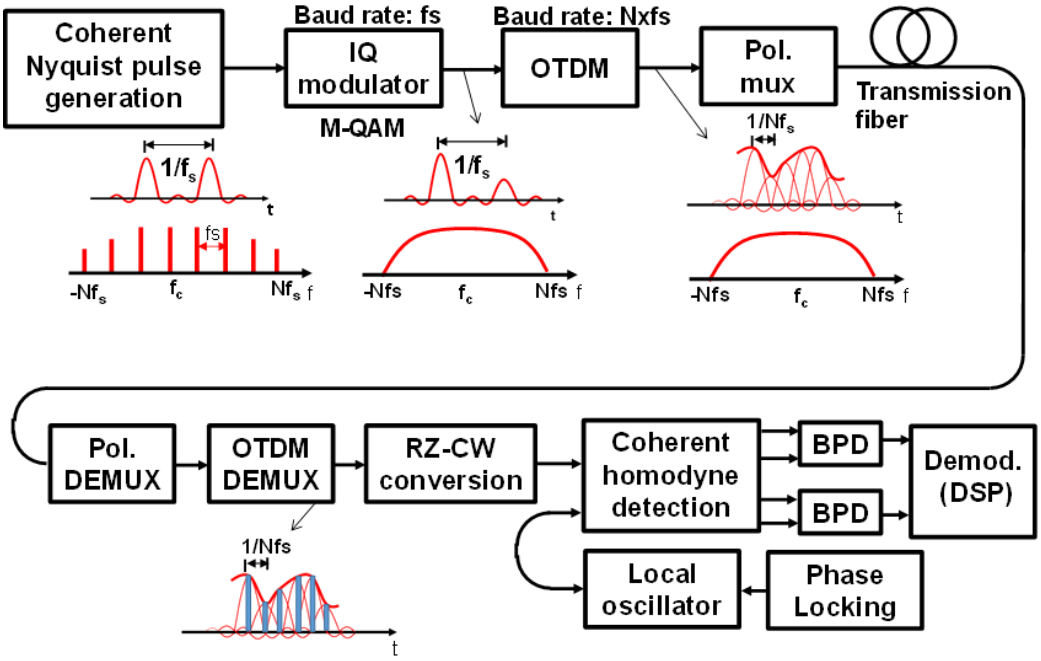

Figure 4.4: The principle of coherent Nyquist pulse transmission

4.2 Experimental setup for 1.92 Tbit/s, 64 QAM coherent Nyquist pulse transmission

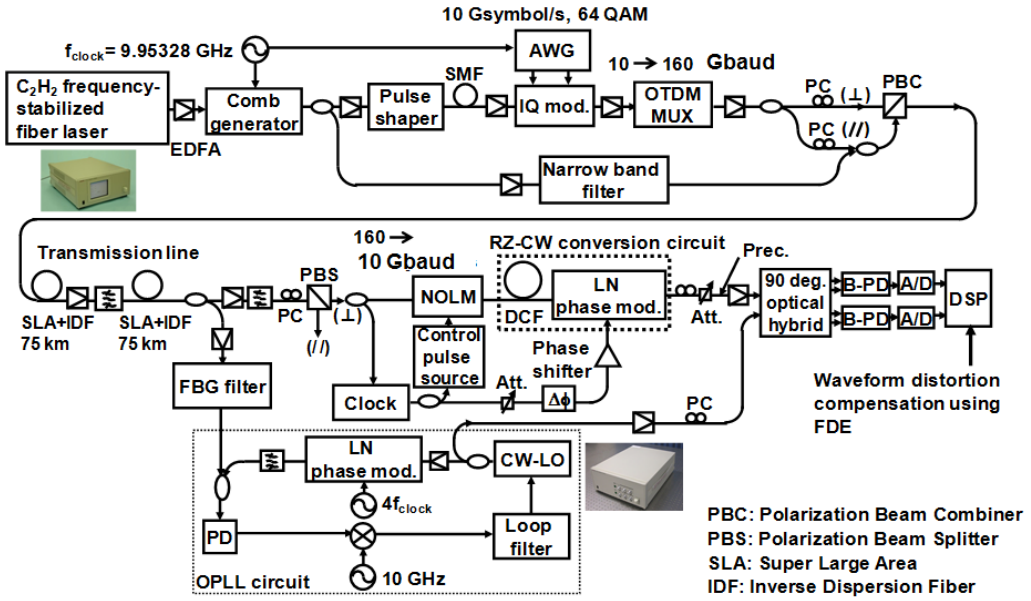

Figure 4.5: The experimental setup for 1.92 Tbit/s, 64 QAM coherent Nyquist pulse transmission

The experimental setup for a single-channel 1.92 Tbit/s, 64 QAM coherent optical Nyquist pulse transmission is shown in Fig. 4.5. At the transmitter, we used an acetylene (C_2H_2) frequency-stabilized fiber laser with a linewidth of 4 kHz described in chapter 2 [4] as a coherent optical source. The optical output from this laser was fed into a comb generator consisting of a dual-drive $LiNbO_3$ (LN) Mach-Zehnder modulator [5]. The optical comb generated was shown in chapter 3, where the spectral bandwidth of the comb was 490 GHz. The 150 km transmission line is the same as that used in chapter 3. After transmission, the signal was polarization demultiplexed, followed by optical sampling of the ISI-free points by use of a NOLM. The demultiplexed 10 Gbaud, 64 QAM signal was fed into an RZ-CW conversion circuit before homodyne detection and the data AD converted using a digital sample oscilloscope.

4.3 1.92 Tbit/s, 64 QAM Nyquist pulse signal generation

In this section I describe the generation of coherent Nyquist pulses in detail and also provide the time waveform and spectrum of the Nyquist pulse produced. A description of how the 1.92 Tbit/s, 64 QAM data signal is generated is also provided.

As mentioned in section 4.2, an acetylene frequency-stabilized fiber laser is used as a coherent light source. The CW laser output from this laser is passed through a comb generator, producing a broad comb. Using a programmable pulse shaper, a Nyquist pulse of desired roll-off factor α is carved out. Figure 4.6(a) and 4.6(b) show the waveform and spectrum of the Nyquist pulse generated, respectively. The roll-off factor was 0.5.

The pulse train, after modulation using an IQ modulator driven by an arbitrary wave generator (AWG) with a 10 Gbaud, 64 QAM signal is OTDM multiplexed using a PLC-type bit interleaver followed by polarization multiplexing. The signal is then combined with a pilot tone signal, used for phase synchronization at the receiver as described in chapter 3. The spectrum of the data signal and pilot signal combined is shown in Fig. 4.7

The power of the signal fed into the fiber link was optimized by plotting the BER error obtained as a function of the launch power. As shown in Fig. 4.8, there was poor BER performance at lower values of the launch power as a result of degradation of the transmitted OSNR. The best BER performance was obtained when the transmission power was 4 dBm which was the same as a for the Gaussian pulse transmission in chapter 3. Any further increase in the launch power beyind this value led to increased fiber nonlinearity and hence a decrease in the BER performance.

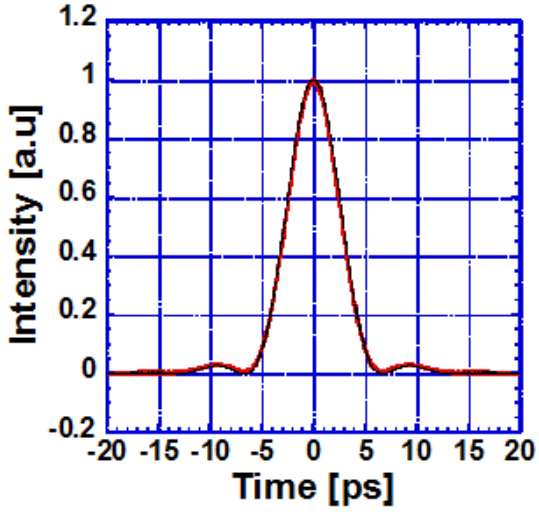

(a) Waveform

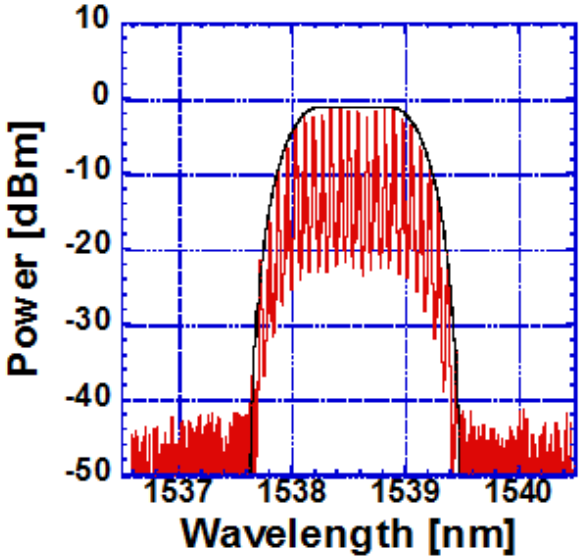

(b) Spectrum

Figure 4.6: Nyquist pulse $\alpha = 0.5$

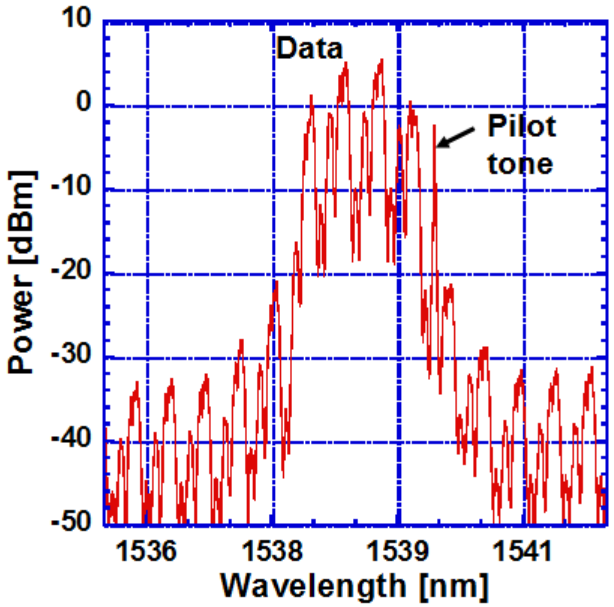

Figure 4.7: The spectrum for the 1.92 Tbit/s, 64 QAM coherent Nyquist pulse data combined with a pilot tone signal

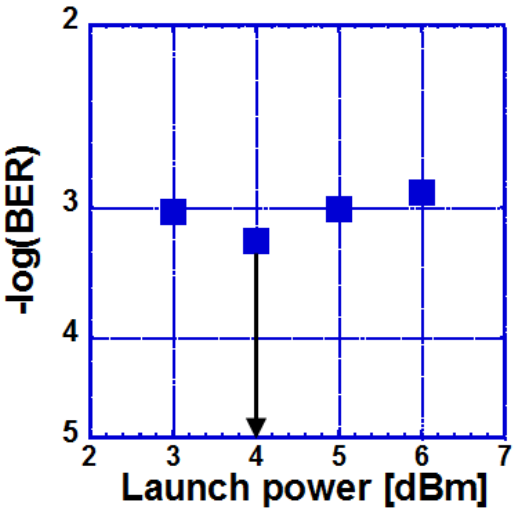

Figure 4.8: BER as a function of the launch power

4.4 OTDM demultiplexing by optical sampling

After polarization demultiplexing, the Nyquist OTDM data signal was demultiplexed using a nonlinear optical loop mirror by sampling out as narrowly as possible the ISI-free points on the Nyquist data train. In order to be able to use this optical sampling method, generating a very narrow control pulse was necessary. The process of control pulse generation was very similar to that described in chapter 3. The control pulse generation unit consisted of a DFB

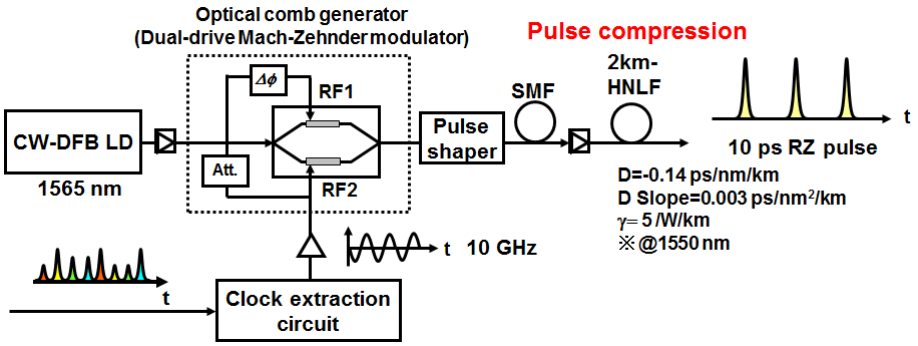

Figure 4.9: The control pulse generation circuit

LD CW source, a comb generator and a pulse shaper as shown in Fig. 4.9. This time, in order to obtain much shorter pulse, I used a highly nonlinear fiber(HNLF)of length 2 km to compress the pulse further from 2.4 ps to 800 fs. The dispersion and dispersion slope of the HNLF were -0.14 $ps/nm/km$ and 0.003 $ps/nm^2/km$. The nonlinear coefficient γ was 5 $W^{-1}km^{-1}$. The waveform and spectrum of the control pulse obtained is shown in Fig. 4.10. The spectral profile of the compressed pulse deviates from the idea Gaussian profile that was before compression. This is because the residual chirp from the comb generator that could not be compensated for using the SMF. This uneven spectral profile results in a pedestal on the time waveform shown in Fig. 4.10(a). However, this does not affect the demultiplexing performance greatly because of nonlinear characteristics of the NOLM transmittance.

I carried out two optimization experiments, first, of the input power of the OTDM signal into the NOLM. The signal input power into the NOLM was optimized by varying the input power while observing the demodulation performance. The viewgraph in Fig. 4.11(a) shows the BER performance as a function of the signal input power into the NOLM. The best performance was obtained with the value of about 17.5 dBm. At input powers below 17.5 dBm, due insufficient OSNR the BER performance was poor. At powers above 17.5 dBm, as a result of increased fiber nonlinearity that occurs in the HNLF in

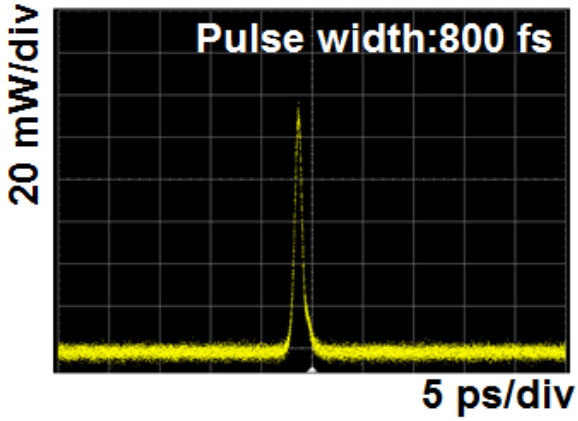

(a) Waveform

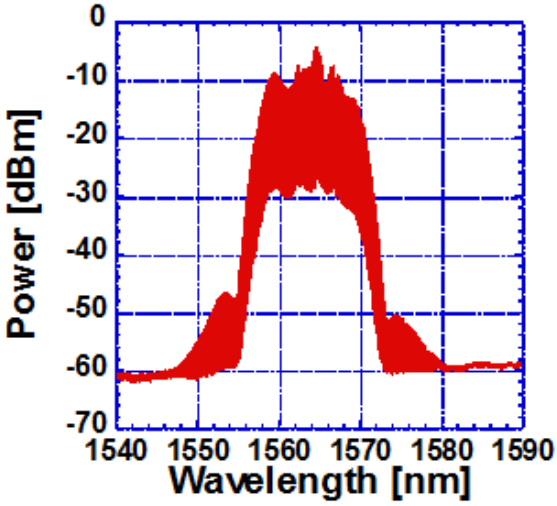

(b) Spectrum

Figure 4.10: The control pulse waveform and spectrum

NOLM that could not be compensated for at the transmitter. Secondly, the control pulse width was also varied while the demodulation performance was measured. A control pulse of 800 fs was found to be optimum as shown by the viewgraph in Fig. 4.6. When the control pulse was broader than 800 fs, the influx of ISI from adjacent tributaries resulted in the degradation of ther BER. As the pulse width is decreased below 800 fs, the decrease of the demultiplexed signal power results in OSNR degradation of the signal after amplification, before detection.

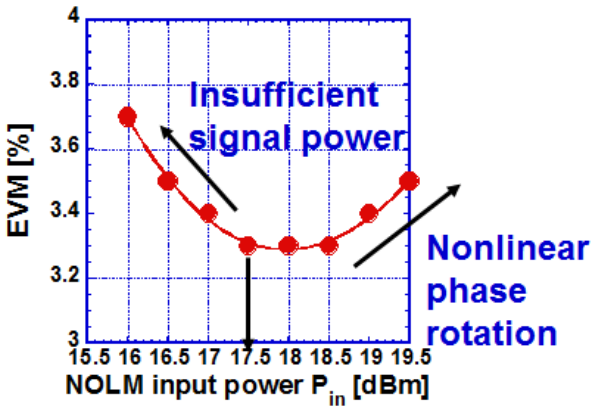

(a) Signal input power

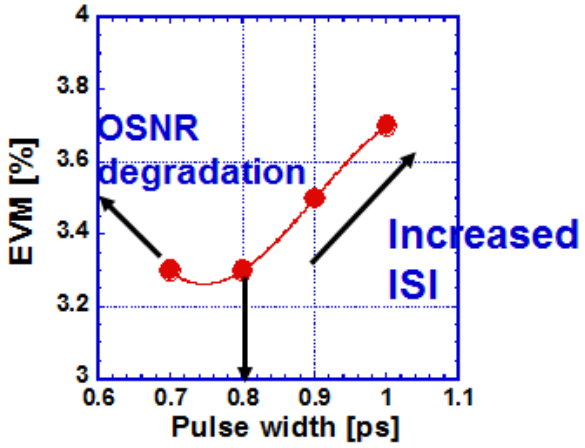

(b) Control pulse width

Figure 4.11: NOLM optimization

4.5 RZ-CW conversion process and characteristics

The demultiplexed data signal was then passed through an RZ-CW conversion circuit similar to that used in chapter 2. The parameters such as dispersion and chirp rate were set to be the same as for Gaussian pulse transmission. The spectra of the signal before and after RZ-CW conversion are shown in Fig. 4.12. The was a 9 dB improvement in power resulting from the RZ-CW conversion. This value is greater than that obtained when using Gaussian pulses. The reason for this difference can be attributed to the fact that the demultiplexed Nyquist TDM signal has a broader spectrum than that of the Gaussian TDM signal. The broad spectral bandwidth means that the RZ-CW conversion efficiency [8] is greater when using with

the much narrower demultiplexed Nyquist signal. The secondary peaks on

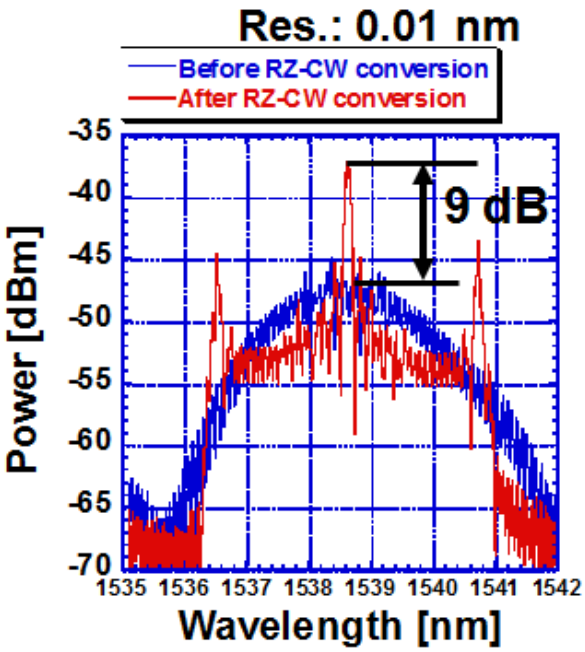

Figure 4.12: RZ-CW conversion characteristics

the spectrum, 2 nm from the center wavelength, result from adjacent symbols interfering with one another after the signal is passed through the dispersive medium in the RZ-CW conversion circuit.

4.6 Transmission results

The BER as a function of the received power was measured and it is shown in Fig. 4.14(a).The BER under back-to-back condition is shown in plots in red. That after 150 km of transmission is plotted in blue. The power penalty at the BER of 2×10^{-3} was 4.5 dB. This penalty is 0.5 dB less than obtained with Gaussian pulse. The improvement in performance with Nyquist pulses can be attributed to improved polarization mode dispersion (PMD) tolerance with Nyquist pulses. The BER for all the 16 tributaries is shown in Fig. 4.14(b). The error floor on the BER curve was as a result of the XPM between the two polarizations.

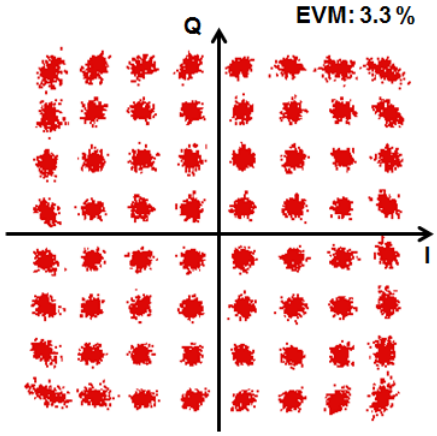

(a) Back-to-back

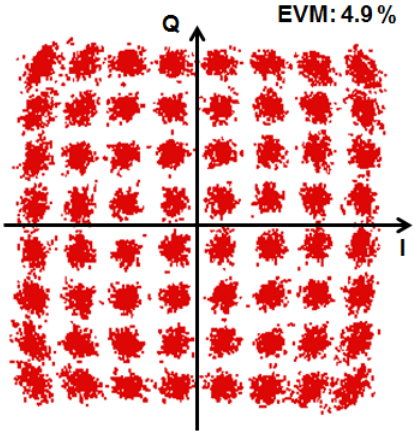

(b) After 150 km

Figure 4.13: constellation map, before and after 150 km

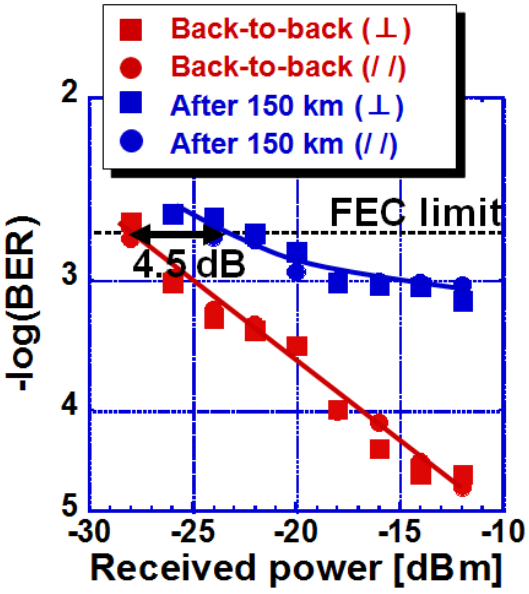

(a) Signal input power

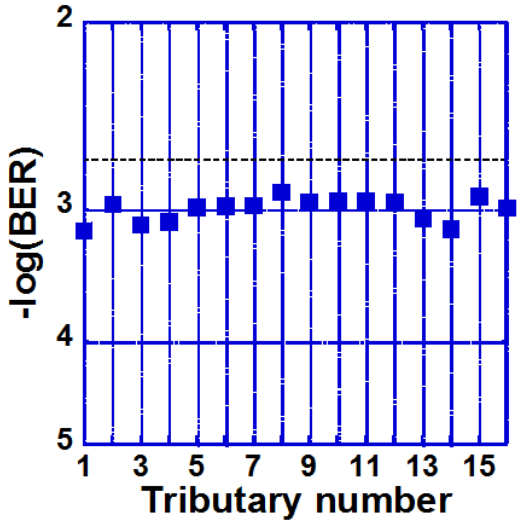

(b) BER for all the 16 tributaries

Figure 4.14: Bit error rate characteristics

4.7 Discsussion and conclusion

In this chapter, I proposed a coherent Nyquist pulse and its high-speed OTDM transmission. A coherent Nyquist pulse for 160 Gbaud transmission was generated by including a pulse shaper after the comb generator and precisely manipulating the amplitude and phase of each longitudinal mode. In the receiver, an ultrafast optical sampling circuit comprising NOLM is newly developed. The switching gate width was optimized to be 800 fs against the symbol period of 6.25 ps, by taking account of the trade-off between the OSNR degradation due to excessive narrow gate and the penetration of adjacent tributaries due to excessive wide gate. RZ-CW conversion scheme was also successfully demonstrated for Nyquist pulses, in which the SNR improvement was as large as 9 dB. As a result, 1.92 Tbit/s/ch, 64 QAM signal was transmitted over 150 km within a spectral bandwidth of 240 GHz, resulting in a spectral efficiency

$$SE = \frac{1.92\ Tbit/s}{240\ GHz\ \times\ 1.07(7\%\ FEC)} = 7.5\ bit/s/Hz \tag{4.3}$$

The spectral efficiency given above is considered, even when the 7% FEC overhead is taken into consideration. For further increase in spectral efficiency, Nyquist pulses of lower roll-off factors are required. In the next chaper a novel transmission scheme is brought about without decreasing demodulation performance even under a low roll-off factor.

Chapter 4 References

[1] M. Nakazawa, T. Hirooka, P. Ruan, and P. Guan, "Ultrahigh-speed "orthogonal" TDM transmission with an optical Nyquist pulse train," *Opt. Exp.* 20(2), pp. 1129-1140 (2012).

[2] H. Nyquist, "Certain topics in telegraph transmission theory," *Trans. Am. Inst. Electric. Eng.* 47, 617-644, (1928).

[3] M. Nakazawa, K. Kasai, M. Yoshida, and T. Hirooka, "Novel RZ-CW conversion scheme for ultra multi-level, high-speed coherent OTDM transmission,"*Opt. Exp.* 19(26), $B574^{-}$ $B580$, (1996).

[4] K. Kasai, A. Suzuki, M. Yoshida, and M. Nakazawa, "Performance improvement of an acetylene (C_2H_2) frequency-stabilized fiber laser," *IEICE Electron. Express* 3(22), 487^{-} 492 (2006).

[5] T. Sakamoto, T. Kawanishi, and M. Izutsu, "Asymptotic formalism for ultraflat optical frequency comb generation using a Mach-Zehnder modulator," *Opt. Lett.* 32(11), 1515^{-} 1517 (2007).

[6] G. Baxter, S. Frisken, D. Abakoumov, H. Zhou, I. Clarke, A. Bartos, and S. Poole, "Highly programmable wavelength selective switch based on liquid crystal on silicon switching elements," in Proceedings of the *Optical Fiber Communication Conference (OFC)*,Anaheim, 2006, OTuF2.

[7] C. Boerner, V. Marembert, S. Ferber, C. Schubert, C. Schmidt-Langhorst, R. Ludwig, and H. G. Weber, "320 Gbit/s clock recovery with electro-optical PLL using a bidirectionally operated electroabsorption modulator as phase comparator," in Proceedings of the *Optical Fiber Communication Conference (OFC)*, Anaheim, 2005, OTuO3.

[8] M. Nakazawa, K. Kasai, M. Yoshida, and T. Hirooka, "Novel RZ-CW conversion scheme for ultra multi-level, high-speed coherent OTDM transmission,"*Opt. Exp.* 19(26), $B574^{-}$ $B580$, (1996).

Chapter 5

Ultrahigh-speed and high spectrally efficient coherent orthogonal Nyquist TDM transmission

In this chapter, I propose a novel scheme for OTDM transmission by taking advantage of the time-domain orthogonality of the coherent Nyquist pulse. In this scheme, a Nyquist pulse is also used as a local oscillator, whose phase is synchronized to the transmitted Nyquist pulse. By taking a homodyne detection of these pulses with a balanced photo diode, the coherent Nyquist OTDM signal can be demultiplexed and demodulated simultaneously. This results in a high performance demultiplexing and much simpler receiver configuration compared to the ultrafast sampling scheme. In this chapter, I develop the new coherent receiver and demonstrate that this scheme exhibits better performance than the ultrafast sampling scheme. With the use of this scheme, I was able to decrease the spectral bandwidth required for transmission and hence the spectral efficiency by using a Nyquist pulse with a roll-off factor α of 0, which can take full advantage of the orthogonal property. With this scheme, 1.92 Tbit/s, 64 QAM transmission over 150 km was achieved with a spectral bandwidth of only 170 GHz, resulting in a spectral efficiency of as high as 10.6 bit/s/Hz. This is the highest SE that has been achieved in a single-carrier transmission beyond 1 Tbit/s. To further increase the transmission distance beyond 150 km, I newly introduced digital back propagation (DBP) and Raman amplification, which made it possible for to increase the transmission distance to 225 km. Finally, I describe the increase in transmission speed from 1.92 Tbit/s to 3.84 Tbit/s by doubling the symbol rate from 160 Gbaud to 320 Gbaud. This is realized by newly employing a HCN

frequency-stabilized mode-locked fiber laser (MLFL) that can directly emit a high OSNR coherent optical pulse.

5.1 The principle of orthogonality-based Nyquist TDM demultiplexing scheme

This section covers the principle of the novel Nyquist OTDM demultiplexing scheme based on the time domain orthogonality of Nyquist pulses [1]- [4]. It begins by describing what Nyquist pulse time domain orthogonality is. If we assume that the Nyquist pulse [5] envelope centered at time $t = 0$ to be

$$\phi(t) = \frac{\sin(\frac{\pi t}{T})}{\frac{\pi t}{T}} \frac{\cos(\frac{\alpha \pi t}{T})}{1 - \left(2\frac{\alpha t}{T}\right)^2} \tag{5.1}$$

where α is the roll-off factor and T the zero crossing interval of the oscillating tail. If the Nyquist pulse centered at $t = nT$ is represented as $\phi_n(t) = \phi(t - nT)$, the orthogonality condition between any two periodic time separated Nyquist pulses can be expressed by the equation

$$\frac{1}{T}\int_{-\infty}^{\infty} \phi_n(t)\phi_m(t)dt = \begin{cases} 1, & n = m \\ 0, & n \neq m \end{cases}$$

which holds when the roll-off factor $\alpha = 0$.

This orthogonality condition is not very strict or limited when $\alpha \neq 0$, but there is a quasi-orthogonality property for other roll-off factors. The overlap integral shown above for the Nyquist pulse of other roll-off factors depend on the difference between m and n. Figure 5.1(a) shows the overlap integral as a function of $m-n$ when $\alpha = 0.5$. The value of the overlap integral becomes 0.9 when $m = n$. When $m \neq n$, the overlap integral approaches zero asymptotically as $|m - n|$ increases. In Fig. 5.1(b), the value of the overlap integral is evaluated as a function of the roll-off factor α. For $m - n = 0$, the value decreases from 1 to 0.75 when $\alpha = 1$. Meanwhile when $m - n = 1$, the integral increases from zero to 0.13 when $\alpha = 1$.

If we now consider a Nyquist TDM signal $g(t)$ shown in Fig. 5.2 to be the sum of the individual Nyquist pulses modulated by the corresponding symbols g_n at time $t = nT$. The analog-like TDM signal $g(t)$ can then be expressed as

$$g(t) = \sum_{n=-\infty}^{\infty} g_n \phi_n(t) \tag{5.2}$$

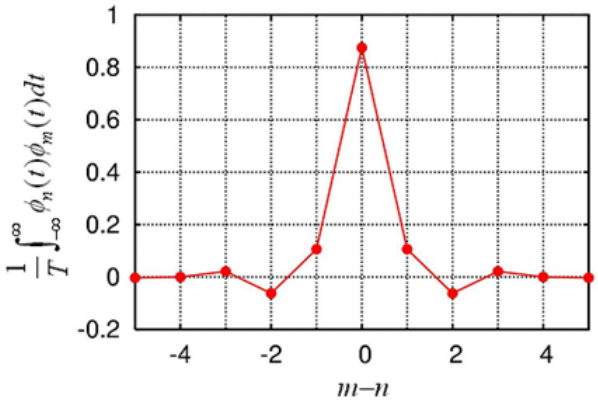

(a) Overlap integral for $\alpha = 0.5$ as a function of $m - n$

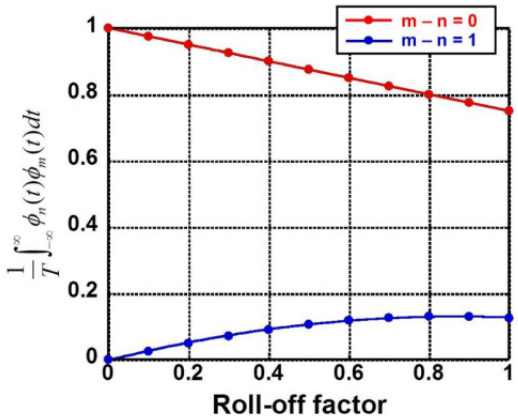

(b) Overlap integral dependence on the roll-off factor α when both $m - n \neq 0$ and when $m - n = 0$

Figure 5.1: The overlap integral as a function of the roll-off factor.

The expression in equation (5.2) satisfies the following equation

$$g_n = \frac{1}{T}\int_{-\infty}^{\infty} g(t)\phi_n(t)dt \tag{5.3}$$

meaning that the symbol data g_n can be extracted from the analog-like data signal $g(t)$ by integrating the product of $g(t)$ and the Nyquist pulse $\phi_n(t)$ centered at $t = nT$. So being able to find the product $g(t)\phi_n(t)$ is an important prerequisite in demultiplexing the tributaries in $g(t)$ using the orthogonality based demultiplexing scheme.

The demultiplexing process explained in the previous paragraph can be achieved experimentally by photomixing the Nyquist OTDM signal $g(t)$ and a synchronized Nyquist LO pulse $\phi_n(t)$. The experimental setup shown in

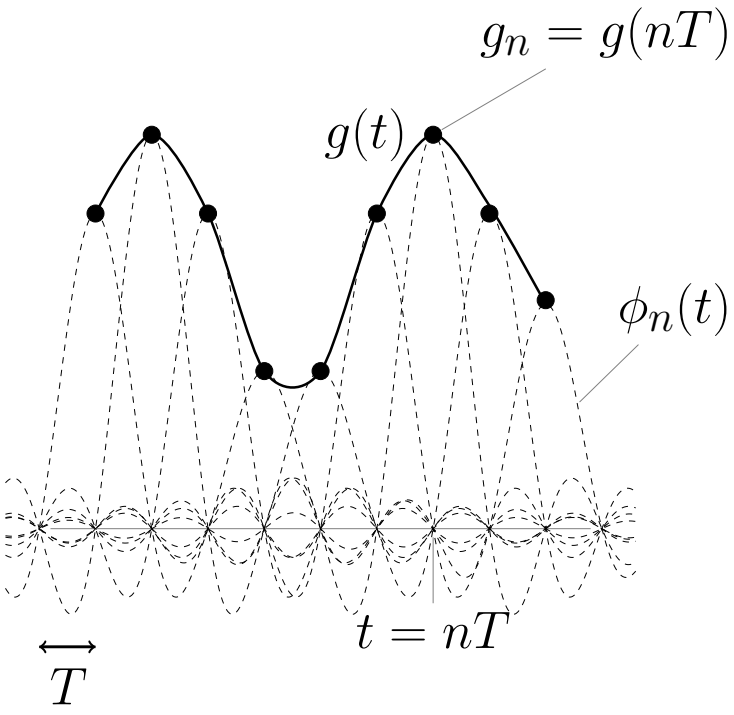

Figure 5.2: Nyquist TDM signal

Fig. 5.3 shows the Nyquist TDM signal being fed simultaneously with a Nyquist LO pulse into a photomixer. The optical output $E_1(t)$ and $E_2(t)$

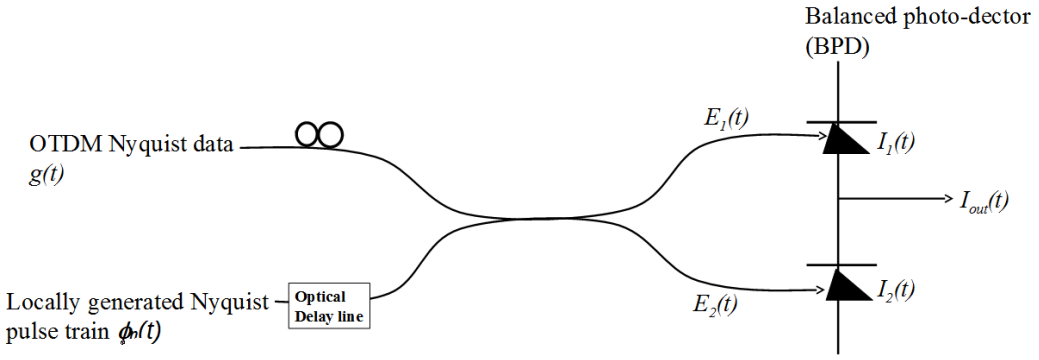

Figure 5.3: Nyquist pulse demultiplexing by photomixing the Nyquist TDM signal $g(t)$ with a locally generated Nyquist pulse train $\phi_n(t)$

from the photomixer is the sum and difference of the signals at the input,

respectively, i.e.,

$$E_1(t) = g(t) + \phi_n(t) \tag{5.4}$$
$$E_2(t) = g(t) - \phi_n(t)$$

Therefore the detected photocurrent $I_{out}(t)$ is then proportional the product of $g(t)$ and $\phi_n(t)$, expressed as

$$I_{out}(t) = I_1 - I_2(t) \propto g(t)\phi_n(t) \tag{5.5}$$

Therefore the product of the TDM Nyquist signal and the locally generated pulse LO can be generated by photomixing of the TDM signal and then detecting it using a BPD. As shown in Fig. 5.4, if a band pass filter is placed

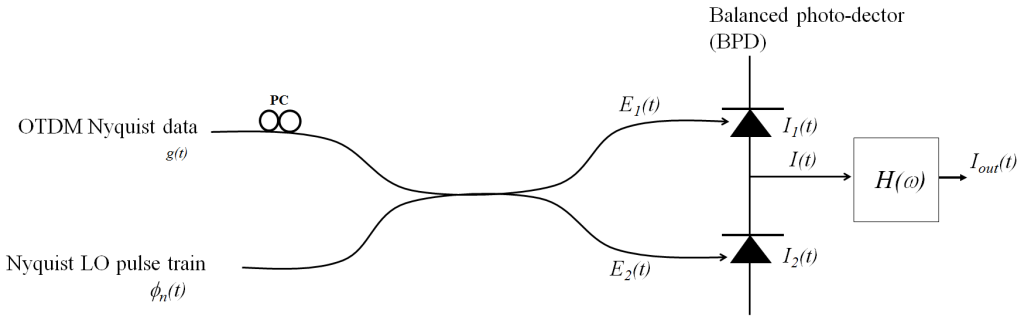

Figure 5.4: Nyquist pulse demultiplexing by photomixing the Nyquist TDM signal $g(t)$ with a locally generated Nyquist pulse train $\phi_n(t)$

after the balanced PD, the current out of the bandpass filter becomes

$$I_{out}(t) = \frac{1}{2\pi}\int_{-\infty}^{\infty} \tilde{I}(\omega)H(\omega)\exp(-j\omega t)d\omega \tag{5.6}$$

where $I(\tilde{\omega})$ is the Fourier transform of the current out the BPD. If the band-pass filter is considered to be an ideal filter with bandwidth Ω, the current above becomes

$$\begin{aligned} I_{out}(t) &= \frac{1}{2\pi}\int_{-\infty}^{\infty} I(t')\int_{-\infty}^{\infty} H(\omega)\exp(j\omega(t'-t))d\omega dt' \\ &= \frac{1}{2\pi}\int_{-\infty}^{\infty} I(t')\int_{0}^{\Omega} \exp(j\omega(t'-t))d\omega dt' \end{aligned} \tag{5.7}$$

for $\Omega(t'-t) << 1$, by Taylor's expansion and approximation, $I_{out}(t)$ can be approximated as follows

$$\begin{aligned} I_{out}(t) &= \frac{1}{2\pi}\int_{-\infty}^{\infty} I(t')\frac{\exp(j\Omega(t'-t))-1}{j(t'-t)}dt' \\ &\approx \frac{1}{2\pi}\int_{-\infty}^{\infty} I(t')\frac{[1+j\Omega(t'-t)]-1}{j(t'-t)}dt' \\ &= \frac{\Omega}{2\pi}\int_{-\infty}^{\infty} I(t')dt'. \end{aligned} \tag{5.8}$$

When $\Omega = 2\pi/T$, I_{out} takes the form

$$I_{out}(t) = \frac{1}{T}\int_{-\infty}^{\infty} g(t)\phi_n dt \tag{5.9}$$

Therefore, the symbol data g_n can be extracted from the TDM signal $g(t)$ by homodyne photomixing. This scheme is advantageous in that it achieves both TDM demultiplexing and homodyne detection simultaneously.

5.2 Demonstration of demultiplexing by orthogonality

We first carried out a proof-of-concept of this scheme using an 80 Gbaud, 64 QAM signal. Figure 5.5 shows an experimental setup that was used to demonstrate this novel demultiplexing scheme that is based on the time domain orthogonality of Nyquist pulses. At the transmitter, a 10 GHz Nyquist pulse with a roll-off factor $\alpha = 0$ is generated, which was modulated with a 10 Gbaud 64 QAM signal and OTDM multiplexed to 80 Gbaud. By using a similar process as that at the transmitter, a 10 GHz local Nyquist pulse train having a roll-off factor $\alpha = 0$ was generated. An OPLL circuit was used for phase synchronization of the CW-LO to the data signal. After homodyne detection using the Nyquist-LO, the data signal was demodulated in an offline condition. The bandwidth of the balanced PD was 47 GHz and the digital sampling oscilloscope has a sampling rate of 80 Gsample/s, while its analog bandwidth was 32 GHz.

The demodulation performances for the scheme that employed optical sampling and that that employed the novel scheme were compared. The sampling gate width was set at 0.86 ps. When $\alpha = 0$, as shown by the constellation maps in Fig. 5.6, the EVM decreased from 4.1% to 3.4% with the adoption of the new demultiplexing scheme. When the roll-off factor was increased to $\alpha = 0.5$, the EVM decreased from 3.6% with the optical

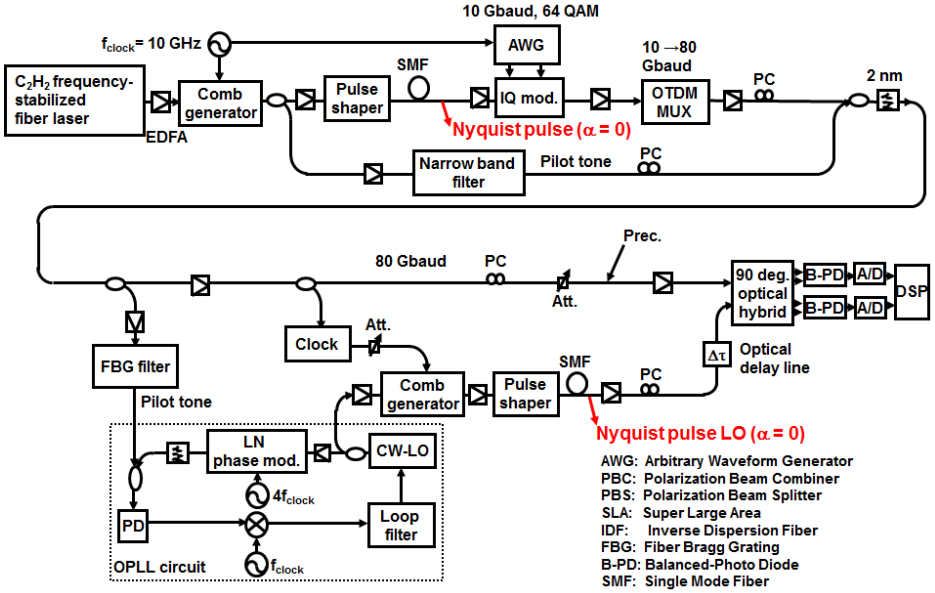

Figure 5.5: The experimental setup to demonstrate the Nyquist TDM demultiplexing scheme based on Nyquist pulse time domain orthogonality

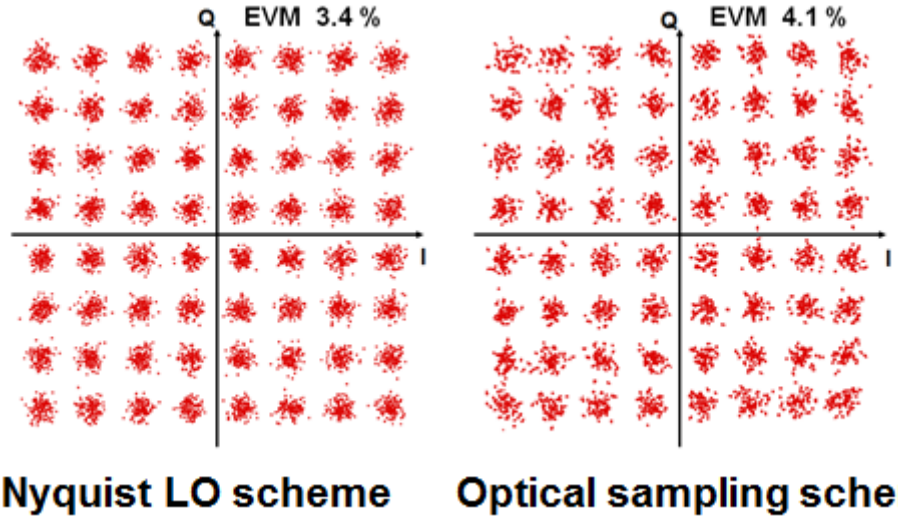

Figure 5.6: Constellation maps of the demultiplexed 10 Gbaud, 64 QAM signal ($\alpha = 0$)

sampling scheme to 3.0% with the orthogonality based scheme as shown in Fig. 5.7. The BER performance for the two schemes is summarised in Fig. 5.8. From the figure, it can be seen that there is a noticeable improvement

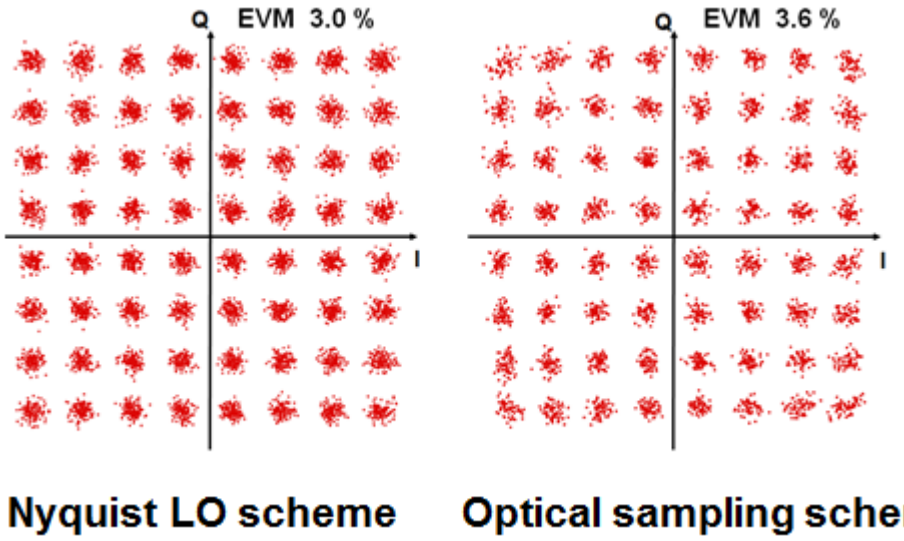

Figure 5.7: Constellation maps of the demultiplexed 10 Gbaud, 64 QAM signal ($\alpha = 0.5$)

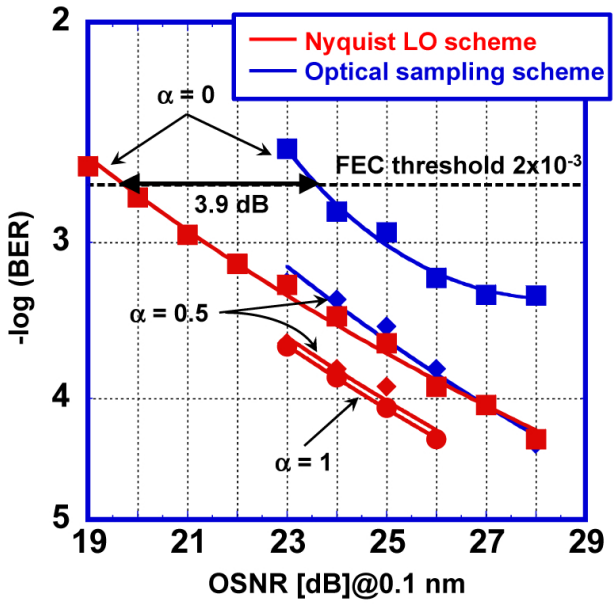

Figure 5.8: The BER performance comparing the performances of the optical sampling and othogonality-based demultiplexing schemes

in the BER performance with the introduction of the new demultiplexing scheme.

The BER performance with Nyquist pulses with roll-off factor $\alpha = 0$ was less than that when Nyquist pulses with roll-off factors $\alpha = 0.5$ and 1. This is attributed to fact that signals with a higher spectral efficiency require more SNR for demodulation as compared to those with lower spectral efficiency. Since the bandwidth of Nyquist pulse is equivalent to $B_0(1+\alpha)$, where B_0 is the bandwidth for a Nyquist pulse with the roll-off factor α of 0, increased roll-factors signify lower spectral efficiency and hence less SNR requirement.

5.3 1.92 Tbit/s, 64 QAM Nyquist pulse transmission using orthogonality-based demultiplexing scheme

Based on the demonstration of high performance demultiplexing in section 5.2, the new demultiplexing scheme was adopted into a 1.92 Tbit/s, 64 QAM transmission experiment. Due to the better performance even with Nyquist pulses of roll-off factor $\alpha = 0$, in order to improve the spectral efficiency further, a Nyquist pulse of roll-off factor $\alpha = 0$ was used. Figure 5.9 shows the experimental setup used for the 1.92 Tbit/s, 64 QAM Nyquist pulse data signal. The setup is mainly divided into the transmitter, fiber link and receiver. First, at the transmitter, a broad comb was generated from CW laser [**?**] output using a dual drive MZM comb generator [**?**]. A 10 GHz Nyquist pulse train with periodic zero-crossing interval of 6.25 ps was carved off the broad comb using a pulse shaper [**?**]. We compensated for the chirp created during comb generation using a 470 m long SMF. The pulse train was then modulated using an IQ modulator and with a 10 Gsymbol/s, 64 QAM signal from and arbitrary waveform generator (AWG). Using a PLC-type OTDM multiplexer, the symbol rate was increased to 160 Gbaud. Furthermore, by passing the signal through polarization multiplexing (Pol Mux) circuit, the bit rate was doubled to 1.92 Tbit/s. In parallel, a CW pilot tone signal was generated by filtering out the -9th harmonic (at 90 GHz from the central frequency) of the comb signal. This was combined with the OTDM-Pol multiplexed signal and fed into the transmission link at an optimized transmission power of 4 dBm. At the receiver, the signal was first polarization demultiplexed, before being fed into the coherent receiver. In order to generate the local Nyquist pulse, a clock signal was recovered from the data signal which was used to drive a comb generator [**?**].

The optical waveform and spectrum of the generated Nyquist pulse with a roll-off factor $\alpha = 0$ is shown in Fig. 5.10. There were 17 harmonics in the spectrum which were flat, with the suppression ratio of the side modes of

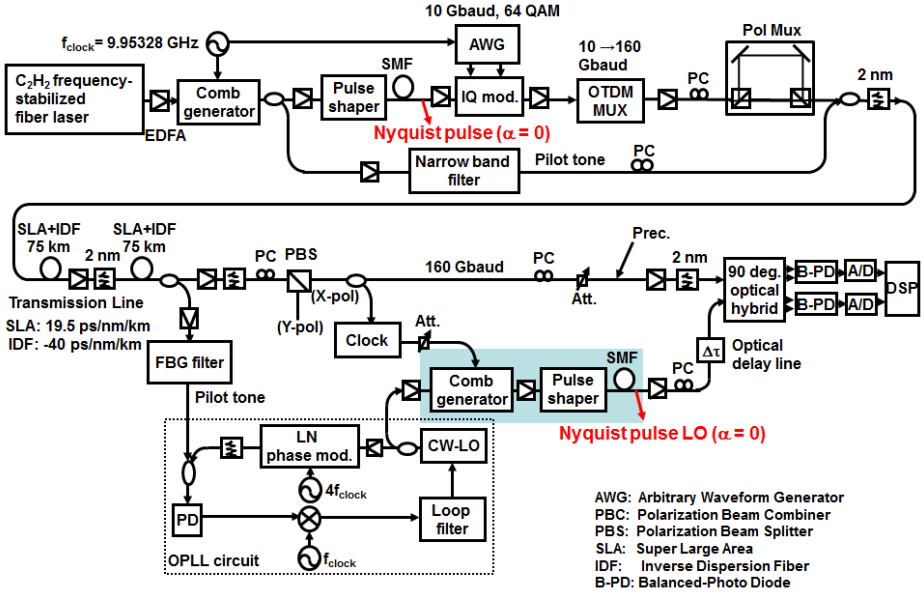

Figure 5.9: The experimental setup for the 1.92 Tbit/s, 64 QAM Nyquist TDM transmission, single polarization receiver system

20 dB. Figure 5.11 shows the optical spectra measured before and after 150

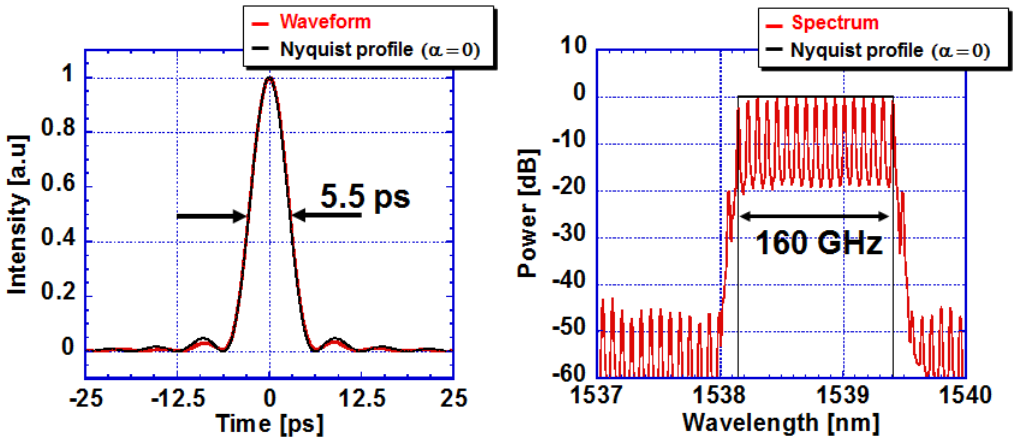

(a) waveform (b) Spectrum (Res. 0.02 nm)

Figure 5.10: Generated Nyquist pulse

km transmission at a resolution of 0.1 nm. The OSNR degradation resulting from the transmission was 14 dB, as shown in Fig. 5.11. The bit error rate for the transmission experiment is shown in Fig. 5.12. Fig.5.12(a) shows the bit error rate as a function of the received power, where the power penalty

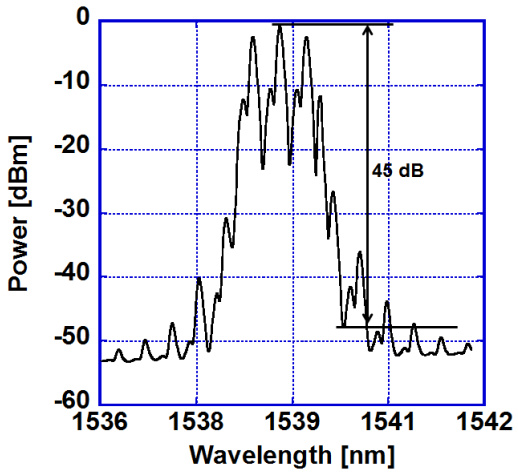

(a) Optical Spectrum before transmission

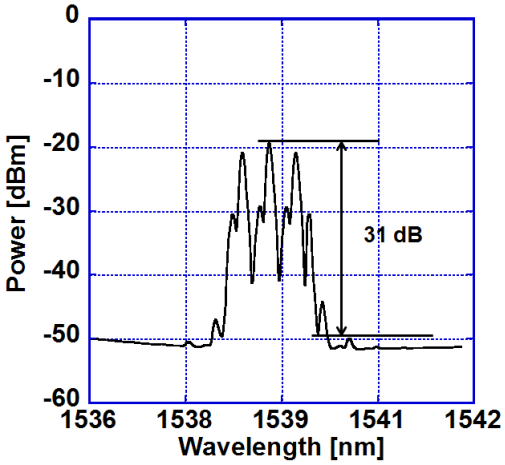

(b) Optical Spectrum after 150 km transmission

Figure 5.11: Optical spectra, before and after 150 km (Res. 0.1 nm)

at the BER of 2×10^{-3} was 4.8 dB. This power penalty was greater than the 4.5 dB, when Nyquist of roll-off factor $\alpha = 0.5$ was demultiplexed using an optical sampling scheme in chapter 4. The corresponding BER for all the 16 tributaries, measured at the maximum received power is shown in Fig. 5.12(b). For all the tributaries a performance of below FEC limit was obtained.

In order to improve the performance of this system further, there is need to convert the receiver from a single polarization receiver system to a dual polarization receiver system where both polarizations can be received and waveform impairments such as XPM between two polarizations can be com-

pensated for. The improvements of the transmission system are described in the next section.

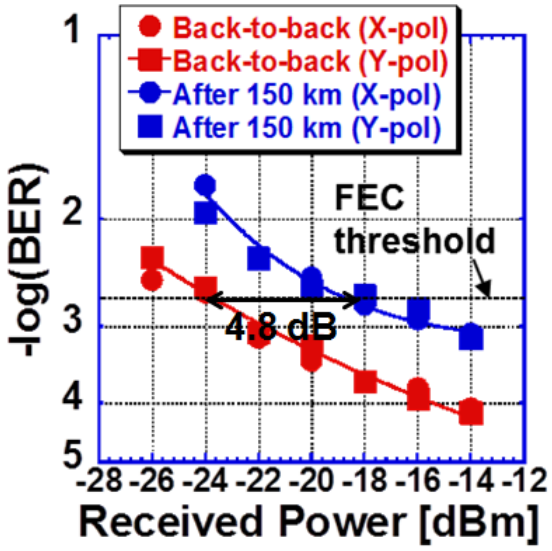

(a) BER as a function of the received power for a single tributary

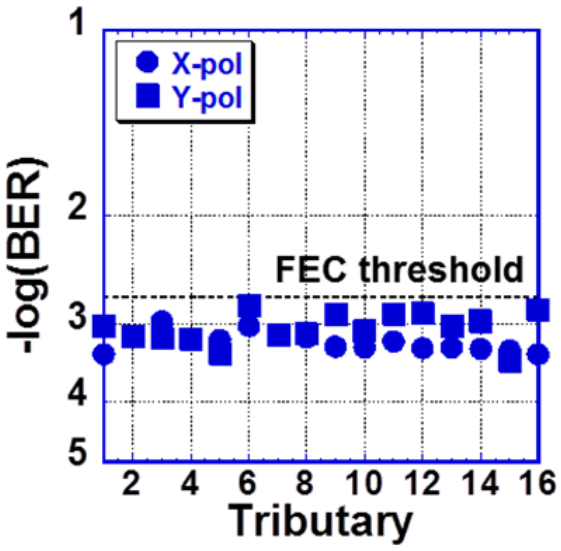

(b) BER for all the 16 tributaries

Figure 5.12: Bit error rate (BER) for the demodulated 10 Gbaud, 64 QAM data signal.

5.4 Performance improvement of Nyquist pulse transmission with digital back-propagation and Raman amplification

I undertook three main steps to improve the transmission experiment. The first step involved transforming the experimental setup from a single polarization receiver system to a daul polarization receiver system, in which the polarization demultiplexing is carried out in the DSP. The second improvement in the experimental setup involved applying digital back propagation (DBP) to the transmission experiment to compensate the impairments due to fiber nonlinearities of the transmitted signal. This was made possible by the fact that the system was able to receive both polarizations simultaneously. The third improvement was the introduction of Raman amplification to improve on the transmitted OSNR while suppressing the fiber nonlinearity. The experimental setup is shown in Fig. 5.13. I will introduce the principle of each of the two techniques:

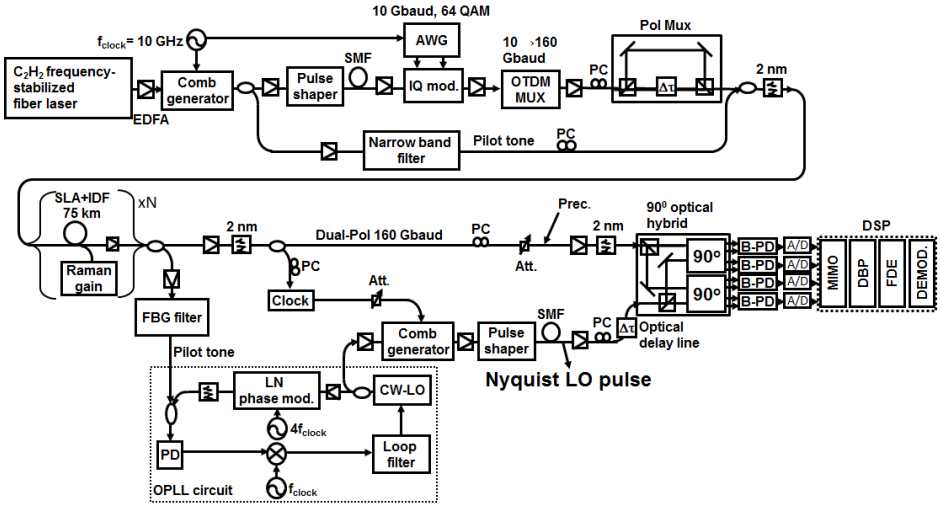

Figure 5.13: The experimental setup for the 1.92 Tbit/s, 64 QAM Nyquist TDM transmission employing polarization diversity configuration

5.4.1 Digital back propagation process

The equation that governs the propagation of optical pulses through an optical fiber is the Manakov equation shown in Eq. (5.10).

$$-j\frac{\partial}{\partial z}\begin{bmatrix}E_x(z,t)\\E_y(z,t)\end{bmatrix} = (\hat{D}+\hat{N})\begin{bmatrix}E_x(z,t)\\E_y(z,t)\end{bmatrix}$$

$$\hat{D} = j\frac{1}{2}\alpha - \frac{\beta_2}{2!}\frac{\partial^2}{\partial t^2}$$

$$\hat{N} = \frac{8}{9}\gamma\left[|E_x|^2 + |E_y|^2\right] \tag{5.10}$$

where $E_x(z,t)$ and $E_y(z,t)$ are the instantaneous electric fields of the orthogonal polarizations propagating through the fiber link, while $\hat{D}$ and $\hat{N}$ are the linear and nonlinear operators, respectively. α is the attenuation coefficient of the fiber, β_2 the group velocity dispersion and γ is the fiber nonlinear coefficient. In order to compensate for the nonlinearity, Ref. [8] proposed to let the transmitted signal propagate through a fiber with opposite sign of nonlinearity, loss, and gain, namely backward propagation.Digital back propagation (DBP) is a digital signal processing used for implementing this backward propagation. The block diagram for the digital back propagation is shown in Fig. 5.14. The method uses a split step Fourier method, in which the received data is numerically propagated backwards through the fiber. The fiber is split into short steps of length h. Within the very short step of length h, first the signal is amplified, and the dispersion for half the length $h/2$ compensated numerically, then both the nonlinear phase rotations of SPM and XPM are compensated for before finally compensating for the remaining dispersion.

It is worth noting that the received OTDM signal is spectrally limited by the bandwidth of the coherent receiver. The bandwidth of the received signal is not that of the signal that propagates through the fiber. In order to reconstruct a signal with the same bandwidth as that before coherent reception, the signal that is digitally back propagated, the signal is loaded on a Nyquist pulse in use before the digital back propagation is applied to it. This is done by numerically generating a Nyquist pulse profile, and multiplying it by the received data signal. The multiplication is done in such a way that the peak of the pulse coincides with the clock period.

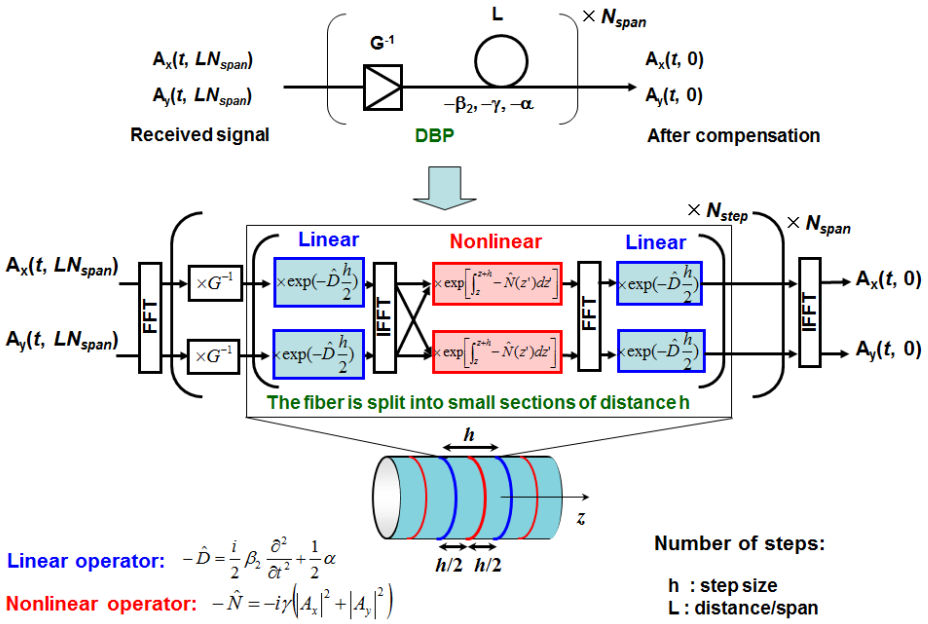

Figure 5.14: The digital back propagation process

5.4.2 The principle of Raman amplification

As mentioned previously, the use of Raman amplification aims at increasing the OSNR of the data signal after transmission while suppressing the nonlinear phase rotation in the fiber.

Raman amplificiation uses stimulated Raman scattering as a means of amplifying the photons traversing through the medium. Raman scattering is brought about by the scattering effect of optical phonon of molecules such GeO_2 and SiO_2. When light is fed into a material, a small fraction gets scattered while light of a lower frequency called Stokes wave is generated. Therefore, when a strong optical input is used, there can be an increased growth of the the Stokes beam with much of the light from the strong pump being converted to the Stokes beam. This is called stimulated Raman scattering. Stimulated Raman scattering can be used for amplification of light that traversed through a medium by pumping it with the light of the right wavelength [9]. Unlike EDFAs that provide gain at a fixed of a fiber link, also referred to as lumped amplification, Raman amplification takes place over a long distance of the fiber link, which is referred as distributed amplification. To achieve maximum Raman ampflication in the fiber, the pump should operate at 13.2 THz higher frequency than the signal frequency as shown by Fig. 5.15. The pump used for telecommunication Raman pumping are LDs

that operate around 1.44 μm region. For broad bandwidth pumping multi-pump Raman pumping has been demonstrated [10]. When using Raman

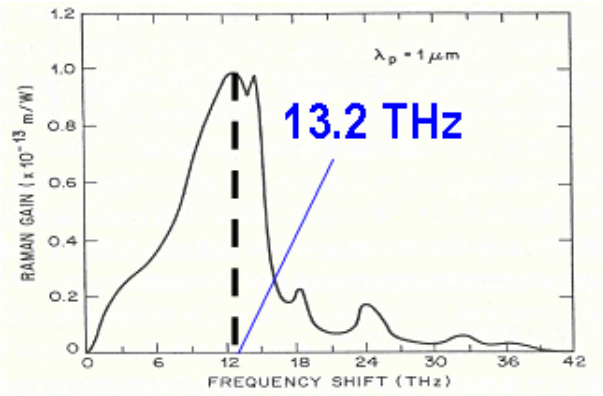

Figure 5.15: Raman gain distribution of silica glass

amplificating, backward pumping is utilized to avoid gain saturation. Figure 5.16 shows the configuration of Raman amplification. If fiber of length L is used with a signal of wavelength λ_s through it, when an LD pump wavelength λ_p is used, the rate increase in signal power intensity I_s and change in pump power intensity I_p can be expressed by equations

$$\begin{aligned} \frac{dI_s}{dz} &= g_R I_p I_s - \alpha_s I_s \\ \frac{dI_p}{dz} &= -\frac{\lambda_s}{\lambda_p} g_R I_p I_s - \alpha_p I_p \end{aligned} \tag{5.11}$$

where g_R is the Raman gain, while α_s and α_p are the attenuation coefficients for both signal and pump, respectively. The equations in (5.11) results in a gain profile shown in Fig. 5.17. The signal power decreases as it propagates and reaches a minimum, at a specific length, after which the intensity begins to rise again.

5.4.3 1.92 Tbit/s, 64 QAM transmission experiment with a dual polarization receiver

The experimental setup used in this section is very similar to that used in the previous section, with the exception that the received signal, now, was not polarization demultiplexed before homodyne detection. The system

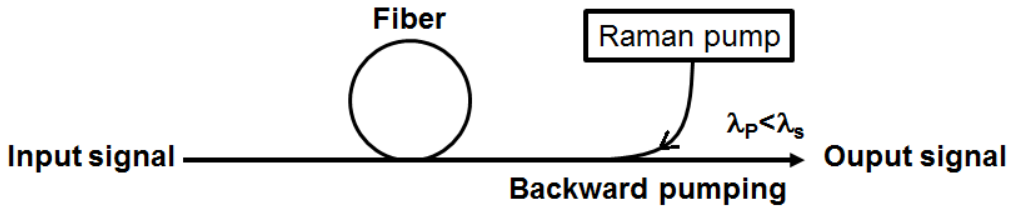

Figure 5.16: The configuration of Raman amplifier

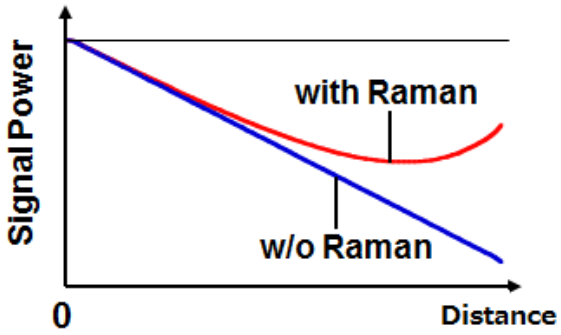

Figure 5.17: The gain profile with and without Raman amplification

performed homodyne detection of a a polarization multiplexed 160 Gbaud, 64 QAM signal. The detailed experimental setup is shown in Fig. 5.13.

Initially, we used an EDFA-only gain system for a 150 km dispersion managed fiber link composed of two spans of SLA (50 km)-IDF (25 km) link, whose average loss per span was approximately 18 dB. Then a Raman gain amplification system was used, where it was connected in tandem with EDFA and made to compensate for 10 dB, while EDFA compensated for the remaining 8 dB of the 18 dB loss. The CW laser at the receiver was phase-locked to the data signal via an OPLL circuit. Thereafter, similar process as that at the transmitter was employed in generating a Nyquist pulse train at the receiver, in which a polarization diversity homodyne receiver described in subsection 2.2.8 was employed. This was used for OTDM demultiplexing of the polarization multiplexed data signal using the orthogonality of Nyquist pulses, with homodyne detection also taking place simultaneously.

Digital back propagation involved loading the homodyne detected base-band signal back to the Nyquist pulse train and carrying out the above process. The values of the parameters we used are shown in table 5.1. After

Table 5.1: DBP parameters

	SLA	IDF
Group velocity dispersion β_2	-12 ps^2/km	24 ps^2/km
Nonlinear coefficient γ	0.89 W^{-1}km^{-1}	1.6 W^{-1}km^{-1}

DBP, waveform distortion compensation using frequency domain equalization (FDE) was performed.

5.4.4 Experimental results

Figure 5.18(a) shows the waveform of the baseband signal obtained after homodyne detection. In order to perform DBP, the received data signal was first numerically loaded on to a 10 GHz Nyquist pulse train, with one of the polarizations resulting in the waveform shown in Fig. 5.18(b). The signal shown in Fig. 5.18(b) was then taken through a digital back propagation as explained in the previous section.

I optimized the launch power by comparing the BER performance of the demultiplexed and demodulated 10 Gsymbol/s-64 QAM data signal at various launch powers. The figure showing that optimization result is depicted in Fig.5.19. By adopting DBP, we were able to increase the transmission power from 4 dBm to 6 dBm. Any further increase in the launch power beyond 6 dBm resulted in a sharp decline in the BER performance.

Figs. 5.20(a) and (b) show constellation maps with and without the application of DBP. With the use of DBP, the error vector maginitude (EVM) improved from 4.8% to 4.2%. As it can be seen, the distortion on the constellation maps was reduced, with the application of DBP. The BER performance of the demodulated 10 Gsymbol/s 64 QAM signal is shown in Fig. 5.21. The power penalty at a BER of 2.0×10^{-3} was improved by 1.5 dB to 4.0 dB. In order to further improve this performance, it is important to carry out DBP by considering the interaction between all tributaries.

When I adopted a Raman gain amplification system for loss compensation in the fiber link, there was an OSNR improvement of 7 dB after 150 km, compared to when we used an EDFA-only gain system as shown in Fig.

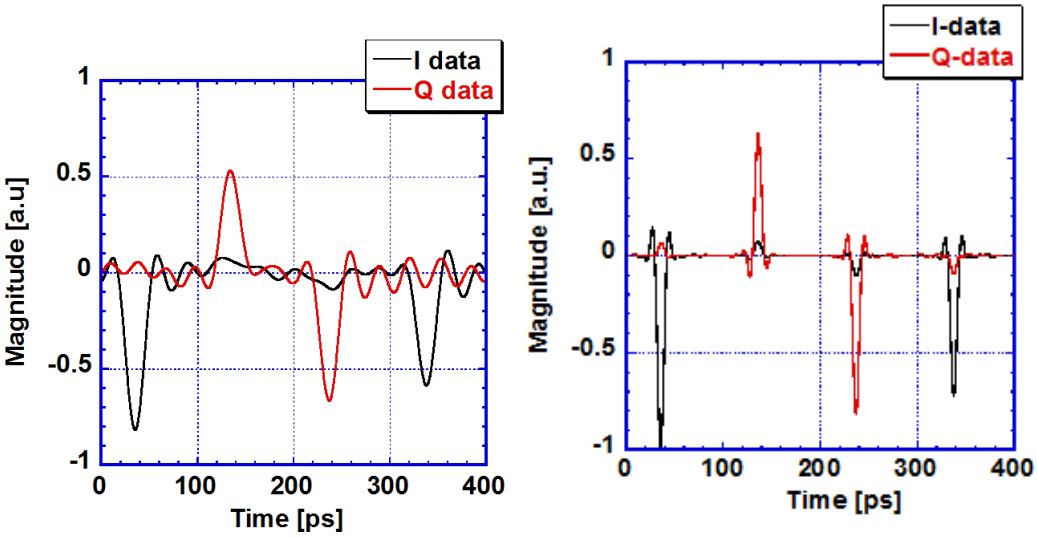

(a) Waveform after homodyne detection

(b) waveform after loading the signal to Nyquist pulse

Figure 5.18: Time waveform of the 10 Gsymbol/s 64 QAM signal at the receiver

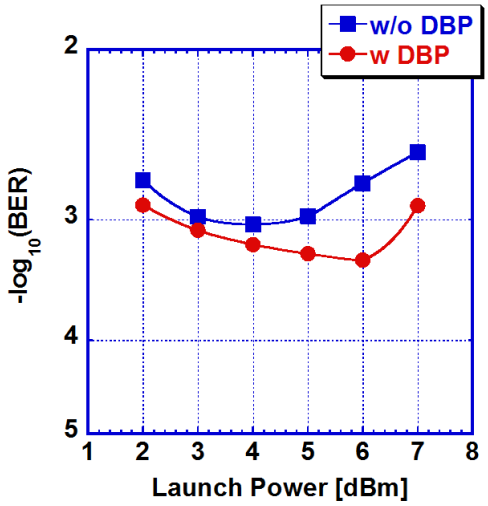

Figure 5.19: BER as a function of launch power

5.22(a) and 5.11(b). As shown in Fig. 5.22(b), with the adoption of Raman gain amplification system, the power penalty at a BER of 2.0×10^{-3} improved further by 1.2 dB to 2.8 dB for the 150 km transmission.

With this improvement in BER performances brought about the adoption of DBP and Raman gain amplification, we extended the transmission

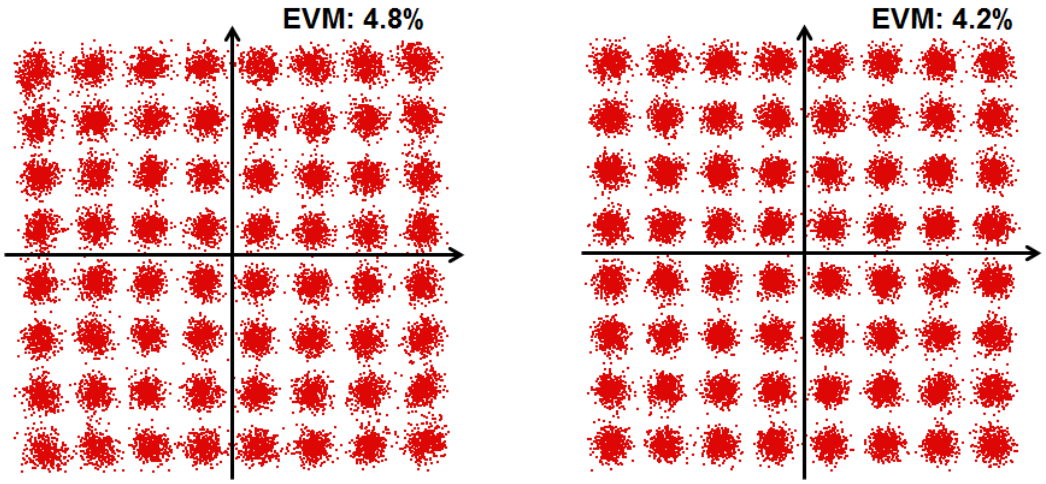

(a) Without DBP (b) With DBP

Figure 5.20: Constellation maps (a) without DBP and (b) after DBP

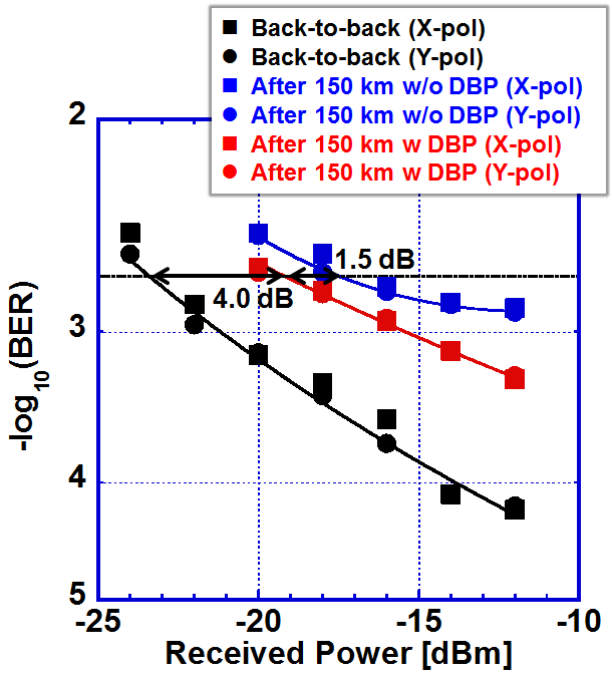

Figure 5.21: BER as a function of launch power after 150 km

distance from 150 km to 225 km. The BER performance is shown by the green plot on Fig. 5.22(b). The power penalty at a BER of 2.0×10^{-3} was 5.6 dB.

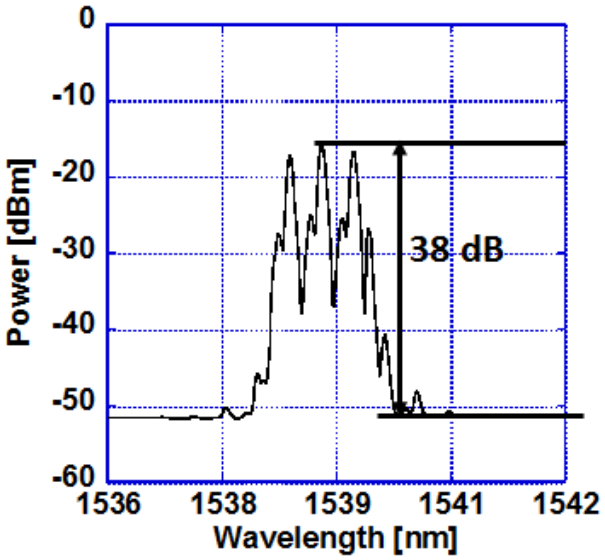

(a) Spetrum after 150 km, with Raman gain

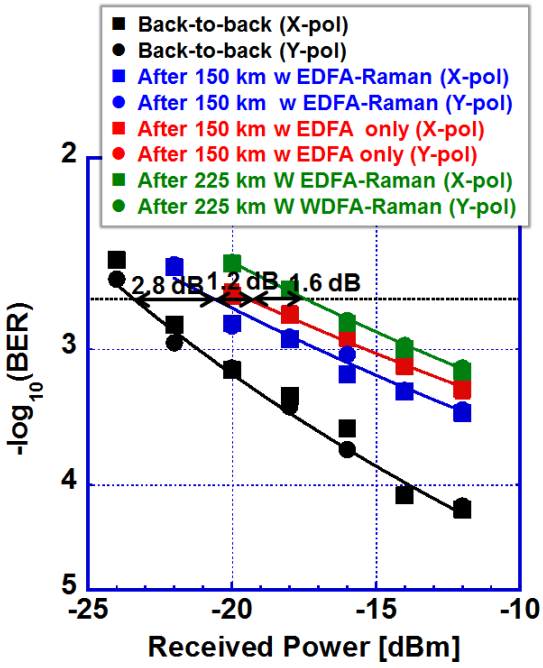

(b) BER after 150 km, and after 225 km

Figure 5.22: OSNR and BER performance with dual Raman gain amplifier

5.5 3.84 Tbit/s, 64 QAM Nyquist pulse transmission using frquency-stabilized mode-locked laser

By newly introducing a high OSNR optical source at the transmitter, it was possible to expand the baud rate from 160 Gbaud to 320 Gbaud. The high OSNR optical source used in this case was a HCN frequency-stabilized mode locked fiber laser (MLFL).

5.5.1 HCN frequency-stabilized mode-locked fiber laser (MLFL)

The configuration of the laser used is shown in Fig. 5.23. The MLFL was a fiber ring laser that consisted of two LD pumps connected to the ring cavity by means of a WDM coupler. The ring cavity consited of an EDFA wound on a piezo-electric transducer (PZT), a dispersion compensating fiber (DCF), an output coupler, an etalon filter, an isolator and and a phase modulator. The total length of the cavity was 11 m, resulting in a free spectral range (FSR) of 18 MHz. Part of the laser output was tapped and one harmonic is filtered, where the frequency component filtered was passed through a phase modulator for phase sensitive detection. The frequency modulated signal was fed through an HCN gas cell. The P(10) absorption line of HCN was used to stabilize the optical frequency of the laser output. The error signal was fed back to the laser cavity PZT. Another part of the laser output was fed to a clock extraction circuit, where the extracted clock was passed through a phase shifter before being used to drive the phase modulator in the ring cavity. A feedback circuit is used to control the phase of the clock that is fed to the phase modulator stabilizing the repetition rate of the laser. The waveform and optical spectrum of the laser output is shown Fig. 5.24. A short pulse of width 0.95 ps was generated and a spectral bandwidth of 3.8 nm or 475 GHz. The time bandwidth product was 0.45, close to the 0.44 transform limit condition of the Gaussian pulse. The output power was 17 dBm. The OSNR of the laser output was 48 dB, 10 dB greater than that OSNR of the comb used for the experiments in chapter 3 and 4. Based on this improvement in performance, I attempted to increase the symbol rate from 160 Gbaud to 320 Gbaud.

5.5.2 Experimental setup for the 3.84 Tbit/s, 64 QAM coherent Nyquist pulse transmission

The experimental setup used for the 3.84 Tbit/s, 64 QAM coherent Nyquist pulse is shown in Fig. 5.26. The optical output from the MLFL was fed into

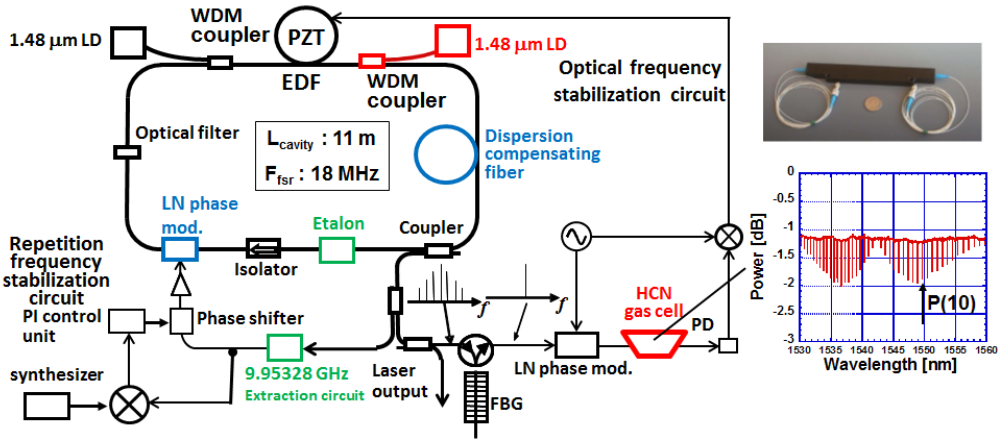

Figure 5.23: The configuration of the HCN frequency-stabilized mode-locked fiber laser (MLFL)

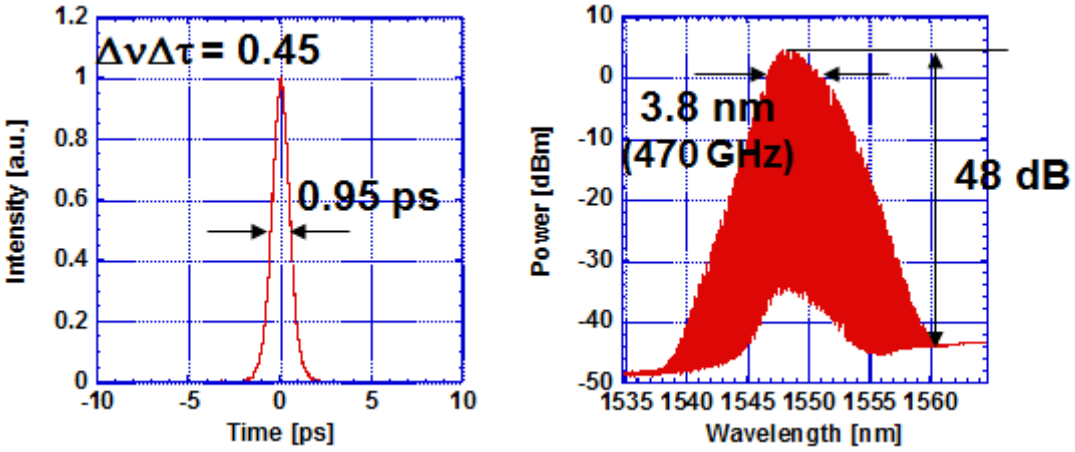

(a) Waveform (b) Spectrum

Figure 5.24: The MLFL output characteristics

a pulse shaper for Nyquist pulse shaping. The time waveform and optical spectrum of the Nyquist pulse generated of roll-off factor $\alpha = 0.5$ is shown in Fig. 5.25. The Nyquist pulse is modulated using an IQ modulator driven by an AWG with a 10 Gbaud, 64 QAM signal. The 10 Gbaud, 64 QAM signal was then multiplexed in the time domain first to 40 Gbaud, after which the 40 Gbaud signal was multiplexed to 320 Gbaud, 64 QAM data signal. A pilot tone signal was generated by extracting the 25th harmonic from the center frequency using a narrow filter, the tone was amplified and combined with the 3.84 Tbit/s, 64 QAM data signal.

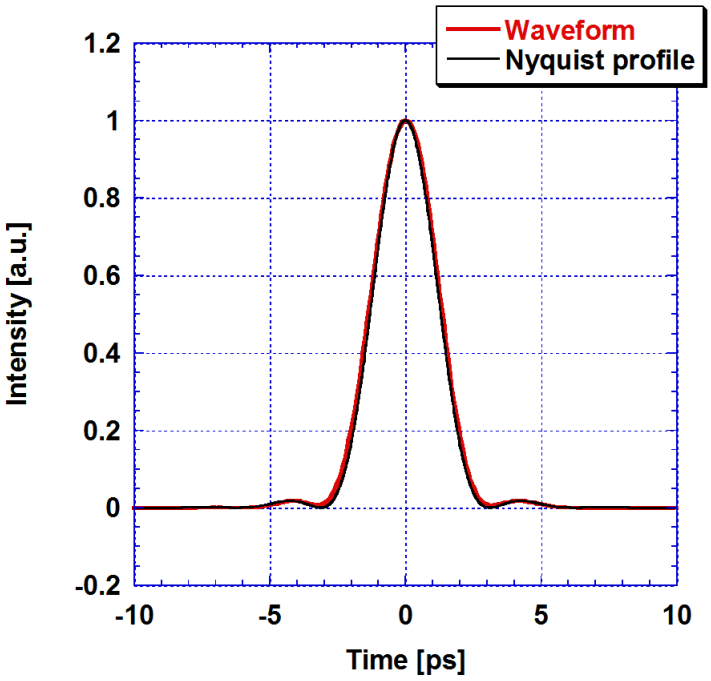

(a) Waveform

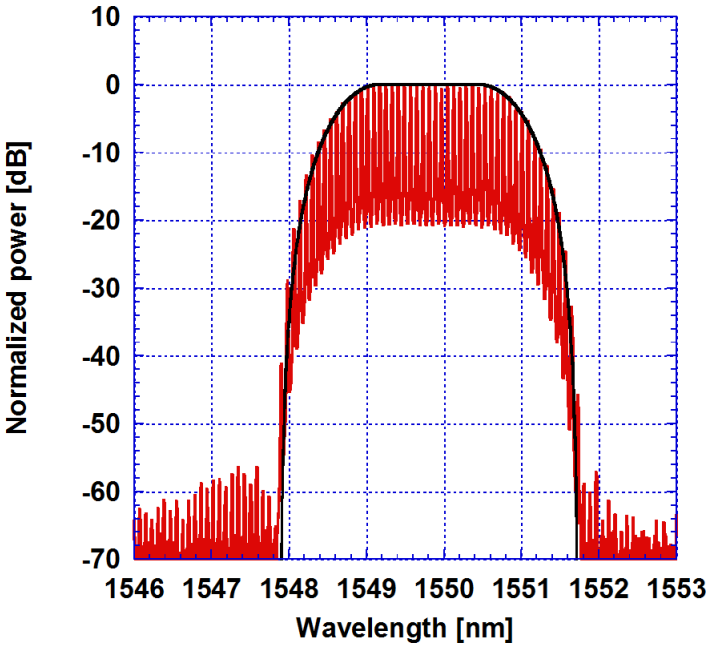

(b) Spectrum

Figure 5.25: Nyquist pulse generated ($\alpha = 0.5$)

At the receiver, part of the data signal was divided, and the pilot tone was filtered off and used for the OPLL process. In order to generate a local Nyquist pulse train, a CW fiber laser in combination with a comb generator was were used. The process of pulse generation was similar to that described in chapters 3 and 4. The 24th harmonic of the comb generated at the receiver is also filtered and used for the OPLL process. The local tone and the the extracted pilot tone signal are fed into a photodetector and their beat frequency of 10 GHz, kept constant by a feedback of the error voltage back to the CW laser at the receiver. In order to keep the OPLL loop length shorter, I fabricated EDFAs used in the OPLL circuit with EDFAs of high concentration making it possible to decrease the loop length to about 6 m from several tens of meters. This leads to phase noise reduction of the IF signal. The phase noise of the OPLL was reduced from 1.8 to 1.1 deg, which was much less than the phase allowance of a 64 QAM constellation map of 4.7 deg.

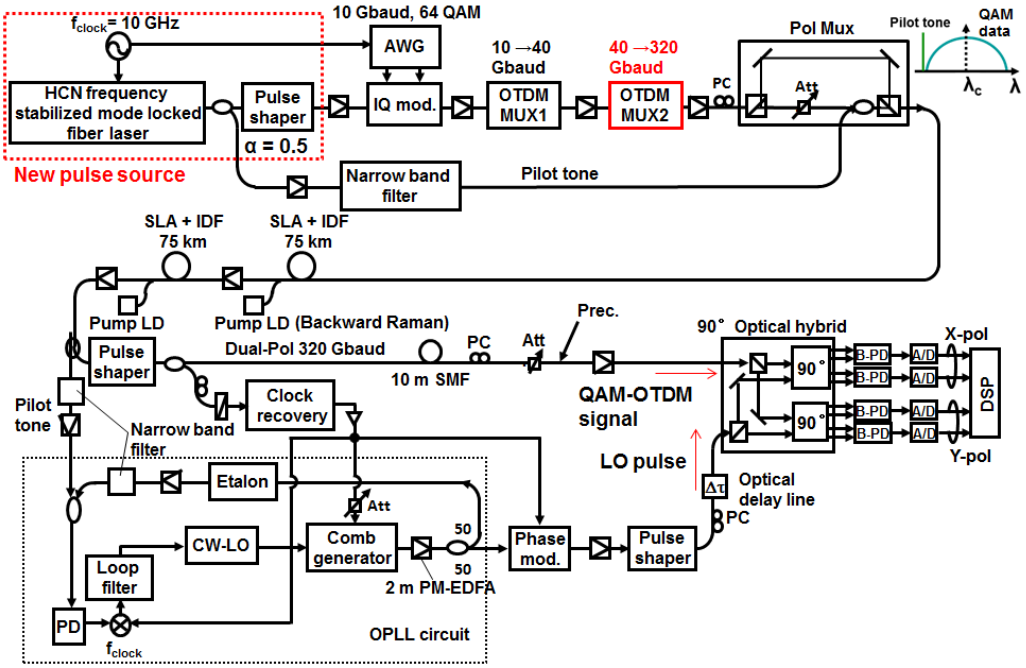

Figure 5.26: The experimental setup for the 3.84 Tbit/s, 64 QAM Nyquist TDM transmission using a MLFL

5.5.3 Experimental results

With the expansion of the spectral bandwidth from 160 GHz to 480 GHz, with Nyquist pulses of roll-off factor α of 0.5, the pulse signal begins to more more sensitive to polarization mode dispersion (PMD) effect. From 3 sets of 75 km spans of fiber labelled as #1, #2 and #3, a combination of two spans with lower PMD was selected. As shown in Fig. 5.27, within the 1549.8 nm region of the fiber which correspond to the signal bandwidth as shown in the region indicated by blue, the combination #1 and #2 had the best PMD performance compared to the other combinations. The other effect that I

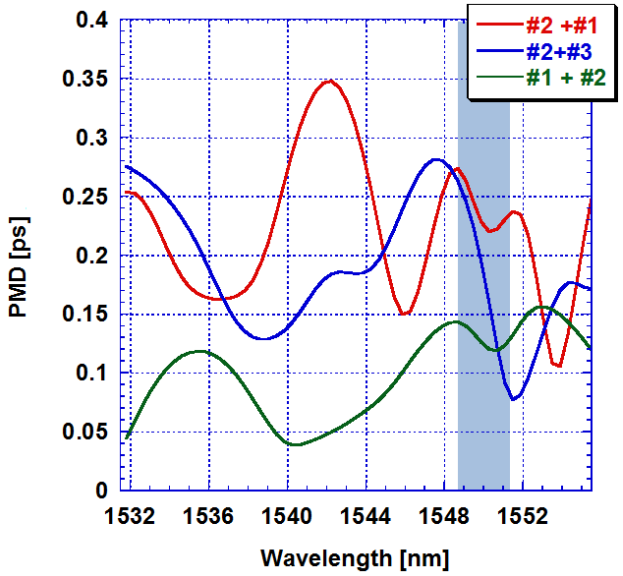

Figure 5.27: Polarization mode dispersion (PMD) of the three combinations of the 150 km dispersion-managed fiber (DMF)

examined was the signal sensitivity to spectral distortions arising from mainly EDFA gain frequency dependence. Flatness of EDFA gain affects the quality of the signal after it has been transmitted. First, I transmitted a single pulse without modulation and multiplexing through the fiber and observed the change in the spectrum, before and after 150 km of transmission. Figure 5.28 shows a set of two spectra, before and after 150 km of transmission. As it can be seen with the two set of spectra, by giving the spectrum before transmission some distortion, the spectrum after 150 km of transmission assumes the ideal Nyquist profile. It is also evident with the waveform, that the waveform before transmission is distorted, however the spectrum after 150 km of transmission assumed a close to ideal Nyquist profile. I undertook a spectral domain compensation such that the final spectrum at

the receiver took an ideal Nyquist profile by a process called predistortion, where components that get enhanced, are given more attenuation before transmission.

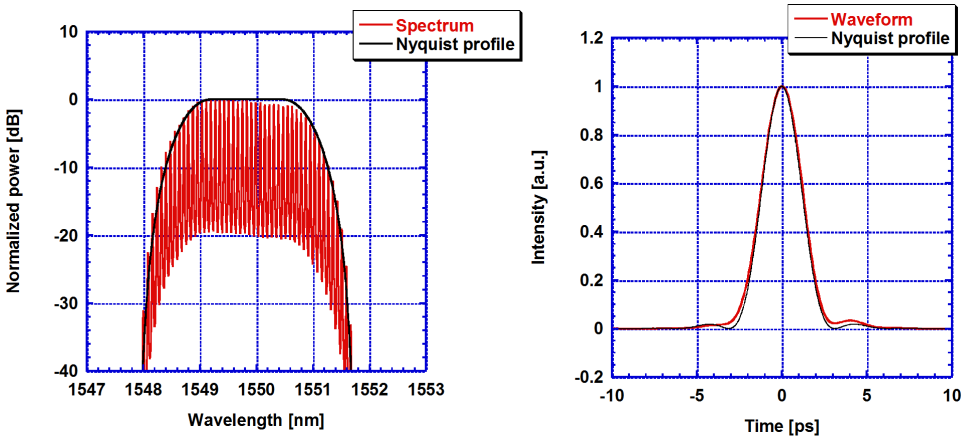

(a) Spectrum at the transmitter

(b) Waveform at the transmitter

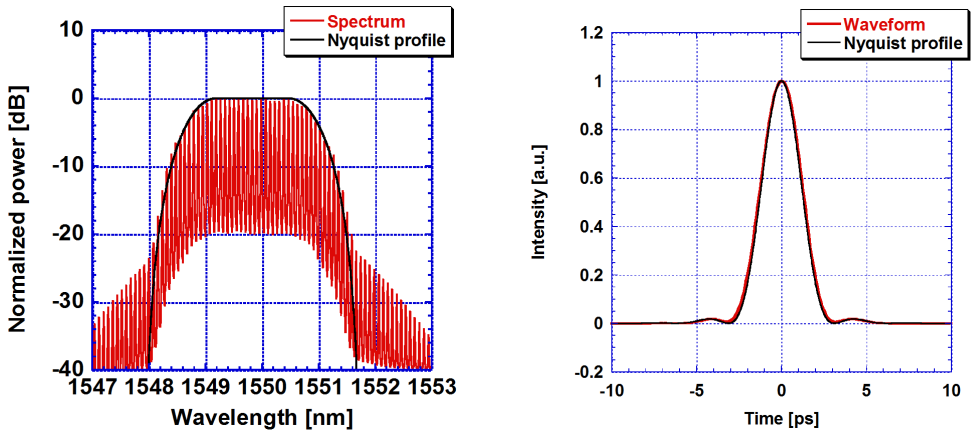

(c) Spectrum after 150 km

(d) Waveform after 150 km

Figure 5.28: Nyquist pulse spectra and waveform before and after 150 km

I also carried out pre-compensation of the dispersion such that the waveform after 150 km was close to the ideal Nyquist pulse. Figure 5.29 shows the effect of pre-distortion on the pulse waveform after 150 km of transmission. The 2nd order chirp was compensated for at the pulse shaper at the transmitter. The optimum second order chirp given to the waveform was equivalent to 0.2 ps^2. The third order chirp was varied from -0.1 to -0.4 ps^3, with the optimum value found to be about -0.2 ps^3.

After optimization of the transmission link and the transmitter, an optimization of the launch power was carried out. The fiber link loss was

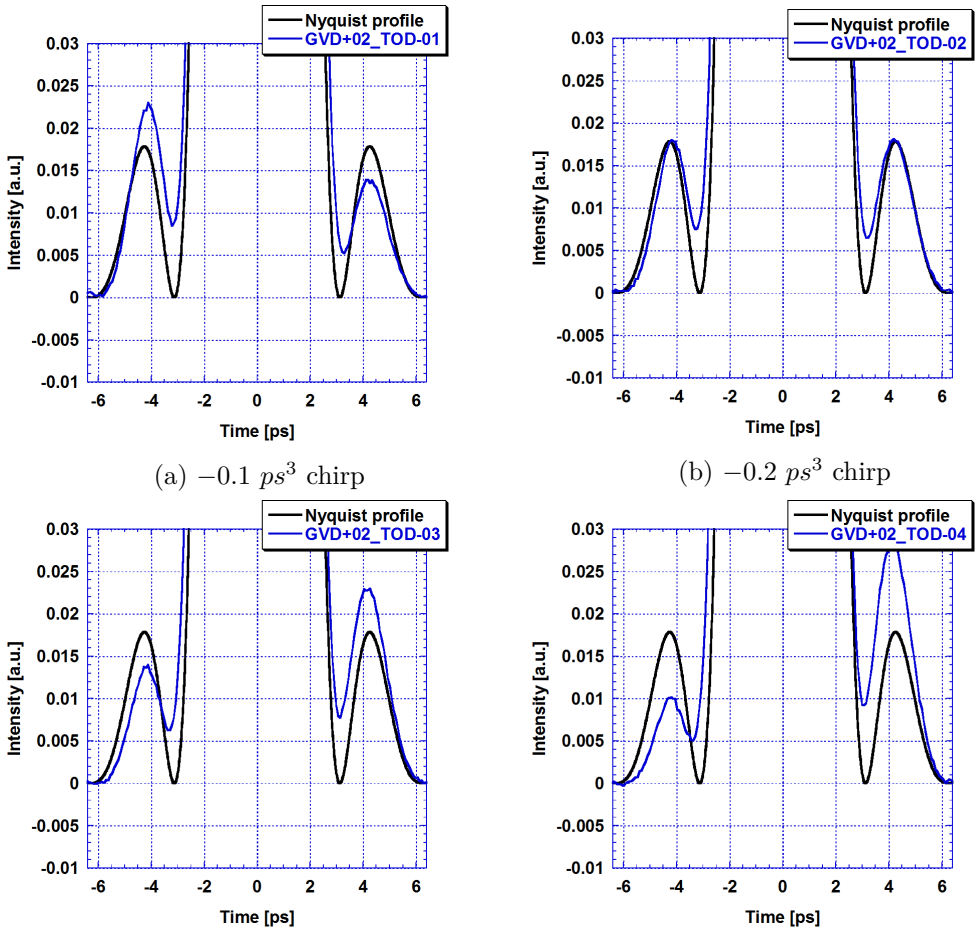

(a) $-0.1\ ps^3$ chirp

(b) $-0.2\ ps^3$ chirp

(c) $-0.3\ ps^3$ chirp

(d) $-0.4\ ps^3$ chirp

Figure 5.29: Third order chirp compensation

compensated for using a combination of both EDFA and Raman amplifiers. The fiber link had a total loss of about 17 dB/span, with the EDFA providing 7 dB gain while EDFA provided the remaining 10 dB.

The OPLL IF spectrum of the beat signal between the pilot tone signal and a harmonic generated at the receiver for OPLL operation was measured and the phase noise obtained. Figs. 5.30(a) and 5.30(b) show the IF spectrum of the beat signal and the corresponding single side spectrum. The phase noise after 150 km of transmission was 1.16 deg which is the approximately the same at the value under back to back condition. This is well below the 4.7 deg. phase allowance of the points on a 64 QAM constellation map, meaning that the OPLL circuit is sufficient for the homodyne detection of a 64 QAM signal. Figure 5.31 shows the BER of the polarization multiplexed 10 Gbaud,

64 QAM signal as a function of the launch power. At low values of the launch power, due to insufficient OSNR, there was decreased performance. At transmission power above 5 dBm, there was BER degradation due to increased nonlinearity in the fiber. The optimum value for the transmission power was then set at 5 dBm. Fig. 5.32 shows the optical spectra before and after 150 km. The spectra were obtained at a resolution of 0.1 nm. From the figure, the OSNR before transmission was 52.1 dB, which degraded by 13.5 dB to 38.6 dB. The constellation maps before and after 150 km is shown in Fig. 5.33. The EVM under back-to-back condition was 3.6%. After 150 km, the EVM was 5.4%. The increase in EVM was accompanied by an increase in size of the constellation points and phase rotation on the constellation points at the corner. The increase in size of the constellation map can be attributed to the decrease in OSNR of the signal after transmission. The rotation on the constellation map arises from the nonlinear phase rotation in the fiber during transmission.

I evaluated the bit error rate obtained from the experimental setup. The graph shown in Fig. 5.34 is a plot of the BER as a function of the received power. The BER obtained was less than 20% FEC threshold. This BER is expected to be improved by introducing a digital back propagation to this experiment.

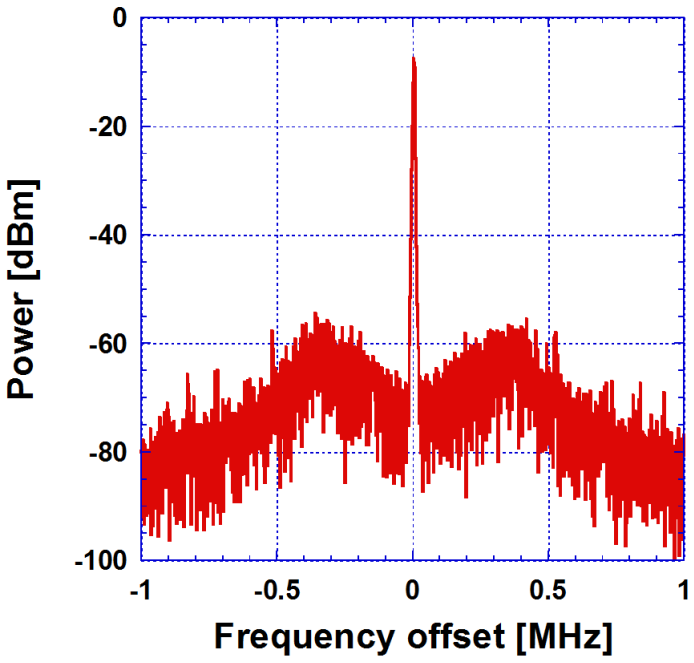

(a) IF spectrum

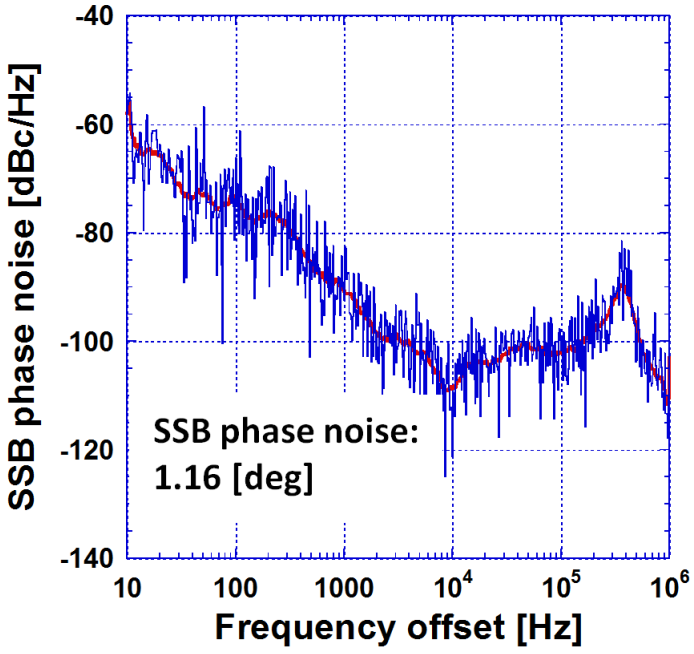

(b) Single side spectrum

Figure 5.30: IF spectrum of the beat signal between the pilot signal and a harmonic generated at the receiver for OPLL operation

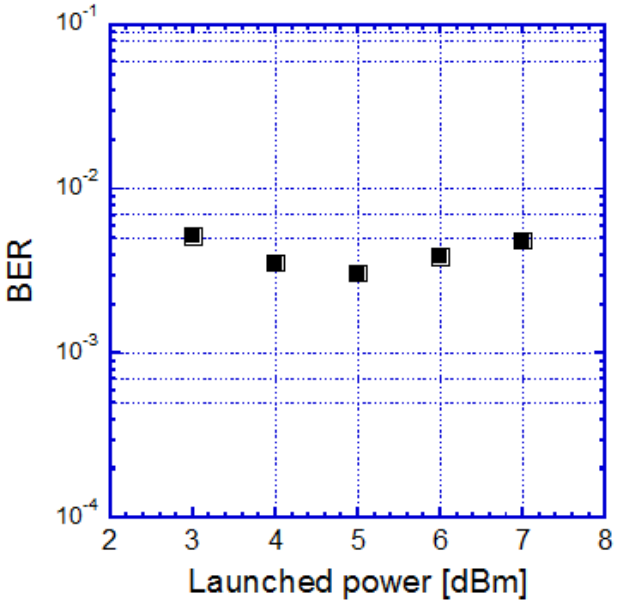

Figure 5.31: Optimization of launch power

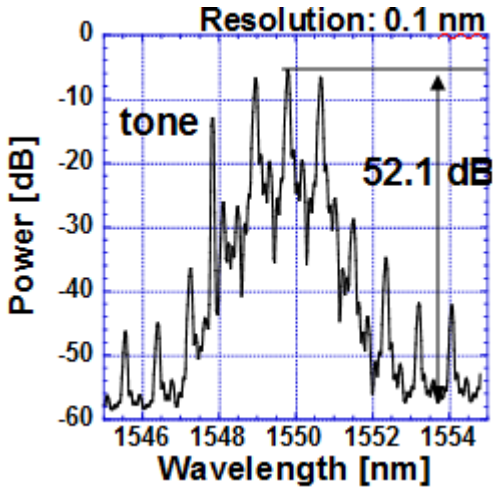

(a) Before 150 km

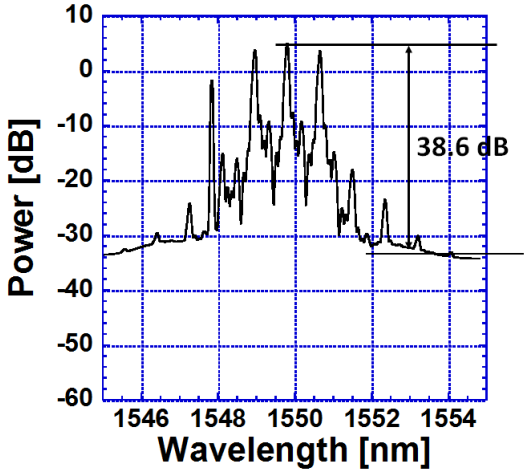

(b) After 150 km

Figure 5.32: The optical spectra before and after 150 km

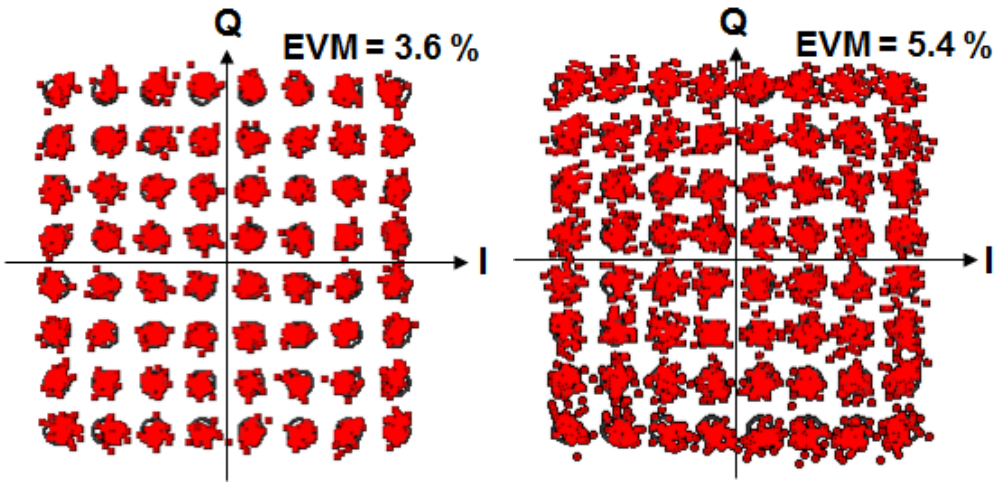

(a) Back-to-back (b) After 150 km

Figure 5.33: Constellation maps before and after 150 km

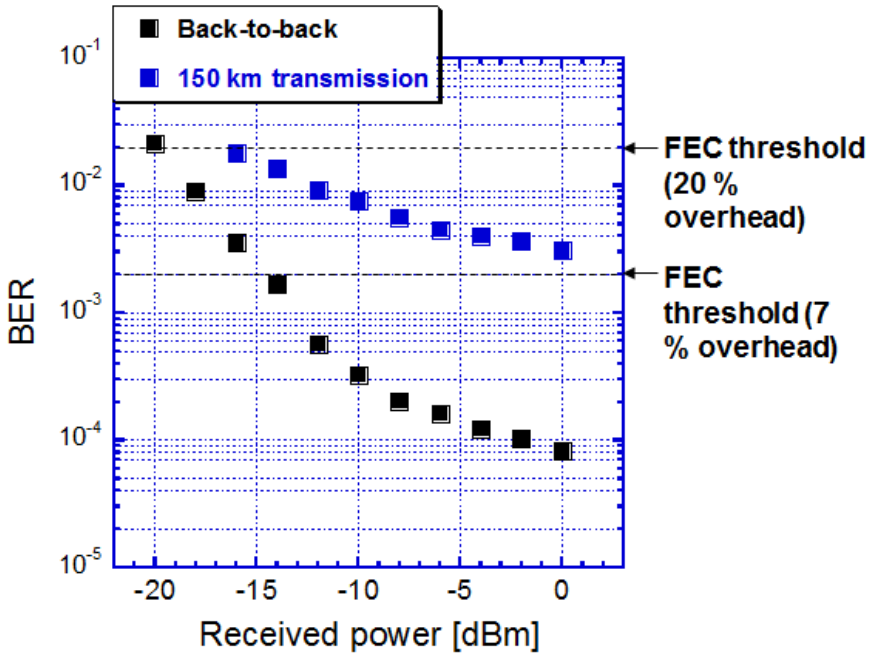

Figure 5.34: The BER for the 3.84 Tbit/s, 64 QAM Nyquist TDM transmission using MLFL

5.6 Discussion and conclusion

In this chapter, I demonstrated a coherent Nyquist pulse transmission at 1.92 Tbit/s and with an SE as high as 10.6 bit/s/Hz by taking advantage of the time-domain orthogonality of the Nyquist pulse. A key technology behind this significant SE increase is a novel demodulation and demultiplexing scheme in which the transmitted Nyquist pulse is homodyne detected with a phase-locked Nyquist LO pulse. This allowed the use of Nyquist pulse with a minimum spectral width, i.e., roll-off factor $\alpha = 0$. I verified that this scheme offers better performance than the optical sampling scheme described in chapter 4. Based on this scheme, I carried out a 1.92 Tbit/s, 64 QAM OTDM transmission in which the signal bandwidth was greatly required to 170 GHz. This leads to a spectral efficiency of:

$$SE = \frac{1.92\ Tbit/s}{170\ GHz \times 1.07} = 10.6\ bit/s/Hz$$

This is the highest SE value yet achieved in a Tbit/s/ch transmission. By further use of digital back propagation (DBP) for nonlinear phase rotation compensation and Raman amplification in the fiber link, I was able to increase the transmission distance to 225 km.

Furthermore, by use of a high OSNR HCN frequency-stabilized mode locked fiber laser (MLFL), I was able to increase the symbol rate from 160 Gbaud to 320 Gbaud, enabling the bit rate of 3.84 Tbit/s. The 3.84 Tbit/s, 64 QAM coherent pulse transmission experiment over 150 km was achieved with Nyquist pulses of roll-off factor $\alpha = 0.5$ where the spectral bandwidth was 490 GHZ. The spectral efficiency in this case was 6.5 bit/s/Hz.

Chapter 5 Reference

[1] K. Harako, D. O. Otuya, K. Kasai, T. Hirooka, N. Masataka, "High-performance TDM demultiplexing of coherent Nyquist pulses using time-domain orthogonalityy," *Opt. Exp.* 22(24), 29456-29464, (2014).

[2] K. Harako, D. O. Otuya, K. Kasai, T. Hirooka, N. Masataka, "Novel Ultrafast TDM Demultiplexing Scheme Using Orthogonality in Coherent Nyquist Pulses," *European Conference on Optical Communications* Tu.4.6.5, (2014).

[3] D. O. Otuya, K. Harako, K. Kasai, T. Hirooka, N. Masataka, "A Single-Channel 960 Gbit/s 64 QAM Orthogonal TDM Transmission with a Spectral Efficiency of 10.0 bit/s/Hz Using Coherent Nyquist Pulses," *European Conference on Optical Communications* We.2.3.4, (2014).

[4] D. O. Otuya, K. Harako, K. Kasai, T. Hirooka, N. Masataka, "Single-Channel 1.92 Tbit/s, 64 QAM Coherent Orthogonal TDM Transmission of 160 Gbaud Optical Nyquist Pulses with 10.6 bit/s/Hz Spectral Efficiency," *In proceedings of Optical Fiber Communications Conference (OFC)* M3G.2, (2015).

[5] H. Nyquist, "Certain topics in telegraph transmission theory," *Trans. Am. Inst. Electric. Eng.* 47, 617-644, (1928).

[6] H. Nyquist, "Novel Ultrafast TDM Demultiplexing Scheme Using Orthogonality in Coherent Nyquist Pulses," *European Conference on Optical Communications* Tu.4.6.5, (2014).

[7] M. Nakazawa, T. Hirooka, P. Ruan, and P. Guan, "Ultrahigh-speed "orthogonal" TDM transmission with an optical Nyquist pulse train," *Opt. Exp.* 20(2), pp. 1129-1140 (2012).

[8] C. Paré , A. Villeneuve, P. -A. Bé langer, and N. J. Doran, "Compensating for dispersion and the nonlinear Kerr effect without phase conjugation," *Opt. Lett.*, 21(7), pp.459-461 (1996).

[9] R. H. Stolen, *Proc. IEEE*, 68, 1232, (1980).

[10] T. Emori, and S. Namiki, "100 nm bandwidth flat gain Raman amplifiers pumped and gain-equalized by 12-wavelength-channel WDM high power laser diodes," *OFC*, PD19, 1999.

Chapter 6

Conclusion

This thesis has demonstrated ultrahigh-speed and highly spectral-efficient digital coherent transmission using coherent optical pulses.

In chapter 1, I described the motivation of this work by highlighting the current state of internet traffic in Japan, which is continuously increasing by 40% annually. Considering the finite bandwidth resource available in optical fibers, which is approximately 10 THz, it was clarified that the increase in a single-channel bit rate and SE simultaneously is one of the critical issues in order to meet the increasing capacity demand in the next-generation optical communication. By pointing out the difficulties in increasing the single-channel bit rate in the current digital coherent transmission, the motivation of developing a digital coherent pulse transmission was provided.

In Chapter 2, I newly established key components required for digital coherent pulse transmission, including a coherent short pulse source for high-speed QAM transmission, OPLL for highly precise phase synchronization between transmitted pulse and LO, RZ-CW conversion for increasing SNR of the demultiplexed high-speed signal in spite of limited receiver bandwidth, and FDE for accurate compensation of waveform distortion associated with optical pulse transmission. It was experimentally demonstrated that all these components play a crucial role in increasing the QAM multiplicity such as 64 levels while retaining a bit rate as fast as 1 Tbit/s/ch.

In Chapter 3, based on these components, I first demonstrated a coherent pulse transmission using a Gaussian pulse, which is a typical waveform used for high-speed pulse transmission. By using RZ-CW conversion and FDE, a SNR degradation and phase noise associated with the pulse transmission was successfully reduced. As a result, 1.92 Tbit/s, 64 QAM transmission was achieved with an SE of 3.8 bit/s/Hz. This is the first demonstration of digital coherent pulse transmission at 64 QAM.

In Chapter 4, in order to explorer much higher SE, I further proposed a

coherent Nyquist pulse that enables an ultrahigh-speed transmission within a narrow bandwidth. The important feature of this pulse is that it has an oscillating tail with periodic zero-crossing points that allow OTDM with a significant overlap between adjacent pulses while maintaining intersymbol interference (ISI)-free condition at each symbol location. To realize this, novel schemes of Nyquist pulse shaping and ultrafast optical sampling were developed. I constructed a coherent Nyquist pulse transmission with a roll-off factor $\alpha = 0.5$. As a result, 1.92 Tbit/s/ch, 64 QAM transmission was successfully achieved within a bandwidth of 240 GHz, resulting in the SE to be increased from 3.8 bit/s/Hz to 7.5 bit/s/Hz. However, this was not the ultimate spectral efficiency since Nyquist pulses of roll-off factor $\alpha = 0.0$ offers an even narrower signal bandwidth, whereas the increased ISI effect with roll-off factor of $\alpha = 0$ limited the use of Nyquist pulse.

In Chapter 5, for making the maximum use of the potential of coherent Nyquist pulse toward ultrahigh SE, I proposed the novel coherent Nyquist pulse transmission scheme that takes advantage of the orthogonal property of Nyquist pulses. The key technology is to use a Nyquist LO pulse for demodulation and demultipleixing at the receiver, whose phase and timing a synchronized with a transmitted Nyquist pulse. It was experimentally demonstrated that this scheme offers a high-SNR demultiplexing even for a Nyquist pulse with roll-off factor as low as $\alpha = 0$. Based on this scheme, a 1.92 Tbit/s, 64 QAM transmission was achieved within a bandwidth of 170 GHz, leading to a spectral efficiency of 10.6 bit/s/Hz, which is the highest SE yet achieved in a single-carrier Tbit/s transmission. This demultiplexing scheme also made it possible to use a polarization diversity coherent receiver configuration. Simultaneous reception of both polarizations allowed the use of digital back propagation (DBP) for compensating for distortions due to dispersion and nonlinear optical effects. The improvement in transmission performance with DBP was also demonstrated in the chapter. After combining these schemes with Raman amplification, a 1.92 Tbit/s, 64 QAM transmission distance was extended to 225 km.

In order to increase the bit rate of the digital coherent pulse transmission, I newly introduced a 10 GHz HCN frequency-stabilized mode-locked fiber laser at the transmitter, that can emit a coherent pulse directly with a high OSNR. The output pulse width as short as 950 fs enabled me to increase the symbol rate to 320 Gbaud, corresponding to the bit rate of 3.84 Tbit/s/ch. By using a Nyquist pulse with $\alpha = 0.5$, a 3.84 Tbit/s/ch transmission over 150 km was achieved within a signal bandwidth of 490 GHz, resulting in a spectral efficiency of 6.5 bit/s/Hz. A further improvement in the spectral efficiency would require the use of Nyquist pulse with a much lower roll-off factor and an improvement in BER performance to below the 7% FEC

overhead.

When the above values of the spectral efficiency are plotted as a function of the SNR, a graph shown in Fig. 6.1 is obtained. As it can be seen, with the utilization of Nyquist pulse of roll-off factor $\alpha = 0$, the spectral efficiency almost approaches the theoretical Shannon limit.

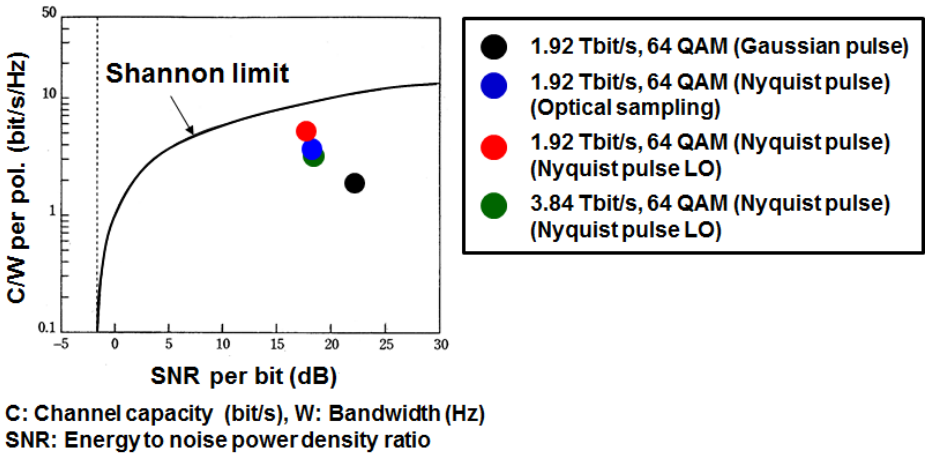

Figure 6.1: The shannon limit

List of Acronyms

ADC	Analog to digital converter
APDs	Avalance photodetectors
BER	Bit error rate
BPD	Balanced photodetector
BPSK	Binary phase shift keying
CW	Continuous wave
DAC	Digital to analog converter
DBM	Double balanced mixer
DBP	Digital back propagation
DCF	Dispersion compensating fiber
DPSK	Differential phase shift keying
DPSK	Differential quaternary phase shift keying
DSF	Dispersion shifted fiber
DSP	Digital signal processing
EAM	Electro-absorption modulator
EDFA	Erbium doped fiber amplifier
ETDM	Electrical time division multiplexing
EVM	Error vector magnitude
FBG	Fiber Bragg grating

FEC	Forward error correction
HNLF	Highly nonlinear fiber
IDF	Inverse dispersion fiber
IF	Intermediate frequency
IM/DD	Intensity-modulation/direct-detection
ISI	Intersymbol interference
LCoS	Liquid crystal on silicon
LD	Laser diode
LO	Local oscillator
MZM	Mach-Zehnder Modulator
NOLM	Nonlinear optical loop mirror
OOK	On-off keying
OPLL	Optical phase-locked loop
OTDM	Optical time division multiplexing
PBC	polarization beam combiner
PBS	Polarization beam splitter
PC	Polarization controller
PDM	Polarization division multiplexing
PZT	Piezo-electric transducer
QAM	Quadrature amplitude modulation
QPSK	Quaternary phase shift keying
RZ	Return to zero
SLA	Super large area fiber
SMF	Single mode fiber
SPM	Self phase modulation

TDM	Time division multiplexing
VCO	Voltage controlled oscillator
WDM	Wavelength division multiplexing
XPM	Cross phase modulation

Acknowledgements

First and foremost, I would like to express my appreciation to Professor Masataka Nakazawa of the Research Institute of Electrical Communication, at Tohoku University for accepting me to his group, the Ultrafast optical communication Lab, back in 2010. I am also grateful to the Honjo Foundation for funding my studies for the past 3 years.

My heartfelt thanks goes to Associate Professor Toshihiko Hirooka, Associate Professor Masato Yoshida, and Assistant Professor Keisuke Kasai. Spanning the period of my 3-year research, I have benefited immensely from very fruitful discussions with them, which made this a a very fruitful and enriching Ph.D study experience. I benefited greatly from their daily counsel and advice, given that the work spanned very broad aspects of high speed pulse transmission and coherent phase synchronization. I am especially grateful to Dr. Kasai for his always patient lectures and for tolerating my slow start in the field.

My utmost thanks goes to Mr. Satoshi Oikawa and Mr. Tokutaka Hara of Sumitomo Osaka Cement Co., Ltd., for providing a low V_π Mach-Zender (MZM) modulator that we used in our comb generator in our pulse generation system, without which most of the work here would not have been possible.

I would also like to acknowledge the input of my fellow Ph.D student Mr. Koudai Harako for the valuable help during the course of my study and experiments. His experimental input and advice was also very instrumental in getting a sizeable part of this work done. His help was very instrumental in making the novel demultiplexing scheme for Nyquist TDM signals a practical reality.

Most importantly, I am very grateful to Mr. Kazuki Yoshida, who is helping me in increasing the transmission capacity to 3.84 Tbit/s.

I would like to thank the Japan Society for the Promotion of Science (JSPS) for providing the Grant-in-Aid for specially Promoted Research (26000009) that funded a part of this research.

My special thanks to a very special friend Dr. Gerard Jimmy Paraison, who is more like brother to me, he provided me a lot of wise counsel and

emotional support during the course of my stay here in Sendai. His valuable friendly advice and moral support was instrumental in getting me through the tough times especially when I was ailing.

My thanks goes to my parents who sacrificed immensely to see me through school. Their invaluable support, both emotional and economic, has been always and highly appreciated.

My special gratitude to my fiancée Vashti T. Mensah, for moral support and company during the long working hours and busy days.

I am so much indebted to God whose grace, love and guidance protected me through the course of my studies in Sendai.

Presentations and Publications

Peer Reviewed Journal Papers

1. K. Kasai, **D. O. Otuya**, M. Yoshida, T. Hirooka, and M. Nakazawa, "Single-carrier 800-Gb/s 32 RZ/QAM coherent transmission over 225 km employing a novel RZ-CW conversion technique," *IEEE Photon. Technol. Lett.*, 24(5), 416-418, (2012).

2. **D. O. Otuya**, K. Kasai, M. Yoshida, T. Hirooka, and M. Nakazawa, "A single-channel 1.92 Tbit/s, 64 QAM coherent optical pulse transmission over 150 km using frequency-domain equalization," *Opt. Exp.*, 21(19), 2280-22816, (2013).

3. **D. O. Otuya**, K. Kasai, M. Yoshida, T. Hirooka, and M. Nakazawa, "Single-channel 1.92 Tbit/s, pol-mux-64 QAM coherent Nyquist pulse transmission over 150 km with a spectral efficiency of 7.5 bit/s/Hz," *Opt. Exp.*, 22(20), 23776-23785, (2014).

4. K. Harako, **D. O. Otuya**, K. Kasai, M. Yoshida, T. Hirooka, and M. Nakazawa, "High-performance TDM demultiplexing of coherent Nyquist pulses using time-domain orthogonality," *Opt. Exp.*, 22(24), 29456-29464, (2014).

5. K. Kasai, Y. Wang, **D. O. Otuya**, M. Yoshida, and M. Nakazawa, "448 Gbit/s, 32 Gbaud 128 QAM coherent transmission with a potential Spectral Efficiency of 10.7 bit/s/Hz," *Opt. Exp.*, 23(22), 28423-28429, (2015).

6. **D. O. Otuya**, K. Kasai, T. Hirooka, and M. Nakazawa, "Single-Channel 1.92 Tbit/s, 64 QAM coherent Nyquist pulse Orthogonal TDM transmission with a spectral efficiency of 10.6 bit/s/Hz," *Journal of Lightwave Techn.*, 43(2), 768-775, (2016).

International Conference Presentations

1. **D. O. Otuya**, K. Kasai, T. Hirooka, M. Yoshida, M. Nakazawa, T. Hara, and S. Oikawa, "A single-channel, 1.6 Tbit/s 32 QAM coherent transmission over 150 km with RZ-CW conversion and FDE techniques," *Optical Fiber Communication Conference (OFC)*, OTh4E.4, Anaheim, California, U.S., March 2013.

2. **D. O. Otuya**, K. Kasai, T. Hirooka, M. Yoshida, M. Nakazawa, T. Hara, and S. Oikawa, "A single-channel 1.92 Tbit/s, 64 QAM coherent pulse OTDM transmission over 150 km," *Opto-Electronics and Communications Conference (OECC)*, WR2-2, Kyoto, Japan, July 2013.

3. **D. O. Otuya**, K. Kasai, T. Hirooka, M. Yoshida, and M. Nakazawa, "1.92 Tbit/s, 64 QAM coherent Nyquist pulse transmission over 150 km with a spectral efficiency of 7.5 bit/s/Hz," *Optical Fiber Communication Conference (OFC)* 2014, W1A.4, , San Francisco, California, U.S., March 2014.

4. K. Harako, **D. O. Otuya**, K. Kasai, T. Hirooka, and N. Nakazawa, "Novel ultrafast TDM demultiplexing scheme using orthogonality in coherent Nyquist pulses," *European Conference on Optical Communication (ECOC)* 2014, Tu.4.6.5, Cannes, France, September 2014.

5. **D. O. Otuya**, K. Harako, K. Kasai, T. Hirooka, and M. Nakazawa, "A single-channel 960 Gbit/s, 64 QAM orthogonal TDM transmission with a spectral efficiency of 10.0 bit/s/Hz using coherent Nyquist pulses," *European Conference on Optical Communication (ECOC)* 2014, We.2.3.4, Cannes, France, September 2014.

6. **D. O. Otuya**, K. Harako, K. Kasai, T. Hirooka, and M. Nakazawa, "Single-channel 1.92 Tbit/s, 64 QAM coherent orthogonal TDM transmission of 160 Gbaud optical Nyquist pulses with 10.6 bit/s/Hz spectral efficiency," *Optical Fiber Communication Conference (OFC)* 2015, W1A.4, Los Angeles, California U.S., March 2015.

7. K. Kasai **D. O. Otuya**, K. Harako, T. Hirooka, and M. Nakazawa, "High-Speed, High Spectrally Efficient 64 QAM Orthogonal TDM Coherent Nyquist Pulse Transmission," *IEEE Summer Topicals Meeting Series* 2015, MF1.3, Nassau, Bahamas, July 2015.

Local National Conferences

1. 葛西恵介、**D. O. Otuya**、吉田真人、廣岡俊彦、中沢正隆、 “RZ-CW変換法を用いた単一チャネル800 Gbit/sコヒーレント32QAM伝送、” 電子情報通信学会総合大会、 B-10-55,(2012.3).

2. **D. O. Otuya**, K. Kasai, T. Hirooka, M. Yoshida, and M. Nakazawa, “1.6 Tbit/s, Single-carrier 32 RZ/QAM Coherent Transmission Over 150 km Utilizing an RZ-CW Conversion Scheme,” 電気関係学会東北支部大会、IEEE Student Session, 2A05, (2012.8)

3. **D. O. Otuya**、葛西恵介、廣岡俊彦、吉田真人、中沢正隆、 “単一チャネル1.92 Tbit/s, 64 QAM-150 kmコヒーレントパルス伝送、” 電子情報通信学会ソサイエティ大会 B-10-28, (2013.9).

4. **D. O. Otuya**、葛西恵介、廣岡俊彦、吉田真人、中沢正隆、 “周波数利用効率7.5 bit/s/Hzを有する1.92 Tbit/s, 64 QAMコヒーレントパルス伝送、” 電子情報通信学会総合大会、 B-10-47, (2014.3).

5. K. Harako, **D. O. Otuya**, Keisuke Kasai, T. Hirooka, M. Yoshida, and M. Nakazawa, “Novel TDM Demultiplexing of 80 Gbaud, 64 QAM Coherent Nyquist Pulses Using Time-domain Orthogonality,” 電気関係学会東北支部大会、IEEE Student Session, 1A12, (2014.8)

6. 葛西恵介、**D. O. Otuya**、原子広大、廣岡俊彦、吉田真人、中沢正隆、 “周波数利用効率10 bit/s/Hzを有する960 Gbit/s/ch, 64 QAM-150 kmコヒーレントナイキスとパルス伝送,” レーザー学会学術講演会第35回年次大会、 G11aVI-5, (2015.1).

7. **D. O. Otuya**、原子広大、葛西恵介、廣岡俊彦、吉田真人、中沢正隆、 “周波数利用効率10.6 bit/s/Hzを有する1.92 Tbit/s/ch, 64 QAMコヒーレントナイキスとパルス伝送,” 電子情報通信学会総合大会、 B-10-26, (2015.3).

8. 葛西恵介、王 怡昕、**D. O. Otuya**、吉田真人、中沢正隆、 “10.7 bit/s/Hzの周波数利用効率を有する448 Gbit/s/ch, 32 Gbaud 128 QAM-150 kmコヒーレント伝送,” 電子情報通信学会ソサイエティ大会 B-10-50, (2015.9).

Research Meeting Presentations

1. 葛西恵介、**D. O. Otuya**、吉田真人、廣岡俊彦、中沢正隆、 “RZ-CW変換法を用いた800 Gbit/sコヒーレント32 RZ/QAM-225 kmコヒーレントOTDM伝送、” 東北大学電気通信研究所共同プロジェクト研究会「超高速コヒーレント光制御による極限通信・計測に関する研究会」、(2011.11).

2. 葛西恵介、**David Odeke Otuya**、吉田真人、廣岡俊彦、中沢正隆、 “RZ-CW変換法を用いた32 RZ/QAM伝送、” 電子情報通信学会光通信システム研究会、OCS2012-23、(2012.7).

3. **D. O. Otuya**、葛西恵介、廣岡俊彦、吉田真人、中沢正隆、“単一チャネル1.92 Tbit/s, 64 QAM-150kmコヒーレントパルス伝送,” 東北大学電気通信研究所共同プロジェクト研究会「超高速コヒーレント光制御による極限通信・計測に関する研究会」、(2013.12).

4. 原子広大、**D. O. Otuya**、葛西恵介、廣岡俊彦、中沢正隆、“コヒーレント光ナイキストパルスを用いた直交時分割多重信号の超高速多重分離,” 電子情報通信学会光通信システム研究会、OCS2014-60、(2014.10).

5. **D. O. Otuya**、原子広大、葛西恵介、廣岡俊彦、中沢正隆、“周波数利用効率10.6 bit/s/Hzを有する1.92 Tbit/s/ch、64 QAMコヒーレントナイキストパルス伝送,” 東北大学電気通信研究所共同プロジェクト研究会「マルチキャリア光波による先進通信・計測に関する研究会」、(2014.12).

6. **D. O. Otuya**, K. Harako, K. Kasai, T. Hirooka, and M. Nakazawa, “1.92 Tbit/s 64 QAM coherent Nyquist orthogonal TDM transmission with a spectral efficiency of 10.6 bit/s/Hz,” 電子情報通信学会光通信システム研究会、OCS2015-26、(2015.7).

Awards and Recognitions

1. 2012, The best paper prize, IEEE Sendai Section
2. 2015, Honorable Mention Award, Institute of Electronics, Information and Communication Engineers (IEICE) of Japan
3. 2015, Finalist for the Corning Outstanding Student Paper Award at the Optical Fiber Communication Conference (OFC) 2015